Title

Water-evaporation reduction by duplex films: Application to the human tear film

Journal

Advances in Colloid and Interface Science, 197-198

ISSN

00018686

Authors

Cerretani, Colin F
Ho, Nghia H
Radke, C.J.

Publication Date

2013-09-01

DOI

10.1016/j.cis.2013.03.007

Water-Evaporation Reduction by Duplex Films: Application to the Human Tear Film

Colin F. Cerretani[a], Nghia H. Ho[a], C. J. Radke[a,b]*

[a] Department of Chemical and Biomolecular Engineering, University of California, Berkeley,
CA 94720-1462

[b] Vision Science Group, University of California, Berkeley, CA 94720-1462

submitted to and accepted by
Advances in Colloid and Interface Science
DOI: http://dx.doi.org/10.1016/j.cis.2013.03.007
published by Elsevier

*Correspondence: Professor Clayton J. Radke, Ph.D., Department of Chemical and Biomolecular Engineering, University of California, Berkeley, 101C Gilman Hall, Berkeley CA, 94720-1462, United States.

Tel: +1 510 642 5204; fax: +1 510 642 4778.

E-mail address: radke@berkeley.edu

Water-Evaporation Reduction by Duplex Films: Application to the Human Tear Film

Colin Cerretani[a], Nghia H. Ho[a], and C. J. Radke[a,b]

[a]Department of Chemical and Biomolecular Engineering, University of California, Berkeley, CA 94720-1462, United States

[b]Vision Science Group, University of California, Berkeley, CA 94720, United States

Abstract

Water-evaporation reduction by duplex-oil films is especially important to understand the physiology of the human tear film. Secreted lipids, called meibum, form a duplex film that coats the aqueous tear film and purportedly reduces tear evaporation. Lipid-layer deficiency is correlated with the occurrence of dry-eye disease; however, *in-vitro* experiments fail to show water-evaporation reduction by tear-lipid duplex films. We review the available literature on water-evaporation reduction by duplex-oil films and outline the theoretical underpinnings of spreading and evaporation kinetics that govern behavior of these systems. A dissolution-diffusion model unifies the data reported in the literature and identifies dewetting of duplex films into lenses as a key challenge to obtaining significant evaporation reduction.

We develop an improved apparatus for measuring evaporation reduction by duplex-oil films including simultaneous assessment of film coverage, stability, and temperature, all under controlled external mass transfer. New data reported in this study fit into the larger body of work conducted on water-evaporation reduction by duplex-oil films. Duplex-oil films of oxidized mineral oil/mucin (MOx/BSM), human meibum (HM), and bovine meibum (BM) reduce water evaporation by a dissolution-diffusion mechanism, as confirmed by agreement between measurement and theory. The water permeability of oxidized-mineral-oil duplex films agrees with those reported in the literature, after correction for the presence of mucin.

We find that duplex-oil films of bovine and human meibum at physiologic temperature reduce water evaporation only 6-8 % for a 100-nm film thickness pertinent to the human tear film. Comparison to *in-vivo* human tear-evaporation measurements is inconclusive because evaporation from a clean-water surface is not measured and because the mass-transfer resistance is not characterized.

Keywords:

Evaporation reduction; dissolution-diffusion theory; duplex film; tear evaporation; tear-film lipid layer

Contents

1. Introduction

Water evaporation is relevant to countless chemical and biochemical processes. It is a non-equilibrium process whose driving force is the chemical-potential difference between liquid water and water in a sub-saturated vapor environment. Evaporation rate depends on the magnitudes of both the chemical-potential (i.e., concentration) driving force and the transport resistances between the water surface and the surrounding gas. Resistances arise from various mechanisms including: kinetic escape of water molecules to and from the interface, transport through possible layers of immiscible molecules covering the water surface, and convective-diffusion of water vapor through the surrounding gas. There is a rich history on evaporative mass-transfer resistance afforded by insoluble monolayers spread at the air/water surface [1-3]. A lesser studied, but equally important, resistance is the that of liquid duplex-oil films (~100 nm to 100 μm in thickness) spread over a water surface. Duplex films are defined as thick enough to display bulk properties with two separate interfaces, but thin enough that the effects of gravity are negligible [4-6].

There are two major applications of evaporation reduction by immiscible-liquid duplex films and, correspondingly, two schools of research. Initial work explored alternatives for surfactant monolayers in slowing evaporation from water reservoirs [5, 7, 8]. The goal was to reduce water loss over that achieved with surfactant monolayers. Thicker oil films were hypothesized to provide more resistance against evaporation and better structural integrity than those of monolayers [5, 9]. Indeed, duplex-oil films with thicknesses on the order of tens of microns reduced water evaporation more effectively than insoluble monolayers, but, in practice, the effectiveness of the films was questionable. Heymann and Yoffe [5] successfully established oil films that remained stable for months under laboratory conditions. With environmental conditions, however, evaporation reduction was compromised by film breakup (into lenses), fracture by wind and dust, and increased water temperature under a film-blanketed surface [10, 11].

More recently, the increasing prevalence of human dry-eye disease [12] spurred study of duplex-oil films in controlling the evaporation rate of water from the lipid-covered human tear film [13, 14]. Water evaporation from the tear film plays a central role in dry eye, which affects up to 30 % of the global population [15]. The human tear film is approximately 5 µm thick [16]. Upon each blink, it coats the surface of the eye and, among other things, helps maintain proper hydration of the ocular epithelial surface, presents a smooth refractive surface for vision, and provides nutrients and cleansing [17]. The majority of the tear film is an aqueous solution containing salts, proteins, and soluble mucins. At the outermost layer of the tear film resides a lipid layer about 100-nm thick, composed of a complex mixture of lipids produced by the meibomian glands embedded in the eyelids. In healthy individuals, blink-secreted lipid, i.e., meibum, spreads upward as a thin-film curtain over the aqueous layer [18, 19]. The lipid layer is thought to function as a barrier against water evaporation from the underlying aqueous portion of the tear film [20-22].

The current paradigm for dry eye holds that increased water evaporation from the tear film through a defective lipid layer increases salinity of the remaining tear film [23-25]. Chronic salty tear triggers an immune response that initiates a vicious cycle of ocular discomfort, inflammation, and damage [12, 25-27]. Clinical observations indicate that dry-eye patients exhibit less uniform tear-film lipid layers (TFLL), lower tear production, increased tear-evaporation rates, and increased tear salinity compared to healthy individuals [12, 23, 24, 28-31]. Although clinical data suggest that the meibum film reduces tear evaporation considerably [20, 21, 32], *in-vitro* experiments with duplex films of tear lipid or similar lipids have so far failed to confirm significant evaporation reduction [13, 14, 33]. Thus, elucidation of the role of the tear-film duplex-lipid layer in water-evaporation reduction can both provide better understanding of dry eye and aid development of care solutions for individuals with compromised lipid layers [34-36].

We first provide a detailed summary of the previous literature on water-evaporation reduction by duplex-oil films. Next, background theory underlying duplex-film spreading and stability is presented. A physically based theoretical model is then outlined to describe water evaporation both from clean surfaces and through duplex-oil films. Importantly, the model addresses the roles of the vapor-phase composition, mass transfer, heat transfer, and film thickness and composition on evaporation rate. Following the theoretical section, an improved method for measuring evaporation reduction is presented that enables assessment of water-surface temperature, continuous visualization of film coverage, and controlled vapor-phase mass-transfer resistance. New *in-vitro* evaporation results with model films of oxidized mineral oil and of bovine-meibomian lipid demonstrate significant reduction in evaporation by a dissolution-diffusion mechanism for thicknesses ranging between 100 nm and 100 µm. Finally, the significance of these new results to human-tear evaporation and to dry eye is discussed.

2. Background

Research in water-evaporation reduction by duplex-oil films arises primarily in two different disciplines: physical chemists seeking mechanistic understanding for application to water conservation and vision scientists researching the tear-film lipid layer (TFLL). Motivation, methodology, and analyses are significantly different between the two approaches. Our review is divided into these two categories.

2.1 Oil duplex films

In their study of water evaporation through surfactant monolayers, Sebba and Briscoe [7] mention briefly evaporation reduction by duplex films of indicator oil. Indicator oil, first described by Blodgett [37] and later used extensively [7, 8, 38-40], is a mineral oil heated to its smoke point in the presence of oxygen. Oxidation products [41-43], such as fatty acids, alcohols, ketones, and others, render the mineral oil spreadable on water [37]. Without oxidation, mineral-oil films immediately form lenses at the air/water interface. Sebba and Briscoe [7] found that although tightly packed monolayers of long-chain alcohols, such as docosanol (C_{22}), reduce water evaporation by up to 99 %, duplex films of indicator oil evidence a noticeably smaller effect. For duplex-oil films that exhibit colored interference patterns, likely 100 to 200-nm thick, evaporation was reduced by only 3 %. Even films thick enough to be devoid of interference patterns, presumably on the order of microns, showed only a modest reduction of 73 % despite being over 100 molecules thick. These early results, however, are far from conclusive. Film thickness and surface temperature are unknown, spread-film areal coverage and stability are not examined, and measurements report only evaporation reduction. As described in §4.2.1, evaporation reduction depends on the experimental apparatus and on environmental conditions, so quantitative comparison among experimenters is not possible. Nevertheless, it is clear that the resistance to water evaporation mustered by a duplex-oil film is not as significant as that expected based on the results of monomolecular films. Still, the experiments of Sebba and Briscoe [7] marked the beginning of a decade of physical-chemistry research into water-evaporation reduction by duplex films.

Also in 1940, Docking *et al.* [9] suggested that duplex-oil films can indeed reduce evaporation by as much as compressed monolayers when they are carefully engineered to spread and remain stable against lens formation. Films consisting of high-molecular-weight polymerized oils dissolved in mineral oil and 1-2 µm in thickness reduced water evaporation by 50-60 % [9]. Additionally, 0.5-1 µm films composed of oil originating from fractions of vertical-retort tar reduced evaporation by 99 %. Although few experimental details are given, Docking *et al.* [9] noted the importance and difficulty of obtaining uniform, stable films to avoid rupture holes that compromise water-evaporation reduction.

Two years later, Heymann and Yoffe [5] studied the stability of duplex paraffin-oil films containing dissolved “polymerized spreaders”. Their films consisted of non-spreading paraffin oil mixed with various amphipathic molecules including carboxylic acids; stand oil; polymerized oleic, ricinoleic, and linoleic acids; and distillation residue from eucalyptus oils. In addition to a comprehensive explanation of oil-film spreading and stability on the water surface, these authors report evaporation reduction by 5 and 10-µm films of a stand oil/mineral oil mixture. For a 5-µm film, evaporation reduction decreased from 80 to 60 % over the course of the experiment, whereas that for a 10-μm film remained relatively constant at 80 %. Measurements of the equilibrium oil/water, water/air, and oil/air interfacial and surface tensions indicated that the studied films have positive initial and negative equilibrium spreading coefficients. Thus, the films were susceptible to dewetting (see §3.2), but the "rigidity" [5] of the additive-stabilized films rendered them impervious to lens formation for as long as 18 months. As a result, the films effectively reduced water evaporation over this time period. A physical explanation of "rigidity" does not appear in the article. Apparently, exposure to oxygen causes the added spreaders to polymerize over time [44].

Langmuir and Schaefer in 1943 [8] carefully investigated the role of surfactant monolayers and duplex-oil films in evaporation reduction of water. Duplex-oil films of oxidized turbine oil and Aroclor (a mixture of polychlorinated biphenyls) were spread over water at thicknesses varying from 120 nm to 1 μm in what is now called a "Langmuir trough" with moveable barriers. A desiccant-containing receiving chamber placed 2 mm above the air/water surface absorbed the evaporated water vapor, and was weighed periodically to ascertain the evaporation rate. Careful calibration of the instrument allowed estimation of the gas-phase mass-transfer resistance, as well as the vapor concentration at the air/water and air/desiccant interfaces. No mention was made of any difficulties in obtaining uniform stable films.

Langmuir and Schaefer were apparently the first to suggest that duplex-oil films impede water evaporation by a diffusive mechanism. The resistance of a duplex-oil film to water transport is $R_F = L/Dk$, where L is the film thickness and Dk is the permeability of the oil film to water, i.e., the product of the diffusion coefficient of water in oil, D, and the equilibrium partition coefficient of water in oil, k. Thus, if water has no solubility in the spread oil film, evaporation halts. The experiments of Langmuir and Schaefer [8] exhibited a linear dependence of measured mass-transfer resistance on film thickness, supporting the proposed diffusive mechanism. Film resistance approached zero as the film thickness approached zero, indicating no interfacial resistance at either the water/oil or oil/air interfaces. By fitting their experimental data to theory, Langmuir and Schaefer found permeabilities, *Dk*, of water in oxidized turbine oil and Aroclor of $2.1\text{x}10^{-5}$ and $3.9\text{x}10^{-5}$ cm^2/s, respectively. It is important to report film water permeability rather than percentage evaporation reduction because *Dk* is a material property of the film. Conversely, evaporation reduction depends on the specific measurement apparatus and on environmental conditions (see §4.2) in addition to film thickness. Similar to Sebba and Briscoe [7], Langmuir and Schaefer discovered that monolayers of tricosanoic acid (C_{23}) at a surface pressure of 55 mN/m exhibit a resistance of 62 s/cm, significantly higher than that of a duplex-oil film 1-µm thick, with a resistance of 5 s/cm. No explanation was offered for this seemingly counterintuitive finding.

In the same year, Powell [45] studied water evaporation through films of mineral oil, vacuum oil, and a mineral oil oxidized during use in steel quenching (referred to as “AO”). Glass dishes containing evaporating water were placed in a wind tunnel at different air speeds directed parallel to the evaporating surface. From the evaporation rate of pure water, the mass-transfer boundary-layer thickness in the air was determined as a function of air speed. Most of Powell’s work focused on relatively thick films between 2 and 25-mm thick that strictly lie outside the realm of duplex films. A few thinner films, however, were studied between 280 nm and 70 µm. For films of AO and oxidized vacuum oil, Powell determined the water permeability of both oils at 22 °C as $3\text{x}10^{-5}$ cm^2/s, similar to Langmuir and Schaefer’s results. At an air speed of 5.4 km/h, a 510-nm thick oil film reduced the water-evaporation rate by almost 90 %. Powell mentions that thinner films are difficult to study because they break up into lenses or are blown to one side of the dish. In agreement with the earlier studies of Rideal [2] and Langmuir and Langmuir [46], increasing the air speed reduced the gas-phase mass-transport resistance resulting in greater evaporation reduction. Thus, both oil-film and gas-phase resistances contribute to the overall water-evaporation rate.

In 1948, Gilby and Heymann published a comprehensive study of evaporation reduction by duplex-oil films including the effects of spreader molecules, film thickness, and gas-phase resistance [47]. A battery of evaporation experiments was conducted with films of 2 wt% polymerized spreader mixed with paraffin oil and deposited over a range of thicknesses from 1-100 µm. Spreaders were similar to those of Heymann and Yoffe [5]: stand oil, eucalyptus residue, polymerized oleic acid, and linseed oil. To explore the effects of the air environment on evaporation reduction, the authors varied air speed, relative humidity, and ambient pressure. Airflow was directed parallel to the evaporating surface in a laminar wind tunnel over the range 1.6 to 12.9 km/h. To investigate the role of humidity, water was also evaporated from dishes placed in a sealed desiccator containing 96 % sulfuric acid. Additionally, the same desiccator with sulfuric acid was evacuated to 15 mm Hg to eliminate most of the air. Apparently, Gilby and Heymann [47] were the first to observe the films visually during evaporation. They reported nonuniform films at thicknesses less than 10 µm, exhibiting changing interference patterns. Evaporation rates were reported as “relative evaporation resistance”, or J_0/J_F, where J_0 is the molar evaporation flux of water from a clean surface and J_F is the corresponding molar evaporation flux of water through an oil film under the same nominal conditions. The authors present a resistance-in-series theory for predicting evaporation rate including an interfacial resistance to evaporation by a structured layer of spreader molecules at the water/oil interface. As with previous theories, no evaporative cooling of the air/water surface was accounted for, which greatly simplifies the expression for J_0/J_F. Unfortunately, the assumption of isothermal evaporation is not accurate.

Gilby and Heymann [47] demonstrated significant evaporation resistance for duplex-oil films containing several different polymerized spreaders under various gas-phase conditions. Reduction of the gas-phase mass-transfer resistance by increasing wind velocity or by applying vacuum increased evaporation reduction. A 5-µm film of eucalyptus oil in paraffin oil reduced water evaporation by 79 % in still air, but by 97 % under a 12.9-km/h wind. For all film thicknesses, flow conditions, and air environments, the magnitude of evaporation reduction depended on the spreader molecule chosen. For films containing 2 wt% spreader, the spreaders listed in the order from most-to-least effective at reducing evaporation were: eucalyptus oil > stand oil > polymerized oleic acid > linseed oil. That evaporation reduction depends on the chemical nature of the spreader supports the authors' claim that the studied spreader molecules form resistive interfacial films at the water/oil interface. As further proof of this assertion, Gilby and Heymann [47] cite earlier experiments [5] in which after the duplex-oil films retracted into lenses, a visible semi-solid "skin" remained between the lenses that still reduced evaporation substantially. Unfortunately, Gilby and Heymann only report relative humidity and ambient temperature for two experiments, and apparently never measure the water-surface temperature. Because they only report J_0/J_F, calculation of the film and air resistances is not possible and quantitative comparison to their data is compromised.

Interest in duplex-oil films as evaporation-reducing agents subsided significantly after the 1940s. To our knowledge, only one more paper appeared in the literature. In 1965, Fox [48] reported improved evaporation reduction over the traditional oil-surfactant duplex films by adding wax particles to the oil film. Details of the type of oils, surfactants, and waxes were not included other than that the oil and wax were petroleum based. Temperature or airflow was not listed. According to Fox, films of the oil/wax/surfactant system spread at approximately 1- and 10-μm thickness reduced water evaporation by 46 and 98 %, respectively, for as long as 20 days. A comparable oil-surfactant system without wax particles reduced evaporation by 25 and 82 % at approximately 1- and 10-μm thickness, respectively.

Understanding of water-evaporation reduction by duplex-oil films remains opaque. Only two studies report the relative humidity and ambient temperature. No study measures the water/air surface temperature, which controls the interface vapor pressure and, hence, the evaporation rate. Calculation of the oil-film and air resistances, therefore, is not possible. Except for Langmuir and Schaefer [8] and Powell [45], all investigations give values only for the evaporation ratio J_F/J_0. Accordingly, quantitative comparison among the various studies is also not possible. We re-emphasize the importance of reporting material properties of the coating oil film (i.e., *Dk*) in addition to evaporation reduction. To achieve this task, temperatures of the water/oil and oil/air interfaces must be known.

2.2 Lipid duplex films

In the 1960s, vision-science researchers initiated studies of the 100-nm lipid layer, i.e., meibum, spread over the human tear film upon each blink. The goal was to understand the physiologic role that meibum plays in the anterior eye [19, 21, 33, 40, 49]. The lipid layer, a complex viscous mixture of long-chain wax and cholesteryl esters, diesters, triglycerides, and polar lipids with currently over 100 different identified species [50-58], was assumed to reduce tear evaporation significantly [21, 22, 32]. As research began to link increased tear evaporation with dry-eye symptoms [28, 59-67], studies sought to understand how the lipid layer reduces tear evaporation. Lowering tear-evaporation rate, thereby maintaining a thicker tear film, might mitigate dry eye.

Mishima and Maurice [21] and later Iwata *et al.* [32] performed *in-vivo* studies on rabbit eyes indicating that the lipid layer reduces tear-evaporation rate. Mishima and Maurice indirectly measured evaporation by filling the anterior chamber of the rabbit eye with paraffin oil and measuring corneal thinning using pachymetry. By assuming that water lost from the cornea was due only to evaporation, they measured the thinning rates before after the meibomian glands had been cauterized and the ocular surface washed. After this treatment, the corneal thinning rate was about 15 times greater. Following corneal wash, the authors smeared previously collected rabbit meibomian secretion over the cornea and closed the eye. Upon opening the eye, the lipid layer re-formed and corneal thinning subsided. Thinning rates were not reported, but apparently the lipid layer reduced evaporation by a factor of 10 to 20. It remains unclear whether the lipid layer reformed over an intact tear film or directly over the corneal surface. The study leaves many questions unanswered, but qualitatively validates evaporation reduction by the lipid layer.

Later, Iwata and colleagues [32] affixed a plastic chamber to the cornea of an anesthetized rabbit before and after the lipid layer was removed. In an effort to be quantitative, evaporation rates from the tear film into dry air flowing through the chamber were measured by weighing the amount of moisture extracted from the effluent air by anhydrous $CaCl_2$. Citing Langmuir and Schaefer's work [8], Iwata *et al.* [32] reported mass-transfer resistance in addition to evaporation reduction. By comparing evaporation rates measured with and without the lipid layer present, Iwata *et al.* attributed a mass-transfer resistance of 13 s/cm to the rabbit lipid layer, corresponding to 75 % evaporation reduction in their apparatus. If we assume a lipid-film thickness of 100 nm, this translates into a water permeability in rabbit lipid of 10^{-6} cm^2/s, which is an order of magnitude smaller than that observed for the most impermeable mineral-oil films reported by Langmuir and Schaefer [8]. However, *in-vivo* experimental conditions are difficult to control precisely. To remove the lipid layer, the entire tear film was rinsed with physiologic saline solution, and the cornea was wiped clean with tissue. The rabbit was prevented from blinking, so the thickness and constitution of the lipid-less tear film are likely not those of the native tear film. Additionally, the airflow rate through the chamber during lipid-less tear evaporation was significantly less than that with the lipid-layer present. Consequently, quantitative reliability of the reported evaporation rates is suspect.

Brown and Dervichian [33] were apparently the first to measure evaporation reduction by human-meibum films *in vitro*. Their experiments were mostly qualitative with few experimental parameters controlled. Human meibum was spread over aqueous saline warmed to 35-40 °C in glass beakers; water mass loss was followed over time. No difference was detected in the evaporation rates among saline-filled beakers with and without spread meibum films, even compared to water in beakers placed in a desiccator. The authors placed meibum on the water/air surface until lenses appeared, so the film thickness was unknown and nonuniform. Additionally, gas-phase resistance was not ascertained. As a result, the experiments of Brown and Dervichian are inconclusive.

Despite a growing understanding of the role of TFLL in dry-eye disease, subsequent decades focused only on *in-vivo* evaporation rates [20, 28, 59-73]. Tomlinson *et al*. [70] recently reviewed essentially all published studies reporting evaporation rates from human healthy and dry eyes. *In-vivo* tear evaporation is typically measured by one of three methods. Commonly, a sealed goggle is placed over the eye and the humidity increase of stagnant air in the goggle is measured [63, 72]. A second goggle method measures the humidity gradient between two points near the ocular surface in uncontrolled flow conditions [71]. A few goggle experiments operate under forced-flow conditions [60, 73]. Regardless of the method employed, it is impossible to remove and reconstitute the lipid layer, so only comparative evaporation rates are available. Although qualitatively useful for developing correlations between lipid-layer appearance and evaporation rate [20], available *in-vivo* studies are not quantitative. Tear-surface temperature, lipid-layer thickness and coverage, and vapor-phase mass-transfer dynamics are all unknown and can vary significantly among people and between studies.

No fundamental *in-vitro* evaporation-reduction studies appeared until 2009, driven primarily by the desire to produce a palliative for dry-eye sufferers. In early 2009, Borchman *et al.* [13] investigated the possible role of tear-film components on water evaporation determined by mass lost over time. Water evaporated at 25 °C and 40 % relative humidity for most experiments. The surface temperature of the water, which is assuredly cooler than 25 °C, was not reported. Although numerous proteins, salts, and mucins were mixed with the water to form artificial tear, only those solutions covered by a mimic lipid film showed any effect on evaporation. A 1:1 mixture of palmityl oleate and *n*-tetradecane served as the artificial lipid layer. Evaporation reduction was minimal: an 85-μm lipid film reduced evaporation by only 27 %. Duplex-oil films of palmityl oleate and tetradecane (1:1 vol:vol) have not been previously probed, but available data suggest duplex films this thick should reduce evaporation more drastically [5, 8, 45, 47]. In our experience, stearyl-oleate films mixed with mineral oil initially spread, but rapidly break up into lenses. Unfortunately, no visual examination was performed on the duplex films of Borchman *et al.* during evaporative loss. As Borchman *et al.* note, their films were not uniform during evaporation, resulting in unreliable data.

Later that same year, Herok *et al*. [14] investigated the role of human meibum and meibum mimics in water-evaporation reduction. Meibum was collected from humans, rabbits, and bovines. Mixtures of dipalmitoyl phosphatidylcholine (DPPC) and cholesterol in varying ratios served as meibum mimics. Evaporation was measured gravimetrically by TGA in a ceramic crucible containing water covered by lipid spread from hexane. Air temperature was controlled, and airflow was directed upward around the crucible. Relative humidity was not measured. For human meibum, evaporation reduction increased monotonically from 0 to 7 % as the film thickness increased from 26 nm to 4 µm. Results for rabbit- and bovine-meibum films were nearly identical to those of human-meibum films over the same range of film thickness. Similar to Brown and Dervichian [33], meibum layers did not reduce evaporation significantly, even for thick duplex films. As with Brown and Dervichian [33] and Borchman *et al.* [13], however, no visual examination of the lipid layer during water evaporation was pursued, and no information on water-surface temperature was given.

With the small crucible utilized by Herok *et al.*, water temperature should be close to ambient. From the evaporation rate reported for a clean water surface and an estimated 30 % relative humidity, we calculate a gas-phase mass-transfer coefficient, k_m, of 0.04 cm/s. As discussed later (§4.2), this means that the gas-phase resistance is much larger than the resistance of the lipid film and likely sets the evaporation rate independent of lipid-film presence. Thus, in addition to likely film dewetting into lenses, the reported evaporation rates were controlled by gas-phase resistances and appear of limited applicability.

Vision scientists have also investigated *in-vitro* evaporation through monolayers of lipid molecules [74, 75] even though the human lipid layer is a duplex film near 100-nm thick, well above the thickness of a monolayer [16, 19, 49, 76-81]. Miano *et al*. [74] found that monolayers of bovine meibum, dipalmitoyl phosphatidylcholine (DPPC), and cholesteryl palmitate spread at surface pressures of ~30 mN/m reduced water evaporation from a pendant drop by 30, 10, and 2 %, respectively. Recently, Rantamäki *et al*. [75] measured evaporation reduction by monolayers of phosphatidylcholine (PC), behenyl alcohol, and behenyl oleate. Although PC had no effect on water evaporation, behenyl alcohol and behenyl oleate monolayers reduced evaporation by 45 and 23 %, respectively. Applicability of these results to the human tear film is limited to possible monolayers present in dewetted areas of the tear-film lipid layer. The tear-film lipid layer does apparently demonstrate dewetting for some individuals [82].

Lack of *in-vitro* corroboration for water-evaporation reduction by duplex meibum films is surprising. Although meibum is more polar than surfactant-mineral oil systems, meibum is 3-4 orders of magnitude more viscous [83, 84]. Thus, we expect reduced diffusivity of water dissolved in meibum, and hence, reduced evaporation rates, especially for thick meibum films. A rigorous set of *in-vitro* experiments similar to those conducted on petroleum-based duplex films is requisite. To design a reliable, quantitative experiment requires, first, that the duplex lipid films spread and remain stable over the air/water interface during the period of evaporation.

3. Duplex films

A primary challenge for reducing water evaporation with duplex-oil films is achieving a uniform-thickness film that remains stable long enough to affect evaporation rates. The oil layer must initially spread over the aqueous surface into a uniform-thickness duplex film and must resist dewetting over a timescale relevant to evaporation measurement. For large water reservoirs, this timescale may be weeks to months. On the eye, it is seconds since the tear film reforms after each blink. In most laboratory experiments, the oil film must last minutes to hours. Unfortunately, duplex-oil films are unstable and dewet, often rapidly. Therefore, understanding oil-film spreading and dewetting is necessary to engineer duplex films for possible evaporation reduction.

3.1 Spreading

Detailed discussions of the thermodynamic theory of spreading (i.e., spontaneous formation of a thin, immiscible, and uniform layer) date back to the early 1900s [4, 5, 85]. We briefly summarize those findings. Consider a macroscopic oil lens initially at the water/air interface as shown in Fig. 1A. The Helmholtz free-energy change, ΔF, for a completely immiscible lens to relax at fixed temperature and lens volume into a slightly more elongated shape illustrated in Fig. 1B is

$$\Delta F = \gamma_w \Delta A_{wa} + \gamma_o \Delta A_{oa} + \gamma_{ow} \Delta A_{ow} \tag{1}$$

where γ_w, γ_o, and γ_{ow} are the constant water/air, oil/air, and oil/water surface and interfacial tensions, respectively, and ΔA_{wa}, ΔA_{oa}, and ΔA_{ow} are the respective changes in the water/air, oil/air, and oil/water interfacial areas. In Eq. 1, we neglect the contribution of line tension at the three-phase contact line because our lenses are larger than microns in extent [86, 87]. For a thin lens with a small lens angle, we approximate that the area changes as $-\Delta A_{wa} = \Delta A_{oa} = \Delta A_{ow} = \Delta A$. Consequently, in the limit as $\Delta A \rightarrow 0$, the differential free-energy change is

$$-dF/dA = \gamma_w - \gamma_o - \gamma_{ow} \equiv S \tag{2}$$

where S is defined as the spreading coefficient. If the free energy decreases as the lens elongates, then $S > 0$, and the lens spreads. Conversely, if the free energy increases as the lens expands, $S < 0$, and the oil remains as a lens. Importantly, the interfacial tensions can change with time when the oil and water phases are not pre-equilibrated. To reflect this change, initial and final (equilibrium) spreading coefficients, S_0 and S_∞, are distinguished. Whereas the initial spreading coefficient, S_0, may be negative or positive, a large body of experiment and theory shows that the equilibrium spreading coefficient must be less than or equal to zero for any immiscible liquid droplet deposited on water [4, 88, 89]. Fortunately, a positive initial spreading coefficient is often enough to form initially a duplex-oil film.

For pure aliphatic hydrocarbons of molecular weight larger than that of octane, the initial spreading coefficient is negative [90]. Consequently, mineral oils and long-chain hydrocarbons that are typically used as duplex-oil films in evaporation studies do not spread on water, even initially. To obtain a duplex film from these oils, S_0 must be rendered positive. One way to increase S_0 is to dissolve the oil into a volatile solvent with a positive initial spreading coefficient. A thin oil layer is left behind after spreading and solvent evaporation. Unfortunately, the final deposited layer is rarely uniform, unless the oil itself has a positive initial spreading coefficient.

To induce spreading, small amounts of oil-soluble surfactants, such as fatty acids or fatty alcohols, are dissolved into the oil. Heymann and Yoffe [5] refer to these additives as "spreaders". Water-soluble surfactants are ineffective in this role because they partition predominately into the water phase and lower γ_w, which makes S more negative. Oil-soluble spreaders, however, lower the water/oil tension and the oil/air tension, thereby raising the spreading coefficient. With the appropriate amount of oil-soluble spreader, the initial spreading coefficient is positive, and the oil initially spreads as a duplex film. Unfortunately, spreader molecules soon escape from the spreading oil to adsorb at the water/air interface of the expanding triple line [4, 5]; the water/air surface tension falls. A building water/air surface pressure slows, and eventually stops, the spreading oil film. At equilibrium, spreader molecules partition between the bulk oil and the oil/water, oil/air, and water/air interfaces such that the tension at all interfaces declines. As mentioned previously, for all pure and spreader-containing liquids measured, the equilibrium spreading coefficient is negative. Accordingly, the initially spread oil film subsequently dewets.

3.2 Dewetting

Dewetting at the fluid/fluid interface is a kinetic process by which an initially spread, immiscible liquid film rearranges into lenses. An equilibrated duplex-oil film must dewet (i.e., $S_\infty < 0$). The first kinetic step in dewetting is the formation of holes in the film [91, 92]. Once a hole forms, it expands and others form to collapse the film into rivulets that eventually gather into lenses [91] (see graphical abstract). We follow Sharma and Ruckenstein [93] to predict the stability of duplex-oil films against hole formation.

Consider a duplex-oil film of initial uniform thickness L_0 on water as shown in Fig. 2A. If a hole of radius r_0 forms and ruptures the film, then the oil film initially takes the shape illustrated in Fig. 2B with thickness L. For holes of radius much smaller than the overall dimension of the film, the change in film thickness is negligible and $L \sim L_0$. The change in free energy corresponding to formation of a hole is then [93, 94]

$$\Delta F = F_{hole} - F_{film} = \left(\frac{1}{2} \tilde{\rho} g L_0^2 + S \right) A_H + \gamma_o \left(A_H + A_1 - A_{H1} \right) + \gamma_{ow} \left(A_H + A_2 - A_{H2} \right) \qquad (3)$$

where $\tilde{\rho} = \rho_o (1 - \rho_o / \rho_w)$, ρ_o and ρ_w are oil and water densities [kg/m^3], g is the gravitational acceleration constant [m/s^2], $A_H = \pi r_0^2$ is the area of the hole at the air/water interface, A_1 and A_2 are the areas of the oil/air and oil/water surfaces from $r = r_0$ to $r = r_1$ and $r = r_2$, respectively, $A_{H1} = \pi r_1^2$, and $A_{H2} = \pi r_2^2$. Hole radii r_1 and r_2 at the oil/air and oil/water interfaces are labeled in Fig. 2B. Evaluation of ΔF requires the interface profile, $r(z)$, as described by Eq. A.7 in Appendix A. Eq. 3 accounts for changes in gravitational-potential energy and surface energy, i.e., S. Strictly, duplex-oil films are thin enough for gravity to be negligible. Gravity is included here for completeness. ΔF decreases when S is negative because hole formation becomes favorable by exposing a low-energy water/air interface. Favorable hole formation is counteracted by an increase in free energy due to creation of high-energy oil/air and oil/water interfaces around the hole rim, as well as due to increasing the overall height of the duplex-oil film. Above a critical film thickness, L_c, $\Delta F \geq 0$, and hole formation is unfavorable. With $r(z)$ specified by Eq. A.7, evaluation of Eq. 3 at $\Delta F = 0$ gives the critical thickness L_c as

$$L_c = r_0 f(\gamma_w, \gamma_o, \gamma_{ow}, g) \tag{4}$$

where the function f is calculated in Appendix A, and takes on values between 0.1 and 1 for the range of typical surface energies. The critical film thickness, L_c, is directly proportional to the hole radius, r_0, so a film of initial thickness L_0 is unstable to holes of radius r_0 larger than L_0/f and stable to smaller holes. For a duplex-oil film initially covering a water/air area of radius r_A, the largest possible hole radius $r_0 = r_A$. Thus, any film of initial thickness $L_0 < r_A f$ is unstable to hole formation and rupture. Conversely, no holes may form in duplex-oil films of thickness $L_0 > r_A f$, guaranteeing the stability of thick films. For example, the exposed area of the eye has a radius, $r_A \sim 5$ mm, so any oily duplex film covering this area and thinner than about 2.5 mm is unstable to rupture into lenses. Since the tear-film lipid layer on the eye is ~100-nm thick, it is unstable to holes of $r_0 > 200$ nm. Hole formation is documented both in the *in-vivo* tear-film lipid layer (TFLL) [82] and in model films of oxidized mineral oil [91]. Measured holes in a TFLL about 50-nm thick were ~1-2 µm in radius [82]; those in a 100-nm thick mineral-oil film were ~100 µm in radius [91]. Such hole radii are consistent with Eq. 3 since film thicknesses are well below the critical thickness.

For large holes of radii near 1 cm, the critical film thickness is large enough for the gravitational-energy and the spreading-coefficient terms to dominate Eq. 3. In this limit, we recover the expression for critical thickness given by Wyart *et al*. [92], $L_c = \left(-2S/\tilde{\rho}g\right)^{1/2}$ that ignores the contribution of curvature near the three-phase contact line towards creating high-energy surface area.

Since duplex-film dewetting of a nonvolatile oil appears inevitable, the best scenario is to slow the process. An understanding of the physics underlying dewetting dynamics is, therefore, necessary. Considerable information is available on dewetting of thin liquid films on solid substrates [95]. Unfortunately, the dynamics of dewetting on liquid substrates has attracted far less attention [92, 94, 96]. The physics is similar, except substrate hydrodynamics can be important. Liquid/liquid dewetting has four stages: initial rupture, hole growth, hole coalescence, and retraction into lenses. The ability of a duplex-oil film to reduce water evaporation is already compromised during the first stages of dewetting when holes begin to form and expand. Attractive Hamaker forces between the oil/air and oil/water interfaces destabilize the thinnest duplex films nearing 100 nm in thickness [92], whereas thicker duplex-oil films apparently destabilize due to contamination by foreign particles such as dust [5]. Once holes form, they expand at a rate that depends on the interfacial tensions and the substrate and film viscosities [92]. The more negative is the spreading coefficient and the less viscous are the fluids, the faster the film dewets. To slow dewetting, spreadable and viscous films must be engineered. Accordingly, Heymann and Yoffe [5] used polymerized spreaders that lowered the final spreading coefficient and increased the film viscosity. In fact, the chosen spreaders apparently solidified over time, allowing films to resist dewetting for months [5]. We consider next water evaporation through duplex-oil films.

4. Water evaporation

Evaporation of water is not a simple process. In addition to molecular properties, it depends on water-concentration profiles both in the liquid and in the surrounding vapor. Therefore, evaporation rate depends on system geometry and convective heat and mass transfer in the liquid and vapor phases. Evaporation through a duplex-oil or lipid film is more involved. We consider steady-state water evaporation from a quiescent, locally flat substrate into humid air with known airflow, first for a clean-water surface, and then for a water surface covered with an oily film of uniform thickness. The resulting analysis predicts the evaporation rate through duplex-oil films. If appropriate temperatures and humidities are measured in addition to the evaporation rate, the model equations provide the desired water permeability of the oily film, *Dk*.

4.1 Pure water

Escape of water molecules from a clean surface into pure water vapor occurs via molecular kinetics. Gas-kinetic theory of Hertz and Knudsen (HK) [97, 98] describes the evaporative flux as

$$J_k = \alpha\left(\frac{1}{2\pi M R_g}\right)^{1/2}\left[\frac{P_w^{sat}(T_S)}{T_S^{1/2}} - \frac{P_w}{T_\infty^{1/2}}\right] \tag{5}$$

where J_k is the molecular-kinetic evaporative flux [mol/m^2/s], M is the molar mass of water [g/mol], R_g is the universal gas constant, T_S and T_∞ are the temperatures [K] of the liquid surface and gas far away from the surface, respectively, $P_w^{sat}(T_S)$ is the vapor pressure of water in equilibrium with the water surface at temperature T_S, and P_w is the partial pressure of water vapor in the bulk gas phase. The first term in the brackets on the right of Eq. 5 corresponds to evaporation and the second term to condensation. α is an evaporation (or condensation) coefficient indicating that only a fraction of the molecules colliding with the interface evaporate (or condense) and is usually adjusted to give agreement between experiment and theory [99]. Extensions of HK theory account for differences between evaporation and condensation coefficients and for non-equilibrium velocity distributions [100, 101]. When experiments are carefully controlled under vacuum conditions, the evaporation coefficient approaches unity [3, 100, 102, 103].

Upon expressing the vapor partial pressure as concentration by the ideal gas law, HK theory simplifies to

$$J_k = \alpha \left(\frac{R_g}{2\pi M} \right)^{1/2} \left[C_w^{sat}(T_S) T_S^{1/2} - C_{w\infty}^G T_\infty^{1/2} \right] \qquad (6)$$

where C_w^{sat} is the molar water-vapor concentration in equilibrium with the liquid phase at T_S and $C_{w\infty}^G$ is the molar concentration of water in the vapor phase far from the interface at temperature T_∞. If liquid water is in contact only with its own vapor, then the evaporative flux is well-described by Eq. 6 [3, 100, 102, 103].

In practice, however, evaporation rates are almost always measured at atmospheric conditions instead of under vacuum. When an evaporating water surface is exposed to air, water molecules must not only escape the surface but must also transport through the air molecules by convective-diffusion as illustrated by the concentration profile in Fig. 3. Convective-diffusion in the air substantially slows the evaporation rate. Water molecules still vacate the surface over the distance λ in Fig. 3 at the rate J_k in Eq. 6, where λ is about the mean-free path of molecules escaping from the water/air surface. The surface temperature, T_S corresponds to an average over this distance. Beyond the interfacial zone ($z > \lambda$), collisions with air molecules demand that water vapor travels by convection or diffusion through the air. Without special precautions to eliminate environmental air currents and temperature gradients, it is difficult to evaporate by molecular diffusion alone. Hence, convective-diffusion must be accounted for.

Convective-diffusion mass-transfer flux follows a form analogous to Newton's law of cooling [104, 105]: $J_c = k_m \Delta C$ where k_m is the mass-transfer coefficient of water in the gas phase [m/s] and ΔC is concentration difference driving the evaporative flux

$$J_c = k_m \left(C_{w\lambda}^{G} - C_{w\infty}^{G} \right) \tag{7}$$

where $C_{w\lambda}^{G}$ and $C_{w\infty}^{G}$ are the water-vapor concentrations [mol/m^3] at $z = \lambda$ and in the environment far from the surface, respectively. When there is gas-phase resistance to water transport, HK theory becomes

$$J_k = \alpha \left(\frac{R_g T_S}{2\pi M} \right)^{1/2} \left[C_w^{sat}(T_S) - C_{w\lambda}^{G} \right] \tag{8}$$

where T_S is the water temperature at the water/air interface. Eq. 8 specifies the rate at which water molecules in the interfacial region escape the surface. Molecules in the surface region are presumed to remain in thermal equilibrium. At steady state, no mass accumulates at the $z = \lambda$ plane. Accordingly, the two fluxes in series J_k and J_c, are equal, giving the overall evaporative flux of water, J, as

$$J = J_k = J_c = \frac{\left[C_w^{sat}(T_S) - C_{w\infty}^{G}(T_\infty) \right]}{R_k + R_m} \tag{9}$$

Thus, J is proportional to the overall concentration driving force between the vapor at the water surface and that in the bulk air, and inversely proportional to the series resistances of molecular-kinetic escape, R_k and convective-diffusion, R_m, defined from Eqs. 7 and 8, respectively, as

$$R_k = \frac{1}{\alpha} \left(\frac{2\pi M}{R_g T_S} \right)^{1/2} \tag{10}$$

and

$$R_m = 1/k_m \tag{11}$$

The molecular-kinetic resistance for water evaporation is calculated to be ~10^{-4} s/cm from 20-37 °C. The convective mass-transfer resistance depends on the type and magnitude of airflow at the water surface. Expressions for mass-transfer coefficients are well documented for a variety of geometries and gas flows both parallel and perpendicular to the surface [104-107]. The water-vapor mass-transfer coefficient, k_m, typically ranges from roughly 0.5-10 cm/s for airflow both parallel and perpendicular to a flat plate over flow velocities from 0.1-10 m/s (Re ~ 300-3000). Thus, the practical range of the mass-transfer resistance is approximately R_m ~ 0.1-2 s/cm. Even at the highest value of the mass-transfer coefficient, the ratio of R_k/R_m ~10^{-3}. In completely diffusion-controlled evaporation (i.e., zero airflow), the mass-transfer resistance is even higher than that for convective-controlled mass transfer. Therefore, for most all foreseeable experimental conditions in air, water evaporation is gas-phase mass-transfer controlled. The resistance to kinetic escape from the surface is minimal. Only in a vacuum that eliminates air does the mass-transfer resistance disappear allowing water to evaporate at rates predicted by molecular kinetics [1, 2, 102]. One important exception is evaporation from micron-sized or smaller droplets. When the drop radius approaches the mean-free path of molecules in the gas, the kinetic resistance dominates because there is effectively a vacuous shell encompassing the sphere [108, 109]. Consequently, we neglect the molecular-kinetic resistance of the water surface in subsequent discussion.

4.2 Duplex-film covered water

4.2.1 Mass conservation

When the water surface is covered by an immiscible duplex-oil film, additional series resistances appear; Eq. 9 requires modification. We adopt a one-dimensional mass- and heat-transfer model. Corresponding schematics of water-concentration and temperature profiles are shown in Fig. 4. The duplex-oil film, of thickness *L*, is bounded by two interfaces: water/oil and oil/air, with bulk oil in between. Following Langmuir and Schaefer [8], we assume a dissolution-diffusion mechanism to describe water transport through the duplex-oil film. That is, water first dissolves into the oil and then diffuses through the duplex film. Upon neglect of interfacial resistances, Fick's law describes the steady mass flux of water through the oil film:

$$J_F = \frac{D}{L}\left[C_{w0}^F(T_{wo}) - C_{wL}^F(T_{oa})\right] \qquad (12)$$

where J_F is the molar water flux [mol/m^2/s], D is the diffusion coefficient of water in the oil [m^2/s], L is the thickness of the oil film [m], and C_{w0}^F and C_{wL}^F are water concentrations [mol/m^3] in the oil film at the water/oil and oil/air interfaces at temperatures T_{wo} and T_{oa}, respectively. In most cases, gas-phase convection is present. The molar flux of water vapor through the air then follows as

$$J_c = k_m\left[C_{wL}^G(T_{oa}) - C_{w\infty}^G(T_\infty)\right] \qquad (13)$$

where J_c is the molar flux [mol/m^2/s] of water vapor through the air, k_m is the mass-transfer coefficient of water vapor in air [m/s], and C_{wL}^G and $C_{w\infty}^G$ are the water-vapor concentrations at the oil/air interface and in the environment far from the interface, respectively.

At steady state, the water flux through the bulk oil film and that through the air are equal. Further, we invoke local phase equilibrium of water at the water/oil and oil/air interfaces. Since water oil and water are sparingly soluble, the water partition coefficient between liquid water and oil in Fig. 4 is conveniently specified as that between pure water vapor equilibrated with pure liquid water and the immiscible oil film or $k_{wo} = C_{w0}^{F} \big/ C_{w}^{sat}(T_{wo})$. Likewise, the partition coefficient for water between the oil film and air is written as $k_{oa} = C_{wL}^{F} \big/ C_{wL}^{G}$. Since the temperature variation across the duplex-oil film is small, $k_{wo} = k_{oa} = k$. After some algebra, we recover the evaporative flux through a water surface covered with a uniform duplex-oil film and exposed to a water-subsaturated air phase

$$J_F = \frac{C_w^{sat}(T_{wo}) - R_H C_w^{sat}(T_\infty)}{R} \tag{14}$$

where we re-express the concentration of water in the air environment, $C_{w\infty}^{G}$, in terms of the ambient relative humidity, R_H, and the saturation water-vapor concentration at ambient temperature, $C_w^{sat}(T_\infty)$. As in Eq. 9, the overall resistance to evaporation, R, in Eq. 14 is the series sum of that due to water diffusion through the duplex-oil film, $R_F = L/Dk$ and that due mass-transfer through the air phase, $R_m = 1/k_m$:

$$R = R_F + R_m = L / Dk + 1 / k_m \tag{15}$$

where the product Dk is the permeability of water dissolved in the duplex-oil film. Clearly, thick oil films with low water solubility and small water diffusion coefficients in the oil more effectively reduce the evaporation rate. If there are additional interfacial resistances due, for example, to coherent molecular films at the water/oil or oil/water interfaces, it is customary to add an interfacial resistance [47]

$$R = R_I + R_F + R_m = R_I + L / Dk + 1 / k_m \tag{16}$$

where R_I is the mass-transfer resistance of any interfacial molecular film.

Once k_m, humidity, and temperatures are known, Eq. 16 provides the basis for assessing the water permeability of the duplex-oil film, *Dk*, by measuring *R* as a function of duplex-oil thickness, *L* [8]. To obtain the air-phase mass-transfer coefficient, k_m, the evaporation rate from a clean-water surface is ascertained. In this case, $R_I = R_F = 0$, and the evaporation rate, J_0, is

$$J_0 = k_m \left[C_w^{sat}(T_{S0}) - R_H C_w^{sat}(T_\infty) \right] \tag{17}$$

where T_{S0} is the steady-state temperature of the water/air interface, commonly referred to as the wet-bulb temperature [104, 105]. Eq. 17 is identical to Eq. 9 since molecular-kinetic escape from the water surface presents negligible resistance. k_m is established from Eq. 17 given measurement of J_0 provided all other quantities are known including the water surface temperature, T_{S0}.

Next, the evaporation rate in the presence of a duplex-oil film, J_F, is measured. Typically, the evaporation ratio is reported i.e., the ratio of water evaporation through a duplex-oil film to that from a clean surface [7, 45]:

$$\frac{J_F}{J_0} = \frac{R_m}{R_I + R_F + R_m} \frac{\left[C_w^{sat}(T_{wo}) - R_H C_w^{sat}(T_\infty) \right]}{\left[C_w^{sat}(T_{S0}) - R_H C_w^{sat}(T_\infty) \right]} \equiv \frac{R_m}{R} \phi \tag{18}$$

Gilby and Heymann [47], however, report the inverse. Evaporation reduction is simply $1 - J_F / J_0$. The first ratio on the right of Eq. 18 is the fraction of overall mass-transfer resistance due to gas-phase transport. This fraction depends on physical properties of the duplex-oil film as well as on the apparatus geometry and airflow. The second factor, ϕ, is the ratio of concentration driving forces, $\phi = \Delta C_F / \Delta C_0$, where ΔC_F is the overall concentration driving force for an oil-coated surface and ΔC_0 is the overall concentration driving force for a clean-water surface. These two driving forces differ because the temperature at the water/oil interface of the duplex-oil film, T_{wo}, is not the same as the wet-bulb temperature of the free water surface, T_{S0}. Thus, ϕ depends on heat and mass-transfer rates and ambient relative humidity and temperature, in addition to film properties. The thicker is the duplex-oil film, the more it reduces evaporation, and the warmer is the water surface. A warmer water/oil interface leads to a larger ΔC_F and, therefore, to a larger ϕ.

Although the evaporation ratio is often reported [5, 7, 9, 32, 45, 47, 48], direct comparison of values derived from Eq. 18 between different experimental apparatus and conditions must be done with caution since heat and mass transfer rates vary. For this reason, Langmuir and Schaefer [8] reported the water permeability of the duplex-oil film, *Dk*, which is a material property of the film oil alone and enables meaningful comparison. Calculation of the oil-film water permeability from Eqs. 14-18 requires knowledge of the evaporative flux and the concentration driving force. Accordingly, the evaporation rate, water surface temperature, ambient temperature, and relative humidity must all be measured. Thus, to establish *Dk*, it is also critical to establish T_{wo} and T_{S0}.

4.2.2 Energy conservation

As shown in the schematic temperature profile of Fig. 4B, the concentration of water vapor in equilibrium with the water/oil interface of the duplex-oil film, $C_w^{sat}(T_{wo})$, appearing in Eq. 18, depends on the temperature T_{wo} or, in the case of a clean-water surface, on the temperature T_{S0}. Consider a stagnant water substrate heated from below at temperature T_b at ($z = -H$) as in Fig. 4B. Special precautions are necessary to avoid buoyancy-driven convection in the aqueous substrate, as discussed later. With convection eliminated, steady conduction imposes a linear temperature profile through the water substrate with a conductive heat flux, q_S [W/m^2], given by Fourier's law:

$$q_S = \frac{k_w}{H}\left(T_b - T_{wo}\right) \tag{19}$$

where k_w is the thermal conductivity [W/m/K] of the substrate water and H is the substrate thickness [m].

The duplex-oil film is too thin to support natural convection. Thus, conductive heat flux through the film, q_F, is written as

$$q_F = \frac{k_{oil}}{L}\left(T_{wo} - T_{oa}\right) \tag{20}$$

where k_{oil} is the thermal conductivity [W/m/K] of the oil, L is the oil-film thickness [m], and T_{oa} is the temperature at the oil/air interface.

Gas-phase hydrodynamics controls the heat-transfer rate from the oil/air interface:

$$q_c = h\left(T_{oa} - T_\infty\right) \tag{21}$$

where q_c is the heat flux [W/m^2] into the air via convection, h is the convective heat-transfer coefficient [W/m^2/K], and T_∞ is the ambient temperature. The convective heat-transfer coefficient, h, depends on geometry, fluid properties, and airflow rate and direction [104-107].

At the water/oil interface, we demand conservation of energy

$$0 = q_S - q_F - J_F \Delta\tilde{H}_S \tag{22}$$

where $\Delta\tilde{H}_S$ is the molar enthalpy of solution [J/mol] for water dissolving into oil at the temperature of the water/oil interface, T_{wo}. Likewise, at the oil/air interface, we write

$$0 = q_F - q_c - J_F \Delta\tilde{H}_E \tag{23}$$

where $\Delta\tilde{H}_E$ is the molar enthalpy change [J/mol] between water dissolved in oil and water vapor at the temperature of the oil/air interface, T_{oa}. For thin duplex films with a small temperature difference across the film, sensible heats can be ignored and

$\Delta\tilde{H}_S + \Delta\tilde{H}_E = \Delta\tilde{H}_V(T_{wo})$, where $\Delta\tilde{H}_V$ is the latent enthalpy of vaporization of pure water [J/mol] at T_{wo}.

Combination of the heat-flux expressions from Eqs. 19-21 with the energy balances in Eqs. 22 and 23 establishes the water/oil interface temperature as

$$T_{wo} = \frac{1}{U_W + U_F}\left(U_W T_b + U_F T_\infty - J_F \Delta\tilde{H}_V(T_{wo})\right) \tag{24}$$

where we define the following heat-transfer coefficients:

$$U_W = \frac{k_w}{H} \tag{25}$$

and

$$U_F = \left(\frac{1}{h} + \frac{L}{k_{oil}}\right)^{-1} \tag{26}$$

As the duplex-oil film thickness increases, the evaporation rate decreases; from Eq. 24, the temperature rises. In practice, the thinness of duplex-oil films guarantees that $T_{wo} \sim T_{oa}$ to within standard measurement precision. Therefore, we refer to T_{wo} as T_{SF} for simplicity. For a clean-water surface, Eq. 24 simplifies to

$$T_{S0} = \frac{1}{U_W + h}\left(U_W T_b + hT_\infty - J_0 \Delta\tilde{H}_V(T_{S0})\right) \tag{27}$$

This temperature corresponds to the highest evaporation rate and, thus, to the lowest surface temperature (i.e., the wet-bulb temperature). Eqs. 14 and 24 and Eqs. 17 and 27 are coupled and must be solved simultaneously to predict both the evaporation rate and the surface temperature of film-covered and clean surfaces, respectively.

Importantly, T_{SF} and T_{S0} are not equal unless $J_F \sim J_0$, and evaporation reduction is minimal. Failure to account for evaporative cooling of the water surface leads to inaccurate prediction of evaporation reduction. Most previous studies neglect the effect of surface cooling [7, 13, 14, 33, 47]. In our experiments described later, careful attention is paid to determining T_{SF} and T_{S0}.

The two sets of coupled equations, Eqs. 14, 24 and Eqs. 17, 27, describe completely the evaporation rates and surface temperatures from clean and duplex-oil film covered surfaces once all parameters are specified. In practice, however, the goal is to obtain the water permeability of the oil film, Dk, which is an unknown material property of the covering oil. In a well-defined evaporation experiment, all other parameters in the coupled equations are measured or found in literature leaving Dk as the sole fitting parameter. Measurement of the evaporation rate, surface temperature, and humidity from a clean-water surface supplies the mass-transfer coefficient, k_m, by Eq. 17. For impinging-jet flow, the heat transfer coefficient, h, is related to the mass-transfer coefficient by Eq. B.7. Water-evaporation measurements through duplex-oil films yield R by Eq. 14 when the relative humidity and ambient and surface temperatures are known. Measurement of the evaporation rate through duplex-oil films of varying thickness enables fitting a straight line to R versus L that provides Dk and R_I from Eq. 16. Eqs. 24 and 27 are ancillary to the calculation of Dk, but agreement between the measured and predicted values of T_{S0} and T_{SF} confirms the consistency of the experiment and theory.

4.2.3 Nonuniform duplex films covering water

In most studies of evaporation through duplex-oil films, little attention is paid to whether or not the film remains stable and of uniform thickness during the measurement. Here we address briefly the effect of isolated open areas in the film on evaporation rate. Consider a dewetted hole in a duplex film where the underlying water surface is exposed. Most likely, a monolayer (or two) of spreader covers the open hole and reduces evaporation to a certain extent. At most, water evaporates through the hole at the rate of a clean-water surface. Evaporation through a dewetted hole is strictly a two dimensional problem [110, 111]. We adopt a simple 1-D analysis. Water evaporative fluxes through the film-covered and open water surfaces obey the same rate law, but the resistances are different. In the duplex-film-covered surface outside of the dewetted hole, the total mass-transfer resistance is $R_I + R_F + R_m$. Above the dewetted surface, the resistance to evaporation is $R_I + R_m$. Thus, depending on the magnitude of R_F, water evaporates faster through the clean surface, so the overall evaporation rate increases even when the hole is small. Assuming independent 1-D concentration profiles and driving forces outlined in §4.2.1, the measured overall evaporation rate, J_{ov}, is predicted by

$$J_{ov} = \alpha_F J_F + (1 - \alpha_F) J_0 \tag{28}$$

where α_F is the fraction of the total evaporating surface area covered by uniform duplex-oil film. Eqs. 14, 17, and 28 specify the measured overall evaporation reduction as

$$\frac{J_{ov}}{J_0} = \alpha_F \frac{R_m}{R_I + R_F + R_m}\phi + \left(1 - \alpha_F\right)\frac{R_m}{R_I + R_m}\phi \tag{29}$$

The first term on the right of Eq. 29 represents the evaporation reduction by the duplex-film-covered portion of the surface, whereas the second term gives the evaporation through the dewetted monolayer-covered regions.

As shown in §4.2.1, the driving force for evaporation is smaller through a clean surface due to evaporative cooling. In the case of a hole, however, the water-surface temperature is not likely lowered to the wet-bulb temperature since the surrounding duplex-film-covered surface is warm. If we assume that the temperature of the water surface in the dewetted hole is close to that of the water/oil interface of the duplex film, then the concentration driving forces are the same for the dewetted hole and the oil-covered surface, and $\phi = 1$ in Eq. 29.

Consider for simplicity, a water substrate with ϕ = 1 covered by a uniform duplex-oil film such that J_F/J_0 = 0.90. If 5 % of the oil-film surface area dewets, Eq. 29 predicts that J_{ov}/J_0 = 0.91, a minimal change. However, for a thicker oil film covering the water surface with J_F/J_0 = 0.10 and for the same 5 % extent of dewetting, Eq. 29 predicts that J_{ov}/J_0 = 0.15. The same dewetted area now causes a 50% increase in measured evaporation ratio giving similar error in the duplex-film water permeability. Thus, the effect of oil-film nonuniformity in evaporation reduction is larger for more impermeable oil films, and can be significant. Langmuir and Schaefer [8] emphasized this effect in mixed monolayers of cetyl alcohol and the more permeable oleic acid. Archer and La Mer [112] documented a similar phenomenon. We later utilize these findings in interpretation of our experimental results.

5. Materials and methods

5.1 Materials

We measure evaporation reduction through two types of duplex-oil films. The first is an admixture of oxidized light mineral oil (MOx) (8042-47-5, Fisher Scientific, Fair Lawn, NJ) and bovine submaxillary mucin (BSM) (Worthington Biochemical Corp., Lakewood, NJ). We abbreviate this admixture as MOx/BSM. Mineral-oil oxidation was carried out following Blodgett [37]. Viscosity measurements of the oxidized mineral oil were performed on a Physica MCR301 rheometer (Anton-Paar, Ashland, VA) with a 25-mm diameter flat-plate geometry at shear rates between 1 and 10^3 s^{-1} and a 500-µm gap size, giving 63 and 25 mPa·s at 20 and 35 °C, respectively. With the viscosity known, the Siddiqi-Lucas correlation [113] predicts the diffusivity of water in this oil as $9x10^{-7}$ and $2x10^{-6}$ cm^2/s at these two temperatures. Duplex-oil films composed solely of MOx, however, dewet within seconds to minutes and are, thus, not long-lasting enough for measuring evaporation rates. Consequently, we follow the suggestion of Holly [38] and use MOx/BSM admixtures to extend duplex-oil-film lifetime.

To obtain the admixture, a small flake of dry BSM is wetted with a known volume of MOx before each experiment. Although it is difficult to control the exact weight of the BSM flake for each experiment, we set the mass of BSM at approximately 10 % of the oil-droplet mass. Compared to films of MOx alone, films spread with BSM are noticeably more viscous, and when spread at the air/water interface retain uniformity and resist motion under a light breeze.

In addition to the MOx/BSM films, we employ films of bovine meibum (BM) in evaporation experiments. Whole bovine eyelids were obtained fresh from a local abattoir, transported in sealed bags to the laboratory, and placed into a water bath at 37 °C. Once warmed, bovine meibum is readily expressed from the glands following Nicolaides *et al.* [57]. Meibum from multiple lids was pooled and sealed in an amber glass jar for storage at -20 °C. Although bovine meibum spreads spontaneously on water above about 35 °C, spreading from a volatile, spreadable solvent results in more uniform films. Therefore, before spreading in all evaporation experiments, bovine meibum was first centrifuged and the supernatant dissolved in a 5:1 (v:v) solution of toluene (108-88-3, >99.8 %, Fisher Scientific, Fair Lawn, NJ) and isopropanol (67-63-0, >99.9 %, EMD Chemicals, Philadelphia, PA). To ensure that solvent, storage process, and pooling play no role, evaporation was also measured through films of fresh, neat bovine meibum. No difference was found.

Human meibum (HM) from healthy human subjects was obtained by expressing the glands and scraping the lid margin with a metal spatula as described by Leiske *et al*. [114] and Rosenfeld *et al*. [83]. Collected material was transferred directly to a glass slide, which was then placed in a sealed amber jar and stored at -20 °C until use. Ethics approval was obtained for collection of human meibum; the procedure followed the guidelines of the Declaration of Helsinki.

The substrate consists of distilled/deionized water with 18.2-MΩ conductivity obtained from a MilliQ^{TM} filtering system (EMD Millipore, Billerica, MA) In some experiments, agarose (Fisher Scientific, Fair Lawn, NJ) and ultrapure water were used to synthesize a 0.5-wt% agarose gel that partially filled the evaporative trough and prevented free convection in the aqueous substrate. Several experiments were performed with various artificial-tear solutions containing salts, proteins, and mucins. Similar to Borchman *et al.* [13], no effect was seen on evaporation rates of pure-water or oil/lipid-covered surfaces.

A large number of chemicals were tested to find a suitable model-oil mixture including wax esters, fatty acids, triglycerides, phospholipids, oil-soluble surfactants, polymers, and oils. High-purity stearyl oleate (17673-49-3,~ 99 %), oleic acid (112-80-1, ~99 %), linseed oil (8001-26-1), dipalmitoyl phosphatidyl choline (DPPC) (63-89-8, >99 %), cholesteryl oleate (303-43-5, >98 %), Brij 30 surfactant (9002-92-0), and cholesterol (57-88-5, >99 %) were purchased from Sigma-Aldrich (St. Louis, MO). Commercial-grade extra virgin olive oil was from Filippo Berio, ITA. Stand oil (Winsor Newton, NJ) was purchased locally. Synthesized polyisobutylene (PIB) with molecular weight 145 kDa (PDI = 1.1) was obtained courtesy of N. Balsara of U.C. Berkeley (Berkeley, CA).

5.2 Apparatus

A schematic of the apparatus for measuring evaporation rates through duplex-oil films is shown in Fig. 5. The system is a miniature Langmuir trough filled with water resting on an analytical balance. Evaporation rates with and without duplex-oil films were obtained gravimetrically by measuring the mass of water remaining in the trough over time.

The custom-built trough was constructed of black Delrin® with a fluid substrate surface area of 20 cm^2 (i.e., 4 x 5 cm) and a depth of 5 mm. Two Teflon® barriers allow compression and expansion of the surface area available to the oil film. The top surface of the trough is rendered hydrophobic using Teflon® coating (86508-42-1, Dupont, Wilmington, DE). Three opposed screws enable leveling of the trough. A flexible heating film (KH-202/5, Omega Engineering Inc., Stamford, CT) adhered to the bottom of the trough provides heat to the water substrate. A thin, K-type thermocouple embedded in the bottom of the trough and coupled to a temperature controller (CN 733, Omega Engineering Inc., Stamford, CT) sets the temperature at the bottom of the water substrate. An infrared thermocouple (OS36-10K-80F, Omega Engineering Inc., Stamford, CT) gauged the average surface temperature of a spot 2 cm in diameter near the center of the water/air or oil/air interfaces.

The water surface is slightly colder in the center of the trough than near the edges, but the infrared thermocouple cannot view the entire gradient. Following others [115, 116], we measure the lateral-surface-temperature distribution using infrared thermography. A Merlin MW-IR thermal camera (FLIR Systems, Wilsonville, OR) images the entire water surface and provides an area-averaged temperature. The offset between the area-averaged surface temperature measured by the thermal camera and the local surface temperature from the infrared thermocouple corrected the infrared-thermocouple measurement. For experiments conducted without heating, the substrate consisted solely of water. When heating through the bottom, however, 4 mm of agarose gel was synthesized in the trough and covered with a 1-mm layer of water. The gel prevented buoyancy-driven thermal convection in the aqueous-substrate layer.

Water-evaporation rates and oil-spreading dynamics were the same with and without the substrate gel present.

The trough rests on an analytical balance (MS 304S, Mettler-Toledo, Columbus, OH) with measurement accuracy of 0.1 mg, much less than the amount of mass lost during a typical experiment. A white light source and color CCD camera (AVT Marlin F131, Allied Vision Technologies, Newburyport, MA) positioned at near-normal incidence to the water surface provided white-light interferometric images of the films. The camera was attached to a PC enabling continuous visualization of the spreading and uniformity of the duplex-oil films. In experiments with 1- to 2-mm thick oil films, a larger surface area was needed to register a mass loss significant enough to gauge reliably the small evaporative flux. In this case, a 10-cm diameter Pyrex® glass crystallizing dish replaced the Langmuir trough.

To obtain repeatable evaporation rates, careful control of the surrounding environment was necessary. Environment temperature (T_∞) and relative humidity (R_H) were maintained at 23-25 °C and 0.32-0.42, respectively, as measured with a Sensirion SHT75 sensor (Zurich, Switzerland). A 5-cm diameter, variable-speed electric fan (Sunon, Kaohsiung City, Taiwan) positioned above the trough directed an impinging jet of air at the interface. Fan rotational speed, ω, was measured using a Strobotac 1531 strobe light (General Radio, Concord, MA). A fan speed of 3800 rpm, corresponding to a nominal velocity of 2.5 m/s (i.e., Reynolds number $Re = 8000$), set a repeatable mass-transfer coefficient without perturbing the film. Nevertheless, impinging airflow from the fan created fluctuations in the mass readings. Evaporation, however, was measured over 15-30 min, a long-enough time period to average fluctuations. A custom program written in LabView continuously recorded measurements from the infrared thermocouple, analytical balance, temperature/humidity sensor, and CCD camera.

5.3 Methods

5.3.1 Spreading experiments

Numerous spreading experiments were conducted to identify oily substances that might mimic the behavior of the tear-film lipid layer (TFLL). Fig. 6 shows representative images of the *in-vivo* human TFLL after a blink in healthy subjects. The color interference patterns indicate lipid-layer thicknesses ranging from 40 to well over 100 nm [78, 117, 118]. Successive frames in Fig. 7 show color interference patterns in the TFLL of a single subject over the course of 6 blinks (approximately 5 s between blinks) [18]. Importantly, the color interferograms in Fig. 7 repeat blink-to-blink with patterns re-emerging but eventually fading after several blinks. Chosen model-oil films must evidence this same phenomenon.

Our goal is to engineer films that spread uniformly at a thickness near 100 nm, that demonstrate repeatable color blink patterns as in Fig. 7, and that resist dewetting long enough to measure evaporation rates. Although the human TFLL need only remain intact several seconds on the eye, we require a more stringent requirement of about 15 min to obtain an evaporation rate. To verify that our *in-vitro* films reflect the required characteristics of the TFLL, we visualized spreading/dewetting behavior of duplex-oil films for a large number of oils and spreaders. In the miniature Langmuir trough, the water surface was set level with the top of the trough sides, and a 0.5-µL droplet of the desired oil was deposited at the air/water interface in the center of the trough using a precision microliter syringe (701, Hamilton Co., Reno, NV). When using human or bovine meibum, the substrate was heated to 35 °C because these lipids spread minimally at ambient temperature. We then document whether or not the oil initially spread and whether or not it remained as a duplex film for at least 1 s. When an observable duplex-oil film occurred, the barrier was closed and opened once to mimic a blink, and the approximate breakup time (BUT) was recorded for visible holes to form in the film. We define BUT as the time taken for the first visible holes to appear in the film.

Fig. 8 records representative behavior of the oils studied. In sequence A-B-C, a duplex film is formed (Panel B) that first forms visible rupture holes after about 5 s post-blink (i.e. BUT). In sequence A-E, the initially spreading drop rapidly dewets into lenses. No duplex-oil film forms. Panel D corresponds to a desposited oil droplet that immediately relaxes into a single lens.

5.3.2 Evaporation rates from a clean-water surface

Clean-surface evaporation experiments yield the evaporation rate J_0, as well as k_m, h, and UA_W at a given airflow rate (see Appendix C), which are properties of the evaporation apparatus. These values are necessary to determine oil-film water permeability via Eq. 16. Pure-water evaporation measurements, therefore, serve to calibrate the apparatus.

Consequently, in each evaporation experiment, we first measured the evaporation rate from a clean-water surface. The unheated trough was filled about 2-3 mm above the brim with distilled/deionized water, the fan turned on, and data acquisition via LabView initiated. In the pure-water experiments, fan speed was varied from 3800 to 6300 rpm to investigate the behavior of the mass-transfer coefficient.

As water evaporates, with or without an oil film present, a steady wet-bulb temperature is reached where the mass of water in the trough decreases linearly in time. Attainment of steady state typically takes 30-40 min. Fig. 9 graphs representative data for the area-averaged surface temperature of a clean-water surface over time at a fan speed of 3800 rpm and no substrate heating. The temperature begins near ambient T_∞, eventually leveling off at the wet-bulb temperature, T_{S0}. For a typical R_H of 28.9 ± 6.9 % and a T_∞ of 23.6 ± 0.7 °C, T_{S0} is 17.2 ± 0.4

°C, which is just slightly higher than the wet-bulb temperature predicted from psychrometric charts of 17 °C [119]. Reported numbers are average ± standard deviation over at least 6 experiments.

After about 15-20 min of steady evaporation at temperature T_{S0}, the water surface falls level with the top edge of the trough. Fig. 10 shows representative results for the mass of water in the trough versus time for fan speeds of 3800, 5000, and 6300 rpm (Re = 8600, 11400, and 14300). Water mass decreases linearly in time indicating a constant evaporation rate. As the fan speed increases from 3800 to 6300 rpm, the mass-transfer coefficient and evaporation rate increase, mass loss is greater, and, thus, the slope of the line is steeper. Similar behavior is seen with a heated substrate. Evaporative mass flux, j_0 [g cm^{-2} s^{-1}], is obtained from the slope of the mass versus time at steady state after dividing by the trough surface area. For the ambient conditions described above and for 3800 rpm, j_0 is 1.16 ± 0.21x10^{-6} g/cm^2/s. Division by the molar mass of water, M, converts j_0 to the molar evaporation rate, J_0, used earlier. We report the measured mass fluxes, but it is implicit that they are converted to molar fluxes when inserted into the equations in §4.

Measurement of T_S, R_H, and T_∞ permits calculation of the water-vapor concentration difference between the air/water interface and the air far from the surface, $\Delta C_0 = C_w^{sat}(T_{S0}) - R_H C_w^{sat}(T_\infty)$. With the concentration driving force known and J_0 measured, we solve Eq. 17 for k_m, which also yields $R_m = 1/k_m$. For typical measured J_0, T_{S0}, R_H, and T_∞, the mass-transfer coefficient in our apparatus is 1.34 ± 0.06 cm/s (average ± std. dev.) at a fan speed of 3800 rpm. For similar ambient conditions and fan speeds of 5000 and 6300 rpm, the respective k_m is 1.63 ± 0.05 and 1.80 ± 0.08 cm/s. From Eq. B.7, h is calculated given the measured k_m value. Finally, we solve Eq. C.5 to establish UA_W that accounts for heat transfer through the edges of the trough due to the small temperature difference between the water-surface center and the trough sides. With the transport properties established, evaporation measurements through the duplex-oil films are interpreted according to Eq. 16 to establish *Dk*.

The experimental process is slightly more involved when the trough is heated from the bottom. Before adding water, warm agarose gel was poured into the trough to a depth of 4 mm and allowed to cool. After depositing a 1-mm layer of water over the gel, the temperature controller was activated at a set-point temperature for the bottom of the substrate, T_b. For a fan speed of 3800 rpm and the ambient conditions listed above, a set-point temperature of T_b = 45°C yields a surface temperature of T_{S0} = 35.4 ± 0.2 °C. The corresponding mass-evaporation rate was j_0 = 4.87 ± 0.27x10^{-5} g/cm^2/s. Calculation of k_m, h, and UA_W remains the same as that for the unheated surface except that we solve Eq. 27 with modification described in Appendix C instead of Eq. C.5.

5.3.3 Evaporation through duplex-oil films

Once the water surface evaporated level with the trough sides, a known volume of oil or solvent solution was deposited at the air/water interface using the precision microliter syringe. The known oil volume, V, and trough surface area, A, set the average film thickness, $L = V/A$. A 2-μL droplet of oil spread uniformly over the 20-cm^2 surface produces a film that is 1-μm thick. Volume of the meibum films was established from the measured mass based on a density of 0.9 g/cm^3. Film thickness was varied from 100 nm to 100 μm, except with bovine meibum, where the maximum film thickness was 10 μm. With bovine-meibum films 1-μm thick or less, meibum was typically dissolved in 50 μL of toluene/ispropanol solution (described earlier) before deposition. For thicker films, 200 μL of the same solvent was used with stepwise deposition to avoid overflow of the nonpolar solvent onto the hydrophobic trough edges or barriers. Although the chosen oils spread spontaneously, thin films less than 1-µm thick rarely cover the entire water surface after initial deposition. To facilitate complete coverage, one barrier was brought across the surface until it almost contacted the other barrier and then returned to its original position, mechanically re-spreading the film. Holly refers to this process as “flexing” the film [38]. We coin this process as “blinking”, as it mimics the action of an eyelid during a blink [120].

Fig. 11 illustrates the water-surface temperature versus time in the unheated trough before and after the deposition of a 2.5-µm MOx/BSM layer at a fan speed of 3800 rpm. After coverage by the uniform duplex-oil film, the water temperature rises from T_{S0} = 18 °C to approach a new steady temperature, T_{SF}, and corresponding new constant evaporation rate, j_F, which depend on the oil-film thickness, among other things. Due to the thinness of duplex-oil films, there is no measurable difference between the two interface temperatures T_{wo} and T_{oa}, so we refer to one measured surface temperature, T_{SF}, that substitutes for T_{wo} in Eqs. 14, 18, and 24 during data analysis. After reaching the film-covered steady-state temperature, mass-loss data are collected for at least another 15 min to ensure a reliable evaporation rate. During this time, the CCD camera records visual images every 5 min. If significant film dewetting occurs, the experiment is discarded.

Fig. 12 shows typical relative evaporative mass loss versus time at a fan speed of 3800 rpm before and after the application of duplex MOx/BSM oil films ranging in thickness from 100 nm to 100 µm. The data are from multiple experiments, so the absolute values of time and mass are shifted for convenience. Filled black squares from t = 0 to t = 47 min show mass loss from the calibrating clean-water surface. Subsequent mass-loss series correspond to water evaporation through films of increasing film thickness. As the film thickness increases, the oil-film diffusion resistance increases and the evaporation rate decreases. Consequently, the slope of mass-versus-time, which gives the evaporative flux of water through the film-covered surface, j_F, decreases. Concurrent measurement of T_{SF}, R_H, and T_∞ allows calculation of the concentration driving force between the water/oil interface and the sub-saturated air: $\Delta C_F = C_w^{sat}(T_{SF}) - R_H C_w^{sat}(T_\infty)$. With j_F measured and ΔC_F established, Eq. 14 is solved for the total mass-transfer resistance, R. Subtraction of the gas-phase mass-transfer resistance, $R_m = 1/k_m$, (calculated from the pure-water evaporation rate as described in §4.2.1) from the total resistance R gives the mass-transfer resistance of the duplex-oil film, $R\text{-}R_m$, via Eq. 16.

In Fig. 13, we plot the measured film mass-transfer resistance ($R\text{-}R_m$) versus film thickness (L) for duplex-oil films of MOx/BSM and bovine meibum (BM). Without substrate heating (■), the average measured surface temperature, T_{SF}, is 20 °C; with heating (□, ○) it is 40 °C. Following Langmuir and Schaefer [8], we fit the film resistance-film thickness data with a straight line. According to Eq. 16, the slope corresponds to the inverse of the water permeability in the oil film, $1/Dk$, and the intercept corresponds to the interfacial resistance, R_I. The intercept is approximately zero for all oil films studied, indicating that R_I is negligible in our systems. Above a 1-μm film thickness, film resistance no longer increases linearly with film thickness. This is likely a consequence of nonuniform film coverage. Inspection of the visual images shows that even with thick films, the water surface is not completely covered near the edges of the trough, leaving 1-5 % of the surface area uncovered. As described in §4.2.3, small exposed areas have minimal effect on evaporation rate at small film thickness, but their impact can be pronounced at large film thickness. Accordingly, we use only the data up to 1-μm thickness in the linear fit to establish Dk.

To determine the water permeability of the oxidized mineral oil without admixed mucin, several experiments with much thicker films were conducted. Films as thick as 1 or 2 mm remained stable without added mucin. Because very little water mass is lost through such a thick oil film, special precautions were necessary. To maximize mass loss, most experiments were conducted in a glass crystallizing dish with a surface area of 79 cm^2. For the thicker films, fluctuations in mass from the applied airflow were no longer negligible, so the fan was not operated. Fortunately, such films are thick enough that the gas-phase mass-transfer resistance, R_m, is insignificant compared to the film resistance, R_F. Additionally, the substrate heater was not used because temperature fluctuations led to significant drift in mass readings from the electronic balance.

Distilled/deionized water was first added to the glass crystallizing dish and evaporated for 1 h to establish steady state, and to allow accurate determination of j_0. Next, an oil film approximately 5 to 8-mm thick was deposited slowly onto the water surface until gravity flattened the oil layer into a uniform bulk film. Then, using the microliter syringe, oil was withdrawn until the film reached the desired thickness (1.5-3 mm). For films of 1-mm thickness, the miniature Langmuir trough was used with only a 3-mm layer of water as the substrate, and the oil film was deposited directly onto the surface without overfill and siphoning of the oil. Once the oil film was in place, water was evaporated for up to 48 h to register significant mass losses. In one experiment, 5 wt% BSM was added to the film to ascertain the effect of mucin on the water permeability of the thick oil films.

5.3.4 Water uptake into oil

The partition coefficient, *k*, reflects the equilibrium uptake of water by the oil. To gauge *k* for our duplex-oil films, oil samples were equilibrated in dry and humid vapor environments.

Resulting water uptake was measured by oil-sample mass change and by differential scanning calorimetry (DSC). Three 10-mg samples of oxidized mineral oil, consisting of 10 wt% BSM, and bovine meibum were placed in aluminum TA Tzero sample pans (TA Instruments, New Castle, DE) and weighed with an analytical balance. The open sample-containing pans were equilibrated for 48 h in a sealed glass container containing either pure water or anhydrous calcium-sulfate desiccant (Drierite, W.A. Hammond Drierite Co., Xenia, OH). The relative humidity in the sealed glass container was measured to be <5 % when containing desiccant and >90 % when containing pure water.

After removal from the glass chamber, each sample mass was recorded, and the pans were hermetically sealed with an aluminum lid. Each pan was placed into the DSC (TA Instruments DSC Q20, New Castle, DE), and cycled between 30 and -30 °C at a rate of 5 °C/min. From the measured heat released upon freezing/melting of any water present and the known heat of fusion, we establish the mass of water present in each sample.

6. Results

6.1 Film spreading and stability

To establish a model duplex-oil film that mimics evaporation through the human TFLL, we investigated the spreading and stability of a large number of oils in the miniature trough. Table 1 reports spreading behavior for 17 oil mixtures of 0.5-µL volume spread on the 20-cm^2 air/water interface. As illustrated in Fig. 8, we recorded whether the various oils spread initially, whether the spreading film remained long enough to form a duplex-oil film, and how long the duplex film remained, as gauged by approximate BUT, after blinking action of the trough barriers. Tested substances fall into the categories of pure components, oil-soluble surfactant dissolved in mineral oil, meibomian-lipid mimics, and other mixtures including the MOx/BSM admixture. As expected, mineral oil, whose initial spreading coefficient is negative, does not spread. Pure surface-active lipids below their pK_a value, including oleic acid, stearyl oleate, and cholesteryl oleate, all spread initially. However, these lipid mimics subsequently dewet rapidly, and no metastable duplex film is observed. Olive oil and linseed oil, which are mixtures of plant-based lipids, spread initially but remain as duplex-oil films for only 1 s.

Mixtures of mineral oil and other surface-active substances exhibited varying results. Films spread from mineral oil mixed with 0.5-wt% oleic acid; 0.4-wt% cholesteryl oleate/0.4-wt% cholesterol; or 2-wt% stand oil persisted long enough to exhibit duplex-oil films (>1 s). Addition of DPPC to mineral oil in percentages above 0.5 wt% enabled initial spreading, but observable duplex-oil films did not form. Identical results emerged for mixtures of Brij 30 and mineral oil; cholesteryl oleate/stearly oleate/DPPC/ mineral oil; and cholesterol/cholesteryl oleate/stearyl oleate.

In agreement with others [8, 37, 38], oxidized mineral oil (MOx) spread at the air/water interface and remained uniform for approximately 5 s after blinking the trough barriers. Addition of PIB to the MOx increased the viscosity to 80 mPa·s and, thus, increased BUT to 10 s.

The most stable model duplex-oil film resulted from the MOx/BSM admixture. In this system, the initial spreading rate is much slower than those with the other mixtures because the BSM flakes disaggregate and dissolve into the oil and water. Once spreading is complete and the barriers are blinked, the 250-nm film resists dewetting for about 5 min. Thicker films resisted dewetting for much longer.

Fig. 14 shows interference patterns visible under white light in spread MOx/BSM films after successive blinking of the trough barriers every 5 s. Color interference patterns repeat over several blinks, similar to the human-eye images in Fig. 7 showing repeated blink patterns in the *in-vivo* human TFLL. Duplex-oil films of MOx alone also display repeated blink patterns. However, these films do not resist dewetting long enough to permit evaporation-rate measurements.

The most stable duplex films at the air/water interface were spread from samples of bovine (BM) and human meibum (HM). Both human and bovine meibum are waxy solids at room temperature [83]. Minor spreading occurred at 23 °C. Upon heating the water/air interface to 35 °C, both human and bovine meibum spread spontaneously. Upon blinking the films in the Langmuir trough, these films remained stable for well over 30-45 min without visible dewetting. Color interference patterns for bovine and human-meibum films (not shown) are similar both to those seen *in vivo* and those from MOx/BSM films. Our spreading studies focus on model MOx/BSM and meibum as candidate duplex-oil films for the evaporation experiments.

6.2 Evaporation reduction

6.2.1 Unheated substrate

A battery of 40 repeat experiments first measuring J_0 and T_{S0} followed by J_F and T_{SF} as a function of film thickness were conducted with MOx/BSM duplex films without substrate heating. Film thicknesses ranged from 100 nm to 100 µm. Experimental conditions and apparatus transport properties measured from the pure-water results are listed in Table 2. For the film-covered water surfaces, Dk was determined from the slope of film resistance, R-R_m, versus film thickness, L, as described in §5.3.3 and illustrated in Fig. 13. Results are shown in the first row of Table 3 (i.e., $Dk = 1.1 \times 10^{-4}$ cm^2/s).

Once Dk is known, Eqs. 18 and 24 permit simultaneous calculation of the evaporation ratio J_F/J_0 and surface temperature T_{SF} as a function of film thickness with no adjustable parameters. Comparison to the experimental data is made as solid lines in Fig. 15 and Fig. 16, respectively. Theory and data are in good agreement with minor discrepancy for the thickest films, which deviate from linearity in Fig. 13. As expected, increasing film thickness slows evaporation, causing the surface temperature to rise. Quantitative prediction, however, demands the proposed dissolution-diffusion theory.

Two evaporation experiments were conducted with bovine meibum without substrate heating. At ambient temperature, bovine-meibum films do not readily spread; obtaining uniform film coverage was difficult even with the spreading solvent since bulk bovine meibum is a viscous, solid-like wax [83]. Due to the difficulty in obtaining uniform films, one film each was deposited at 100 and 500 nm. Evaporation reduction by bovine-meibum duplex films of 100 and 500-nm thickness was 36 and 81 %, respectively.

6.2.2 Heated substrate

Water evaporation through duplex films of MOx/BSM, bovine meibum (BM), and human meibum (HM) was likewise measured with a warmed substrate to facilitate meibum spreading and to reflect eye conditions. As with the unheated substrate, measurements of J_0 specified the apparatus transport properties reported in Table 2, and measurements of J_F and T_{SF} as functions of film thickness allowed determination of Dk from the slope of $R\text{-}R_m$ versus L as reported in Table 3. Theory then predicts J_F/J_0 and T_{SF} as functions of L.

Comparison to experimental evaporation-reduction and surface-temperature data (T_b = 45 °C) at 3800-rpm fan speed is made in Figs. 17 and 18. In these figures, filled squares correspond to MOx/BSM films and open circles correspond to BM films. Additionally, two samples of human meibum (HM) were obtained and tested, indicated in Fig. 17 by inverted open triangles. The two lines in each figure correspond to the predictions of coupled Eqs. 18 and 24 with the corresponding *Dk* for each oil from Table 3: solid lines for MOx/BSM and dotted lines for BM. Ascertained permeabilities measured by *R*-versus-*L* data are 1.6 and 2.6x10^{-4} cm^2/s for MOx/BSM and BM duplex films, respectively, at an average T_{SF} = 40 °C. The limited sample amount of bovine meibum restricted the thickest bovine-meibum film studied to 10 μm and less. Excellent agreement is found between dissolution-diffusion theory and experiment, especially since no adjustable parameters are used in the theoretical predictions.

6.3 Evaporation through thick oil films

For oxidized-mineral-oil films between 1- and 5-mm thick deposited over water in a glass crystallizing dish, the measured water permeability, *Dk*, ranged from 2-3x10^{-5} cm^2/s, almost and order of magnitude smaller than that for MOx/BSM. For 2-mm thick films of MOx deposited in the miniature Langmuir trough, the calculated *Dk* ranged from 2.6-3.5x10^{-5} cm^2/s. In one experiment, a 1.9-mm thick layer of oxidized mineral oil was deposited in the miniature Langmuir trough: the calculated *Dk* was 3.2x10^{-5} cm^2/s. In another experiment, the same thickness film was deposited in the trough and 191 g of BSM were gently contacted with the film. The BSM quickly settled into the film, and evaporation was measured over the course of 24 h. The calculated *Dk* was 5.6x10^{-4} cm^2/s. At the end of the experiment, large domains of water-containing BSM were visible throughout the oil film. Regions rich in BSM contained water droplets that appeared to rise through the oil film. Apparently, admixed water-liking mucin molecules imbibe water into the duplex-oil films.

6.4 Water uptake into oil

DSC measurements showed no measurable amount of water uptake into the samples of oxidized mineral oil. However, the samples of MOx/BSM and bovine meibum exhibited freezing and melting peaks corresponding to water phase transitions [83]. Integration of the heat-flow peaks show that MOx/BSM and bovine meibum contain up to 10 and 4 wt% water, respectively, when equilibrated with water vapor at >90 % relative humidity. Detailed information on the DSC experiments is reported by Rosenfeld *et al*. [83].

7. Discussion

Not surprisingly, most oils deposited on water do not form persistent duplex films over a timescale useful for evaporation experiments. Three substances did so: MOx/BSM, human meibum, and bovine meibum. Similar to the results of Heymann and coworkers [5, 47], we find that addition of an interfacial structurant, BSM, imparts stability to duplex films of oxidized mineral oil. Although films of oxidized mineral oil alone form uniform duplex films, the resulting films are relatively fluid as seen by swirling and movement of the interference patterns. These films dewet well before the 15 min necessary to measure evaporative mass loss. In contrast, incorporation of BSM into mineral oil results in films that show little or no motion at the interface. Apparently, mucin forms gel-like networks at the water/oil and/or water/air interfaces.

Duplex-oil films spread from both human and bovine meibum were similarly stable at physiologic temperature. Viscosity of both human and bovine meibum is four orders of magnitude larger than that of water at 35 °C [83]. Large viscosity slows the dewetting process. Some films of meibum spread from samples stored for many months did indeed dewet in a fashion similar to mineral-oil mixtures. It is possible that decomposition of the meibomian lipids leads to a less-structured material that does not remain stable. There is evidence that the human TFLL indeed dewets *in vivo* [82].

The duplex-oil films tested well obey the dissolution-diffusion mechanism of evaporation reduction outlined in §4.2, as shown by Fig. 13 and Figs. 15-18. The linear relationship between film resistance and film thickness, illustrated in Fig. 13, confirms a constant *Dk*. In agreement with Langmuir and Schaefer [8], we do not find interfacial resistance in any of our duplex-oil films. Interfacial resistance apparently demands polymerized spreaders [47]. Figs. 15-18 show the measured evaporation ratios and surface temperatures in comparison with dissolution-diffusion theory. Close agreement between data and theory in all of figures indicates that heat and mass transfer in the films is well characterized by our proposed 1-D model. Importantly, the fitted *Dk* value for each duplex-oil-film substance listed in Table 3 is a material property that describes water transport through the film. Without obtaining *Dk* from the raw evaporation data, quantitative comparison of evaporation reduction between different experimenters is not possible because measurements are apparatus and procedure sensitive.

Model and experiment do not agree as closely for the thickest films, which we attribute to inhomogeneous film coverage. The disagreement is most readily seen in Fig. 13, where film resistance no longer increases linearly with film thickness above 1 µm. Gilby and Heymann [47] report a similar trend. They attribute this behavior to “an inhomogeneity of the duplex films below 10-µm thickness.” Films at smaller thicknesses tend to dewet more readily, resulting in inhomogeneous coverage. However, theory outlined in §4.2.3 predicts that the effect of dewetted holes on evaporation reduction decreases as the duplex-film thickness decreases. In fact, the effect of holes on evaporation is magnified in thicker films.

Duplex-oil-film water permeabilities calculated in §5.3.3 and shown in Table 3 for each film chemistry are higher than expected for an aliphatic hydrocarbon oil. Permeability is the product of the water diffusivity, *D*, and the partition coefficient, *k*, in the oil. Reported partition coefficients vary from about 3 for pure hexadecane or mineral oils [121] to 50 for vegetable oils [122]. Water diffusivities predicted in §5.1 for MOx give an expected permeability range of 0.3-5x10^{-5} cm^2/s at 20 °C and 0.6-10x10^{-5} cm^2/s at 40 °C. Experiments of Schatzberg [123] with pure hexadecane demonstrate water permeabilities of 7.3 and 8.5x10^{-5} cm^2/s at 20 and 40°C. Langmuir and Schaefer fitted their data to a water permeability of 2.1x10^{-5} cm^2/s for oxidized turbine oils [8]. Our values obtained for MOx/BSM and BM duplex films in Table 3 are significantly larger.

MOx/BSM films contain approximately 10 wt% bovine submaxillary mucin (BSM), a strongly water-liking glycoprotein. BSM molecules consist of hydrophilic carbohydrate moieties extending from a polypeptide backbone [124, 125]. From the water-uptake experiments in §6.4, we find no measurable amounts of water present in pure oxidized mineral oil. However, the mucin-containing oxidized mineral oil contains as much as 10 wt% water. To confirm that the added mucin is indeed the cause of increased evaporation rate, we tested thicker MOx films above L_c that did not require mucin to remain stable. For 1.5 and 2-mm thick films of nascent oxidized mineral oil, the measured water permeability was 3x10^{-5} cm^2/s, close to that obtained by Langmuir and Schaefer for films of oxidized turbine oil [8]. When 5 wt% mucin was added to the same films, the permeability increased tenfold, and water visibly incorporated into the films. We conclude that admixed mucin increases the water permeability of MOx/BSM duplex-oil films.

High water permeability of bovine-meibum duplex films is more difficult to rationalize because no literature exists on the transport or water-uptake properties of bovine meibum. Only recently have data emerged on the structural and rheological properties of human and bovine meibum [83, 114, 126]. Bovine meibum is orders of magnitude more viscous than mineral oil [83] and is composed largely of waxy and cholesterol esters along with other lipids generally more polar than the hydrocarbons that constitute mineral oil [57]. Compared to oxidized mineral oil, the viscosity and polarity of bovine meibum are higher, leading to a lower D and a higher k. Bovine and human meibum are not amorphous fluids. Recent work shows that these substances are composed of structured lipid crystallites suspended within an amorphous continuous phase [83, 114]. It is possible that the continuous phase, through which water diffuses, consists of a non-crystallized lipid not much more viscous than is mineral oil. Thus, the expected diffusion coefficient corresponds not to an oil of 10^4 mPa·s viscosity, but considerably lower. The absence of measured continuous-phase properties makes prediction of D in meibum difficult. DSC results presented here indicate that bovine meibum imbibes up to 4 wt% water, which suggests a high k of water in bovine meibum, but not as high as that of MOx/BSM. To explain fully the water permeability of meibum, more work is needed to understand its physicochemical structure.

In Fig. 19, we compare our J_F/J_0 measurements at physiologic-temperature for MOx/BSM, BM, and HM duplex films versus film thickness to data available in the literature. In the case of Langmuir and Schaefer [8], we used our 1-D dissolution-diffusion model to predict J_F/J_0 based on their reported Dk values and our measured heat and mass-transfer coefficients. This exercise permits comparison between the two data sets. For the data of Gilby and Heymann

[47], we chose those experiments with an estimated mass-transfer coefficient closest to ours. For the remaining literature data, we plot the values of J_F/J_0 reported by the authors.

Unlike previous work with meibum and tear-lipid mimics [13, 14, 33], our duplex-oil films reduce evaporation significantly as the film thickness increases, consonant with the dissolution-diffusion mechanism. The ability to spread and maintain uniform duplex-oil films explains our observation of significant evaporation reduction, whereas others do not [13, 14]. Nevertheless, bovine-meibum duplex films at physiological thickness, i.e., 100 nm, reduced water evaporation only by 6 %, which is much less than normally attributed to the human TFLL [21, 32]. Human-meibum duplex films in this study also reduced evaporation by only 8 % at 100-nm thickness.

In contrast to our *in-vitro* results, Mishima and Maurice report *in-vivo* evaporation reduction of 93 % by rabbit-meibum lipid films [21]. Unfortunately, the corresponding *in-vivo* measurement of evaporation reduction by the human TFLL is not available since most experiments can only detect j_F and not j_0. The range of clinically measured tear-evaporation rates from healthy subjects under various flow and environmental conditions is $0.002\text{-}6.3\text{x}10^{-6}$ g/cm^2/s. Most *in-vivo* tear-evaporation rates are measured without forced flow. The average evaporation rate measured under many different flow conditions is $j_F = 1.25\text{x}10^{-6}$ g/cm^2/s at $T_S \approx$ 35 °C [127], $R_H \approx$ 30-40 %, and $T_\infty \approx$ 23-25 °C, similar environmental conditions to those in this study. Tomlinson *et al.* [70] measured the evaporation rate from pure water at 31 °C with the same device as used on eye. Comparison between the two measurements suggests an *in-vivo* evaporation reduction by the human TFLL of 25-45 %, much less than that of the rabbit. However, because j_F and j_0 are not measured under identical conditions, this estimate is not quantitative. Although the clinical evaporation rate is about 2-3 % of our *in-vitro* measurents, j_0

remains unknown for most clinical measurements, precluding direct calculation of the lipid-film mass-transfer resistance, R_F, or even evaporation reduction. Thus, it is possible that clinically reported evaporation reduction results primarily from a gas-phase mass-transfer resistance and not from the TFLL resistance.

To accentuate this point, quantitative analysis of evaporation rates requires an estimate of k_m, which depends on airflow and apparatus geometry. With a few exceptions, clinically measured evaporation rates are conducted in the absence of forced airflow. Tomlinson *et al.* discuss the details of the evaporation-rate measurement methods [70]. Briefly, evaporation rates without forced flow are obtained either by measuring the relative-humidity gradient in front of the eye using a modified dermatological evaporimeter [71] or by measuring the transient relative-humidity increase in a sealed goggle placed over the eye [63, 72]. We estimate a reasonable range of k_m for these experiments as 0.05-1 cm/s. Due to the thinness of the human tear film, we assume that the tear-surface temperature remains constant regardless of the presence of a lipid film, so $T_{SF} = T_{S0}$. The clean-water evaporation rate for the *in-vivo* experiments then ranges from $1.6\text{x}10^{-6}$ to $3.1\text{x}10^{-5}$ g/cm^2/s at T_∞ = 23 °C and R_H = 40 %. Therefore, depending on the mass-transfer coefficient, the average clinically measured evaporation reduction varies from 20-96 %. Assuming a lipid-layer thickness of 100 nm, Eqs. 14 and 15 specify the possible range in lipid-layer water permeability for various values of the mass-transfer coefficient. Thus, for k_m = 1 cm/s, Dk = $4.2\text{x}10^{-7}$ cm^2/s; for k_m = 0.05 cm/s, Dk = $2.0\text{x}10^{-6}$ cm^2/s. At very small mass-transfer coefficient, however, estimation of Dk is extremely sensitive to changes in k_m. If k_m = 0.04 cm/s, the calculated Dk is $3.0\text{x}10^{-4}$ cm^2/s, close to that of this study: $2.6\text{x}10^{-4}$ cm^2/s. Importantly, without careful characterization of mass-transfer rates in clinical-evaporation measurements, it is not possible to estimate the effect of the TFLL on evaporation reduction.

Airflow and water permeability of the lipid layer control the evaporation rate through the TFLL. Fig. 20 shows the calculated mass evaporation rate through a duplex film, j_F, as a function of film thickness, L, for various impinging air speeds, u, and two lipid-layer water permeabilities, Dk. We set $T_{S0} = T_{SF} = 35$ °C, $R_H = 40$ %, and $T_\infty = 23$ °C to replicate physiological conditions. Solid, dotted, and dashed lines show theory results for $u = 0.01$, 0.1, and 1 m/s, representative of air speeds for nearly stagnant air, flow in a ventilated room, and walking, respectively [128]. The mass-transfer coefficient at each velocity is calculated by ratio with that measured in our experiments, assuming $k_m \sim u^{0.54}$ [107, 129]. Lines labeled with open squares and open circles correspond to $Dk = 2.6\text{x}10^{-4}$ and $2.6\text{x}10^{-6}$ cm^2/s, respectively. Lower water permeability and slower air speed lead to lower evaporation rates. The ordinate intercept of each line corresponds to j_0, which increases significantly with increasing air speed. Greater evaporation reduction at any film thickness is effected by a smaller Dk for a given air speed or by a larger air speed for a given Dk. There is no single evaporation rate or evaporation reduction. Thus, reporting a single number for the evaporation rate of the human TFLL is misleading. In addition to environmental R_H and T, evaporation rate and evaporation reduction depend strongly on airflow as well as on the thickness and water permeability of the lipid layer. At 100-nm thickness, little evaporation reduction is predicted except at the lowest Dk and the highest air speed. The importance of both controlling the experimental conditions and measuring k_m (i.e., j_0) cannot be understated.

If we assume that $k_m > 0.05$ cm/s, then clinical evaporation measurements suggest that the water permeability of the human TFLL is ~10^{-6}-10^{-7} cm^2/s, which is at least an order of magnitude smaller than the most impermeable duplex-oil films measured by Langmuir and Schaefer [8], and two to three orders of magnitude lower than the *in-vitro* measurements from this study. We offer several reasons for this discrepancy.

First, recent measurements of meibum physical and structural properties show that human and bovine meibum undergo solidification phase transitions below 35 °C, turning into solid wax-like solids [83]. Eye temperature is close to this transition temperature, but all of our evaporations experiments were deliberately conducted well above this transition to avoid possible drastic changes in meibum properties at different film thicknesses and temperatures. Two evaporation measurements conducted with bovine meibum at 20 °C gave *Dk* ~ 1×10^{-5} cm^2/s, which is about an order of magnitude less than that at 40 °C. Nevertheless, the calculated *Dk* of bovine meibum at well below tear-film temperature is still much higher than that necessary to explain the purported clinical measurements [21, 32, 71].

Second, it is possible that our *in-vitro* substrate and duplex-oil films are fundamentally different than the *in-vivo* aqueous tear film and TFLL. The presence of salt, proteins, and mucins in the aqueous tear film is lacking in the most of our experiments. As mentioned in §5.1, however, addition of these components did not affect evaporation rates from either clean or film-covered water surfaces. This agrees with Borchman *et al.* [13] and Herok *et al.* [14] who show that human tear and salt buffers containing proteins evaporate at the same rate as pure water alone. The colligative effect of salt on the water-vapor pressure is minimal because tear salts make up less than 1 percent of the aqueous phase [24, 30, 130]. Lowering of the water chemical potential by dissolved protein is likewise negligible. Specific interaction between proteins and lipids adsorbed at the aqueous/lipid interface might lead to a structural change in the interface and lead to an interfacial resistance, R_I. However, we have no experimental evidence for such behavior.

Another possibility is that our sampling for bovine and human meibum results in exuded lipids with different chemical and physical properties than those in natural secretion. The physical state of meibum expressed from human meibomian glands depends on the pressure applied to the eyelid during collection [131]. At light pressures, typically less than 1 psia, liquid material exits the meibomian glands, but at higher pressures, the expressed material becomes solid-like. The bovine meibum collected from excised lids was done so at high pressures; human-meibum collection was not controlled for pressure application other than to avoid discomfort to the patients. Thus, it is possible that we obtained meibum not representative of that secreted under natural *in-vivo* conditions. We note, however, that the increased viscosity of solidified meibum usually exuded at high pressures likely exhibits lower *Dk* than liquid meibum deemed to be natural. Gentle expression of the glands results in a less viscous and larger water-permeable meibum that exhibits even less resistance to evaporation.

In our view, none of these potential explanations explains the apparent difference between the *in-vitro* evaporation rates in this study and clinical results on humans and rabbits. It remains an open question whether the human TFLL contributes significantly to water-evaporation reduction in the human tear film [132].

8. Conclusions

We review the available literature on water-evaporation reduction by duplex-oil films and outline the theoretical underpinnings of spreading and evaporation kinetics that govern behavior of these systems. The dissolution-diffusion model unifies data reported in the literature and identifies dewetting of duplex films into nonuniform layers as a key challenge to obtaining significant evaporation reduction. We develop an improved apparatus for measuring evaporation reduction by duplex-oil films. New data reported in this study fit into the larger body of work conducted on water-evaporation by duplex-oil films. Duplex-oil films of MOx/BSM and bovine meibum reduce water evaporation by a dissolution-diffusion mechanism, as confirmed by agreement between the new measurements and theory. The water permeability of MOx/BSM duplex films agrees with those reported in the literature [8, 45, 123], after correction for the presence of bovine submaxillary mucin.

We find that duplex-oil films of bovine and human meibum at physiologic temperature reduce water evaporation only 6-8 % for a 100-nm film thickness pertinent to the human tear film. These numbers disagree with the 75-93 % reduction reported by *in-vivo* clinical measurements on evaporation reduction by rabbit lipid layers [21, 32]. Comparison to *in-vivo* human tear-evaporation measurements is inconclusive because evaporation from a clean-water surface is not measured and, accordingly, the mass-transfer resistance is not characterized. Without this characterization, evaporative resistances of the air and lipid layer cannot be decoupled. Theoretical estimation of j_0 gives evaporation reduction by the *in-vivo* human lipid layer of 20-96 %. Even at the smallest reduction, the calculated duplex-oil-film water permeability of the TFLL is significantly less than that reported in this study. To reconcile this difference, future *in-vivo* evaporation measurements must include calibration to characterize the mass-transfer coefficient and measurement of the evaporation rate from a clean-water surface.

Acknowledgments

This work was partially funded by Alcon Corporation under Contract 022466-003 to the University of California. The authors thank Yuzhang Li and Kevin Okimura for calibrating the

IR camera and IR thermocouple, Gerald Fuller for use of the infrared camera, Nitash Balsara for the PIB samples, Rachel Segalman for use of the DSC, Eric Granlund for machining the miniature Langmuir trough, and David Chang for conducting many of the spreading experiments.

Appendix A. Thermodynamic stability of duplex films

Eq. 3 in §3.2 describes the free energy of hole formation in a thin duplex-oil film. Changes in surface energy and gravitational-potential energy are included in the analysis. Details are given here on the derivation of the gravity term ($\frac{1}{2}\tilde{\rho} g A_H L_0^2$) and on the calculation of areas A_1 and A_2.

The gravitational term in Eq. 3 results from the difference in gravitational-potential energy between a hole-containing film (Fig. 2B) and that with a uniform film (Fig. 2A). The gravitational-potential energy, *PE*, is that of the water substrate plus the oil film. The average potential energy in Fig. 2A containing a uniform film of thickness L_0 resting on a substrate of thickness *d* is

$$\overline{PE}_{film} = m_w g \bar{z}_w + m_{oil} g \bar{z}_{oil} = \frac{1}{2}\rho_w A_0 g d^2 + \rho_{oil} A_0 g\left(L_0 d + \frac{L_0^2}{2}\right) \tag{A.1}$$

where subscripts *w* and *oil* indicate the water and oil phases, respectively, m_i is the mass of material in phase *i*, *g* is the gravitational constant (9.81 m/s^2), $\bar{z}_i$ is the average height of phase *i* above the reference point at the bottom of the trough, ρ_i is the mass density of phase *i*, and A_0 is the area of the water/oil and oil/air interfaces.

After dewetting and hole formation, the oil phase covers a smaller area, $A = A_0 - A_H$. Assuming that $r\text{-}r_1$ and $r\text{-}r_2$ are much smaller than the radius of the overall film, mass conservation of oil yields $A_0L_0 = AL$, and the resulting dewetted oil film thickens slightly. Buoyancy requires that the air/water interface in the hole rise a distance l' above the height of the water/oil interface in Fig. 2A. When a hole forms in the film, the average potential energy in Fig. 2B is:

$$\overline{PE}_{hole} = \frac{1}{2}\rho_w A_0 g\left(d - l_2 + l'\right) + \rho_w A_H l_2 g\left(d - \tfrac{1}{2}l_2 + l'\right) + \rho_{oil} AL\left(d - l_2 + l' + \tfrac{1}{2}L\right) \qquad \text{(A.2)}$$

where all terms are defined in §3.2. Hydrostatics dictate that $l_2 = L\,\rho_{oil}/\rho_w$. Conservation of water mass relates l' and l_2:

$$l' = l_2\left(1 - \frac{A_H}{A}\right) \qquad \text{(A.3)}$$

Upon combining Eqs. A.1-A.3 and the mass-conservation expressions for water and oil, the change in average gravitation potential energy between the film-with-hole and uniform-film states is

$$\Delta\overline{PE} = \overline{PE}_{hole} - \overline{PE}_{film} = \tfrac{1}{2}\rho_{oil} g A_0 \left\{\left(1 - \frac{A_H}{A}\right)\left[\frac{\rho_{oil}}{\rho_w}L^2\left(1 - \frac{A_H}{A}\right) + 2Ld\right] - \right.$$

$$\left. - \left(1 - \frac{A_H}{A_0}\right)\left[\frac{\rho_{oil}}{\rho_w}L^2 + 2Ld + L^2 + L^2\left(1 - \frac{A_H}{A_0}\right)\right]\right\} \qquad \text{(A.4)}$$

In practice, the hole area is much smaller than the initial area such that $A \sim A_0$, and Eq. A.4 simplifies to

$$\Delta\overline{PE} = \frac{1}{2}\rho_{oil}\left(1 - \frac{\rho_{oil}}{\rho_w}\right) g L^2 A_H \left(1 - \frac{A_H}{A_0}\right) \qquad \text{(A.5)}$$

By assuming $L \sim L_0$, $A_H << A_0$, and by defining $\tilde{\rho} = \rho_{oil}\left(1 - \rho_{oil}/\rho_w\right)$, Eq. A.5 simplifies to the gravitational term in Eq. 3 of the text:

$$\Delta\overline{PE} = \frac{1}{2}\tilde{\rho} g A_H L_0^2 \qquad \text{(A.6)}$$

The water/oil and oil/air interface shapes in the region surrounding the hole determine r_1, r_2, A_1, and A_2. We follow Sharma and Ruckenstein [93] and solve the Young-Laplace equation ignoring gravity for the shape of both interfaces and obtain expressions for the oil/air and oil/water profiles, $r_i(z)$. Evaluation of the profiles at l_1 and l_2 gives r_1 and r_2, respectively:

$$r_i = r_0\left[\cosh\left(\frac{l_i}{r_0\sin\alpha_i}\right) + \cos\alpha_i \sinh\left(\frac{l_i}{r_0\sin\alpha_i}\right)\right] \qquad i = 1,2 \tag{A.7}$$

where the subscript i = 1 or 2 for the top or bottom surface, respectively, and α_i is the contact angle in the oil between the water/air horizontal and the oil/water or oil/air interfaces. Neumann's triangle relates the three tensions, γ_w , γ_o, and γ_{ow}, to each contact angle. Areas are calculated by integrating the arc length from r_0 to r_1 or r_2. The result is

$$A_i = \frac{\pi}{2} r_0^2\left[(1+\cos^2\alpha_i)\sinh\left(\frac{l_i}{r_0\sin\alpha_i}\right) + 2\cos\alpha_i(\cosh\left(\frac{l_i}{r_0\sin\alpha_i}\right) - 1) + \frac{2l_i}{r_0}\sin\alpha_i\right] \quad i = 1,2 \tag{A.8}$$

where again the subscript i denotes the areas of the top (1) or bottom (2) "shoulder" areas. Following Sharma and Ruckenstein [93], we assume that the profiles level at l_i for $r > r_i$, but since we ignore gravity in solving the Young-Laplace equation, the calculated profiles do not level smoothly.

Substitution of the expressions for r_i and A_i into Eq. 3 and evaluation at $\Delta F=0$ gives the critical film thickness L_c, which depends on γ_o, γ_{ow}, α_1, α_2, and r_0. We numerically evaluate L_c. Similar to Eq. 13 of Sharma and Ruckenstein [93], L_c is linear with r_0. For a reasonable range of mass densities and tensions applicable here, $f = L_c/r_0$ varies from ~0.2-0.8, corresponding to a total contact angle, $\alpha_1 + \alpha_2$, of 20 to 90°.

Appendix B. Impinging-jet heat and mass transfer

The air-supply fan shown in Fig. 5 directs an impinging jet of air perpendicular to the evaporating water surface in the miniature Langmuir trough. The resulting stagnation flow [133] at the water surface convects water vapor from the surface and heat to or from the surface, depending on whether the trough is heated. Eqs. 13 and 21 describe how water flux and heat flux from the trough into the air depend on the mass- and heat-transfer coefficients, k_m and h. As mentioned previously, k_m and h vary with the type and magnitude of the airflow as well as with the apparatus geometry. This dependence is reported in terms of the relationship between the Sherwood (*Sh*) and Nusselt (*Nu*) numbers, which characterize k_m and h, and the Reynolds (*Re*) number, which characterizes the airflow. For impinging-jet flow these dimensionless groups are

$$Sh = \frac{k_m D_{fan}}{D_{wa}} \tag{B.1}$$

$$Nu = \frac{h D_{fan}}{k_a} \tag{B.2}$$

$$Re = \frac{V_{fan} D_{fan}}{\nu}$$

(B.3)

where D_{fan} is the fan diameter, D_{wa} is the mass diffusivity [m^2/s] of water vapor in air, k_a is the thermal conductivity of air [W/m/K], V_{fan} is velocity of air exiting the fan [m/s], and ν is the momentum diffusivity of air [m^2/s]. V_{fan} is provided by the manufacturer via a linear calibration with fan rotational speed, ω. Correlations for *Sh* and *Nu* at solid surfaces exposed to impinging-jet fluid flow are tabulated [107, 129]. Obot and Trabold [134] reported good agreement between the correlation proposed by Martin [107] and their measured values for water-evaporation data. For a single fan of diameter D_{fan} placed at a distance H_{fan} above a surface, the integral-mean *Sh* and *Nu* at a radial distance *r* along on the evaporating surface from the stagnation point follow the forms

$$\frac{\overline{Sh}}{Sc^{0.42}} = \frac{\overline{Nu}}{Pr^{0.42}} = F\left(Re, r/D_{fan}\right)G\left(H_{fan}/D_{fan}, r/D_{fan}\right) \tag{B.4}$$

where $\overline{Sh}$ and $\overline{Nu}$ are the integral-mean of *Sh* and *Nu* from radius $r = 0$ to *r* and *F* and *G* are functions shown graphically in Fig. 9 of Martin [107]. Schmidt (*Sc*) and Prandtl (*Pr*) numbers are

$$Sc = \frac{\nu}{D_{wa}} \tag{B.5}$$

$$Pr = \frac{\nu}{\alpha} \tag{B.6}$$

where α is the thermal diffusivity of air [m^2/s]. For air at 25 °C, $Sc = 0.6$ and $Pr = 0.7$. Fig. 9 in Martin [107] plots $\overline{Sh}/Sc^{0.42}$ and $\overline{Nu}/Pr^{0.42}$ versus *Re* for $H_{fan}/D_{fan} = 7.5$ and various r/D_{fan}. For our experimental apparatus, $H_{fan}/D_{fan} = 8$ and $r/D_{fan} = 0.5$. The correlation in Martin [107] predicts that $\overline{Sh}$, $\overline{Nu} \sim Re^{0.54}$.

In our experiments, k_m is established from pure-water evaporation experiments using Eq. 17. The rotational fan speed, ω, measured with a strobe light, sets the air exit velocity from the fan, V_{fan}, permitting calculation of *Re.* Fig. B1 shows measured log k_m versus log ω at two average surface temperatures: $T_{S0} = 17.2$ and 34.7 °C. There is little difference between k_m at the two temperatures, which is expected because the change in air physical properties is negligible over this range. Least-squares fitting calculates the slope of both lines to be 0.58, which is close to that reported in Martin [107] for similar systems. Mass and heat transfer in our system are, therefore, well described by impinging-jet flow. Any difference is most likely due to differences in fluid flow and geometry between our system and those reported in literature, such as the presence of trough barriers that alter the airflow compared to that for a flat plate.

From the experimentally measured values of k_m, we calculate h using Eq. B.4

$$h = k_m\left(\frac{k_a}{D_{wa}}\right)\left(\frac{Pr}{Sc}\right)^{0.42} \tag{B.7}$$

As the fan speed increases from 3800 to 6300, the predicted h increases from 1.4-1.9x10^{-3} W/cm^2/K at 18 °C and 1.5-2.0x10^{-3} W/cm^2/K at 35 °C. Thus, the pure-water evaporation experiments serve to establish both k_m and h, which are then used in the dissolution-diffusion model for predicting evaporation rate and surface temperature.

Appendix C. Apparatus heat transfer

In §4.2, we developed a 1-D model to predict evaporation rates from and temperatures of an evaporating water surface including the effects of substrate heating and the presence of a spread duplex-oil film. The 1-D model requires modification to describe the behavior of the miniature Langmuir trough used in our experiments because the trough edges are not completely insulated and the temperature at the bottom of the substrate is not strictly uniform. As a result, the water-surface temperature is nonuniform. We use a pseudo-1-D heat-transfer model to account for heat flow from the trough walls, defined as $\dot{Q}_W$ [W], which is small but not negligible. Upon rewriting the energy balance at the water/oil interface in Eq. 22 to include heat transfer from the walls, we find

$$0 = q_S A + \dot{Q}_W - q_F A - J_F \Delta\tilde{H}_S A \tag{C.1}$$

where A is the area of the evaporating surface, and all other variables are defined in §4.2.2. If the trough is not heated, then $q_S = 0$. In the absence of a film, J_0 replaces J_F and $\Delta\tilde{H}_V$ replaces

$\Delta\tilde{H}_S$ in Eq. C.1. $\dot{Q}_W$ is expressed in terms of a heat-transfer coefficient and a temperature driving force:

$$\dot{Q}_W = UA_W\left(T_{hot} - T_{wo}\right) \tag{C.2}$$

where U is the overall heat-transfer coefficient between the water surface and the heat source, A_W is the effective area over which heat transfer occurs, and T_{hot} is the hot temperature acting as a heat source. When the substrate is heated, $T_{hot} = T_b$, the temperature at the bottom of the trough. Without heating $T_{hot} = T_\infty$, the temperature of the ambient air. Neither U nor A_W can be obtained independently, but the product UA_W is a constant characteristic of the apparatus. Solution of Eqs. C.1 and 23 results in modified versions of Eqs. 24 and 27 that describe T_{SF} and T_{S0}. The difference is that U_W from Eq. 25 is now redefined as

$$U_W = \frac{k_w}{H} + \frac{UA_W}{A} \tag{C.3}$$

Modified Eqs. 24 and 27 describe T_{SF} and T_{S0} when the water substrate is heated.

For experiments conducted without substrate heating, Eqs. 24 and 27 further simplify to

$$T_{SF} = T_\infty - \frac{J_F \Delta\tilde{H}_V}{U_F + UA_W/A} \tag{C.4}$$

and

$$T_{S0} = T_\infty - \frac{J_0 \Delta\tilde{H}_V}{h + UA_W/A} \tag{C.5}$$

In the pure-water evaporation experiments, all values in Eq. C.5 are known or measured except UA_W. Therefore, the modified Eq. 27 is solved to determine UA_W in the case where the trough is heated, and Eq. C.5 is solved in the case where it is not heated. Results from all experiments show that UA_W is larger when the substrate is heated than when it is not and has a standard deviation of 10-17 %.

Appendix D. Experimental conditions and apparatus properties

Evaporation-reduction measurements were carried out over a 2-year span, so the environmental conditions were slightly different. There are three sets of data: MOx/BSM without substrate heating; MOx/BSM with substrate heating; and BM with substrate heating. We outline the average conditions for each of these sets of data in Table 2. The measured quantities T_{S0}, T_∞, R_H, and j_0 are reported, followed by the calculated values for k_m, h, and UA_W. Reported values are averaged over the entire set of clean-water experiments that are conducted for a given oil system. Each data set contains over 30-40 measurements.

References

[1] Hedestrand G. On the influence of thin surface films on the evaporation of water. J Phys Chem. 1924;28:1245-52.

[2] Rideal EK. On the influence of thin surface films on the evaporation of water. J Phys Chem. 1925;29:1585-8.

[3] Barnes GT. The effects of monolayers on the evaporation of liquids. Adv Colloid Interface Sci. 1986;25:89-200.

[4] Harkins WD. A general thermodynamic theory of the spreading of liquids to form duplex films and of liquids or solids to form monolayers. J Chem Phys. 1941;9:552-68.

[5] Heymann E, Yoffe A. The stability of multimolecular films of hydrocarbon oils, containing spreaders, on water surfaces. Trans Faraday Soc. 1942;38:408-17.

[6] Langmuir I. Oil lenses on water and the nature of monomolecular expanded films. J Chem Phys. 1933;1:756-76.

[7] Sebba F, Briscoe HVA. The evaporation of water through unimolecular films. J Chem Soc. 1940;39:106-14.

[8] Langmuir I, Schaefer VJ. Rates of evaporation of water through compressed monolayers on water. J Franklin Inst. 1943;235:119-62.

[9] Docking AR, Heymann E, Kerley LF, Mortensen KN. Evaporation of water through multimolecular films. Nature. 1940;146:265.

[10] Bursztyn I. Evaporation Reduction of Water. Nature. 1966;211:521.

[11] Mansfield WW. Effect of Surface Films on the Evaporation of Water. Nature. 1953;172:1101.

[12] (No authors listed). The definition and classification of dry eye disease: report of the Definition and Classification Subcommittee of the International Dry Eye Workshop (2007). Ocul Surf. 2007;5:75-92.

[13] Borchman D, Foulks GN, Yappert MC, Mathews J, Leake K, Bell J. Factors affecting evaporation rates of tear film components measured in vitro. Eye Contact Lens. 2009;35:32-7.

[14] Herok GH, Mudgil P, Millar TJ. The effect of meibomian lipids and tear proteins on evaporation rate under controlled in vitro conditions. Curr Eye Res. 2009;34:589-97.

[15] (No authors listed). The epidemiology of dry eye disease: report of the Epidemiology Subcommittee of the International Dry Eye WorkShop (2007). Ocul Surf. 2007;5:93-107.

[16] King-Smith PE, Fink B, Hill R, Koelling K, Tiffany JM. The Thickness of the Tear Film. Curr Eye Res. 2004;29:357-68.

[17] Korb DR, Craig JP, Doughty M, Guillon J-P, Smith G, Tomlinson A. The Tear Film: structure, function, and clinical examination. Oxford: Butterworth-Heinemann; 2002.

[18] Bron AJ, Tiffany JM, Gouveia SM, Yokoi N, Voon LW. Functional aspects of the tear film lipid layer. Exp Eye Res. 2004;78:347-60.

[19] McDonald JE. Surface Phenomena of Tear Films. Trans Am Ophthalmol Soc. 1968;66:905-39.

[20] Craig JP, Tomlinson A. Importance of the lipid layer in human tear film stability and evaporation. Optom Vis Sci. 1997;74:8-13.

[21] Mishima S, Maurice DM. The oily layer of the tear film and evaporation from the corneal surface. Exp Eye Res. 1961;1:39-45.

[22] Wolff E. The muco-cutaneous junction of the lid-margin and th distribution of the tear fluid. Trans Ophthalmol Soc U K. 1946;66.

[23] Gilbard JP, Farris RL. Tear Osmolarity and Ocular Surface Disease in Keratoconjunctivitis Sicca. Arch Ophthalmol. 1979;97:1642-6.

[24] Gilbard JP, Farris RL, Santamaria J. Osmolarity of Tear Microvolumes in Keratoconjunctivitis Sicca. Arch Ophthalmol. 1978;96:677-81.

[25] Bron AJ, Yokoi Y, Gaffney EA, Tiffany JM. Predicted Phenotypes of Dry Eye: Proposed Consequences of Its Natural History. Ocul Surf. 2009;7:78-92.

[26] Baudouin C. The Pathology of Dry Eye. Surv Ophthalmol. 2001;45:S211-S20.

[27] Gilbard JP, Carter JB, Sang DN, Refojo MF, Hanninen LA, Kenyon KR. Morphological Effect of Hyperosmolarity on Rabbit Corneal Epithelium. Ophthalmol. 1984;91:1205-12.

[28] Khanal S, Tomlinson A, Diaper CJM. Tear Physiology of Aqueous Deficiency and Evaporative Dry Eye. Optom Vis Sci. 2009;86:1235-40.

[29] Khanal S, Tomlinson A, McFayden A, Diaper CJM, Ramaesh K. Dry Eye Diagnosis. Invest Ophthalmol Vis Sci. 2008;49:1407-14.

[30] Tomlinson A, Khanal S, Ramaesh K, Diaper CJM, McFayden A. Tear Film Osmolarity: Determination of a Referent for Dry Eye Diagnosis. Invest Ophthalmol Vis Sci. 2006;47:4309-15.

[31] Isreb MA, Greiner JV, Korb DR, Glonek T, Mody SS, Finnemore VM, et al. Correlation of lipid layer thickness measurements with fluorescein tear film break-up time and Schirmer's test. Eye. 2003;17:79-83.

[32] Iwata S, Lemp MA, Holly FJ, Dohlman CH. Evapoartion Rate of Water from the Precorneal Tear Film and Cornea in the Rabbit. Invest Ophthalmol. 1969;8:613-9.

[33] Brown SI, Dervichian DG. The oils of the meibomian glands: physical and surface characteristics. Arch Ophthalmol. 1969;82:537-40.

[34] Goto E, Shimazaki J, Monden Yu, Takano Y, Yagi Y, Shimmura S, et al. Low-concentration homogenized castor oil eye drops for noninflamed obstructive meibomian gland dysfunction. Ophthalmol. 2002;109:2030-5.

[35] Khanal S, Tomlinson A, Pearce EI, Simmons PA. Effect of an Oil-in-Water Emulsion on the Tear Physiology of Patients With Mild to Moderate Dry Eye. Cornea. 2007;26:175-81.

[36] Korb DR, Scaffidi RC, Greiner JV, Kenyon KR, Herman JP, Blackie CA, et al. The Effect of Two Novel Lubricant Eye Drops on Tear Film Lipid Layer Thickness in Subjects With Dry Eye Symptoms. Optom Vis Sci. 2005;82:594-601.

[37] Blodgett KB. Interference Colors in Oil Films on Water. J Opt Soc Am. 1934;24:313-5.

[38] Holly FJ. Surface chemistry of tear film component analogs. J Colloid Interface Sci. 1974;49:221-31.

[39] Langmuir I, Schaefer VJ. The effect of dissolved salts on insoluble monolayers. J Am Chem Soc. 1937;59:2400-14.

[40] Brown SI, Dervichian D. Hydrodynamics of Blinking - In Vitro Study of the Interaction of the Superficial Oily Layer and the Tears. Arch Ophthalmol. 1969;82:541-7.

[41] Balsbaugh JC, Assaf AG, Pendleton WW. Mineral oil deterioration. Ind Eng Chem. 1941;33:1321-30.

[42] Hicks-Bruun MM, Ritz BL, Ledley RE, Bruun JH. Mineral oil oxidation. Ind Eng Chem. 1944;36:562-8.

[43] Zuidema HH. Oxidation of Lubricating Oils. Chem Rev. 1946;38:197-226.

[44] Lazzari M, Chiantore O. Drying and oxidative degradation of linseed oil. Polym Degrad Stab. 1999;65:303-13.

[45] Powell RW. The influence of surface films of oil on the evaporation of water. Trans Faraday Soc. 1943;39:311-8.

[46] Langmuir I, Langmuir DB. The effect of monomolecular films on the evaporation of ether solutions. J Phys Chem. 1927;31:1719-31.

[47] Gilby AR, Heymann E. The rate of evaporation of water through duplex films. Aust J Sci Res A. 1948;1:197-212.

[48] Fox RC. An Oil-Wax-Surfactant System for Retarding Evaporation of Water. Nature. 1965;205:1004.

[49] Ehlers N. The precorneal film: Biomicroscopical, histological and chemical investigations. Acta Ophthalmol. 1965:1-136.

[50] Butovich IA. Cholesteryl esters as a depot for very long chain fatty acids in human meibum. J Lipid Res. 2009;50:501-13.

[51] Butovich IA. The Meibomian Puzzle: Combining pieces together. Prog Retin Eye Res. 2009;28:483-98.

[52] Butovich IA. Lipidomics of human Meibomian gland secretions: Chemistry, biophysics, and physiological role of Meibomian lipids. Prog Lipid Res. 2011;50:278-301.

[53] Butovich IA, Millar TJ, Ham BM. Understanding and analyzing meibomian lipids - A review. Curr Eye Res. 2008;33:405-20.

[54] Butovich IA, Uchiyama E, McCulley JP. Lipids of human meibum: mass-spectrometric analysis and structural elucidation. J Lipid Res. 2007;48:2220-35.

[55] Butovich IA, Wojtowicz JC, Molai M. Human tear film and meibum. Very long chain wax esters and (O-acyl)-omega-hydroxy fatty acids of meibum. J Lipid Res. 2009;50:2471-85.

[56] Chen JZ, Green-Church KB, Nichols KK. Shotgun Lipidomic Analysis of Human Meibomian Gland Secretions with Electrospray Ionization Tandem Mass Spectrometry. Invest Ophthalmol Vis Sci. 2010;51:6220-31.

[57] Nicolaides N, Kaitaranta JK, Rawdah TN, Macy JI, Boswell FM, Smith RE. Meibomian Gland Studies - Comparison of Steer and Human Lipids. Invest Ophthalmol Vis Sci. 1981;20:522-36.

[58] Nicolaides N, Ruth EC. Unusual Fatty-Acids in the Lipids of Steer and Human Meibomian Gland Excreta. Curr Eye Res. 1982;2:93-8.

[59] Aronowicz JD, Shine WE, McCulley JP. Tear measurement in patients with keratoconjunctivitis sicca. Invest Ophthalmol Vis Sci. 2003;44:U640.

[60] Goto E, Endo K, Suzuki A, Fujikura Y, Matsumoto Y, Tsubota K. Tear evaporation dynamics in normal subjects and subjects with obstructive meibomian gland dysfunction. Invest Ophthalmol Vis Sci. 2003;44:533-9.

[61] Hamano H, Hori M, Kawabe H, Mitsunaga S, Ohnishi Y, Koma I. Modification of the superficial layer of the tear film by the secretion of the meibomian glands. Folia Ophthalmol Japonica. 1980;31:353-60.

[62] Mathers WD. Ocular evaporation in meibomian gland dysfunction and dry eye. Ophthalmol. 1993;100:347-51.

[63] Mathers WD, Binarao G, Petroll M. Ocular Water Evaporation and the Dry Eye - A New Measuring Device. Cornea. 1993;12:335-40.

[64] Mathers WD, Daley TE. Tear flow and evaporation in patients with and without dry eye. Ophthalmol. 1996;103:664-9.

[65] Mathers WD, Lane JA, Sutphin JE, Zimmerman MB. Model for ocular tear film function. Cornea. 1996;15:110-9.

[66] Rolando M, Refojo MF, Kenyon KR. Increased Tear Evaporation Rates in Eyes with Keratoconjunctivitis Sicca. Arch Ophthalmol. 1983;101:557-8.

[67] Shimazaki J, Sakata M, Tsubota K. Ocular Surface Changes and Discomfort in Patients with Meibomian Gland Dysfunction. Arch Ophthalmol. 1995;113:1266-70.

[68] Nichols JJ, Mitchell GJ, King-Smith PE. Thinning Rate of the Precorneal and Prelens Tear Films. Invest Ophthalmol Vis Sci. 2005;46:2353-61.

[69] Rolando M, Refojo MF. Tear evaporimeter for measuring water evaporation rate from the tear film under controlled conditions in humans. Exp Eye Res. 1983;36:25-33.

[70] Tomlinson A, Doane MG, McFayden A. Inputs and Outputs of the Lacrimal System: Review of Production and Evaporative Loss. Ocul Surf. 2009;7:186-98.

[71] Trees GR, Tomlinson A. Effect of Artificial Tear Solutions and Saline on Tear Film Evaporation. Optom Vis Sci. 1990;67:886-90.

[72] Tsubota K, Yamada M. Tear Evaporation from the Ocular Surface. Invest Ophthalmol Vis Sci. 1992;33:2942-50.

[73] Liu DTS, Di Pascuale MA, Sawai J, Gao YY, Tseng SCG. Tear film dynamics in floppy eyelid syndrome. Invest Ophthalmol Vis Sci. 2005;46:1188-94.

[74] Miano F, Calcara M, Giuliano F, Millar TJ, Enea V. Effect of meibomian lipid layer on evaporation of tears. J Phys Condens Matter. 2004;16:S2461-S7.

[75] Rantamäki AH, Javanainen M, Vattulainen I, Holopainen JM. Do Lipids Retard the Evaporation of the Tear Fluid? Invest Ophthalmol Vis Sci. 2012;53:6442-7.

[76] Doane MG. An Instrument for In Vivo Tear Film Interferometry. Optom Vis Sci. 1989;66:383-8.

[77] Fatt I, Weissman BA. Physiology of the Eye: An Introduction to the Vegetative Functions. 2nd ed. Stoneham, MA: Butterworth-Heinemann; 1992. p. 227.

[78] Goto E, Dogru M, Kojima T, Tsubota K. Computer-synthesis of an interference color chart of human tear lipid layer, by a colorimetric approach. Invest Ophthalmol Vis Sci. 2003;44:4693-7.

[79] Guillon J-P. Tear film photography and contact lens wear. Cont Lens Anterior Eye. 1982;5:84-7.

[80] King-Smith PE, Hinel EA, Nichols JJ. Application of a novel interferometric method to investigate the relation between lipid layer thickness and tear film thinning. Invest Ophthalmol Vis Sci. 2010;51:2418-23.

[81] Korb DR, Greiner JV, Glonek T, Whalen A, Hearn SL, Esway JE, et al. Human and rabbit lipid layer and interference pattern observations. Lacrimal Gland, Tear Film, and Dry Eye Syndromes 2: Basic Science and Clinical Relevance. Vol. 438. New York: Plenum Press Div Plenum Publishing Corp; 1998. p. 305-8.

[82] King-Smith PE, Nichols JJ, Braun RJ, Nichols KK. High Resolution Microscopy of the Lipid Layer of the Tear Film. Ocul Surf. 2011;9:197-211.

[83] Rosenfeld L, Cerretani C, Leiske DL, Toney M, Radke CJ, Fuller GG. Structural and rheological properties of meibomian lipids. Invest Ophthalmol Vis Sci. 2013.

[84] Tiffany JM, Dart J. Normal and Abnormal Functions of the Meibomian Secretion. R Soc Med Int Congr Symp Ser. 1981;40:1061-4.

[85] Langmuir I. The constitution and fundamental properties of solids and liquids. II. Liquids. J Am Chem Soc. 1917;39:1848-906.

[86] Ushijima Y, Ushijima B, Ohtomi E, Takata Y, Takiue T, Aratono M, et al. Line tension at freezing transition of alkane wetting film on aqueous surfactant solutions. Colloids and Surfaces A: Physicochemical and Engineering Aspects. 2011;390:33-9.

[87] Takata Y, Matsubara H, Kikuchi Y, Ikeda N, Matsuda T, Takiue T, et al. Line Tension and Wetting Behavior of an Air/Hexadecane/Aqueous Surfactant System. Langmuir. 2005;21:8594-6.

[88] Rowlinson J, Widom B. Molecular Theory of Capillarity. Oxford: Clarendon Press; 1982. p. 212-17.

[89] Gibbs JW. The Collected Works of J. Willard Gibbs. Vol. 1. New York: Longmans; 1928. p. 258.

[90] Pomerantz P, Clinton WC, Zisman WA. Spreading Pressures and Coefficients, Interfacial Tensions, and Adhesion Energies of the Lower Alkanes, Alkenes, and Alkyl Benzenes on Water. J Colloid Interface Sci. 1967;24:16-28.

[91] Cerretani C, Radke CJ. Human tear lipid breaks up by dewetting. 6th International Conference on the Tear Film and Ocular Surface. Florence, Italy 2010.

[92] Wyart FB, Martin P, Redon C. Liquid/liquid dewetting. Langmuir. 1993;9:3682-90.

[93] Sharma A, Ruckenstein E. Dewetting of Solids by the Formation of Holes in Macroscopic Liquid Films. J Colloid Interface Sci. 1989;133:358-68.

[94] Martin P, Buguin A, Brochardwyart F. Bursting of a Liquid Film on a Liquid Substrate. Europhys Lett. 1994;28:421-6.

[95] Craster RV, Matar OK. Dynamics and stability of thin liquid films. Rev Mod Phys. 2009;81:1131-98.

[96] Lambooy P, Phelan KC, Haugg O, Krausch G. Dewetting at the liquid-liquid interface. Phys Rev Lett. 1996;76:1110-3.

[97] Hertz H. Ueber den druck des gesättigten quecksilberdampfes. Ann Phys. 1882;253:193-200.

[98] Knudsen M. Die maximale verdampfungsgeschwindigkeit des quecksilbers. Ann Phys. 1915;352:697-708.

[99] Alty T. The Reflection of vapour molecules at a liquid zurface. Proc R Soc Lond. 1931;131:554-64.

[100] Cammenga HK. Evaporation Mechanisms of Liquids. In: Kaldis E, (editor). Current Topics in Material Science. Vol. 4: North Holland Publishing Company; 1980. p. 335-46.

[101] Schrage R. A Theoretical Study of Interphase Mass Transfer. New York: Columbia University Press; 1953.

[102] Bonacci J, Myers A, Nongbri G, Eagleton L. The Evaporation and Condensation Coefficient of Water, Ice, and Carbon Tetrachloride. Chem Eng Sci. 1976;31:609-17.

[103] Eames I, Marr N, Sabir H. The Evaporation Coefficient of Water: A Review. Int J Heat Mass Transf. 1997;40:2963-73.

[104] Bird R, Stewart W, Lightfoot E. Transport Phenomena. 2nd ed. New York: John Wiley & Sons, Inc.; 2002. ch. 14, 22.

[105] Welty J, Wicks C, Wilson R, Rorrer G. Fundamentals of Momentum, Heat, and Mass Transfer. 4th ed. New York: John Wiley & Sons, Inc.; 2001. ch. 30.

[106] Green D, Perry R. Perry's Chemical Engineer's Handbook. 8th ed. New York: McGraw-Hill; 2008. p. 5-64 – 5-65.

[107] Martin H. Heat and mass transfer between impinging gas jets and solid surfaces. In: James PH, Thomas FI, (editors). Advances in Heat Transfer. Vol. 13: Elsevier; 1977. p. 1-20.

[108] Bradley RS, Evans MG, Whytlaw-Gray RW. The rate of evaporation of droplets. evaporation and diffusion coefficients, and vapour pressures of dibutyl phthalate and butyl stearate. Proc R Soc L A Math Phys Sci. 1946;186:368-90.

[109] Fuchs N. Über die Verdampfungsgeschwindigkeit kleiner tröpfchen in einer gasatmosphäre. Physikalische zeitschrift der Sowjetunion. 1934;6:224-43.

[110] Assouline S, Narkis K, Or D. Evaporation suppression from water reservoirs: Efficiency considerations of partial covers. Water Resour Res. 2011;47.

[111] Stefan J. Ueber die verdampfung aus einen kreisforming oder elliptisch begrenzten becken. Sitzungsberichte der Königlich Preussischen Akademie der Wissenschaften II. 1881;83:943-54.

[112] Archer RJ, Lamer VK. The Rate of Evaporation of Water through Fatty Acid Monolayers. J Phys Chem. 1955;59:200-8.

[113] Siddiqi MA, Lucas K. Correlations for Prediction of Diffusion in Liquids. Can J Chem Eng. 1986;64:839-43.

[114] Leiske DL, Miller CE, Rosenfeld L, Cerretani C, Ayzner A, Lin B, et al. Molecular Structure of Interfacial Human Meibum Films. Langmuir. 2012;28:11858-65.

[115] Girard F, Antoni Ml, Sefiane K. Infrared Thermography Investigation of an Evaporating Sessile Water Droplet on Heated Substrates. Langmuir. 2010;26:4576-80.

[116] Girard F, Antoni Ml, Sefiane K. Use of IR Thermography To Investigate Heated Droplet Evaporation and Contact Line Dynamics. Langmuir. 2011;27:6744-52.

[117] Blackie CA, Solomon JD, Scaffidi RC, Greiner JV, Lemp MA, Korb DR. The Relationship Between Dry Eye Symptoms and Lipid Layer Thickness. Cornea. 2009;28:789-94.

[118] Josephson JE. Appearance of the Preocular Tear Film Lipid Layer. Am J Optom Physiol Opt. 1983;60:883-7.

[119] Felder R, Rousseau R. Elementary Principles of Chemical Processes. Third ed. New York, NY: John Wiley & Sons, Inc.; 2000. p. 385.

[120] Doane MG. Interaction of Eyelids and Tears in Corneal Wetting and the Dynamics of the Normal Human Eyeblink Am J Ophthalmol. 1980;89:507-16.

[121] Du Y, Mamishev AV, Lesieutre BC, Zahn M, Kang SH. Moisture solubility for differently conditioned transformer oils. IEEE Trans Dielectr Electr Insul. 2001;8:805-11.

[122] Hilder MH. Solubility of Water in Edible Oils and Fats. J Am Oil Chem Soc. 1968;45:703-7.

[123] Schatzberg P. Diffusion of water through hydrocarbon liquids. Polym Rev. 1965;10:87-92.

[124] Gum JR. Mucin Genes and the Proteins They Encode: Structure, Diversity, and Regulation. American Journal of Respiratory Cell and Molecular Biology. 1992;7:557-64.

[125] Tsuji T, Osawa T. Carbohydrate structures of bovine submaxillary mucin. Carbohydrate research. 1986;151:391-402.

[126] Leiske D, Leiske C, Leiske D, Toney M, Senchyna M, Ketelson H, et al. Temperature-induced transitions in the structure and interfacial rheology of human meibum. Biophys J. 2012;102:369-76.

[127] Kamao T, Yamaguchi M, Kawasaki S, Mizoue S, Shiraishi A, Ohashi Y. Screening for Dry Eye With Newly Developed Ocular Surface Thermographer. Am J Ophthalmol. 2011;151:782-91.

[128] Baldwin PEJ, Maynard AD. A survey of wind speeds in indoor workplaces. Ann Occ Hyg. 1998;42:303-13.

[129] Chin DT, Tsang CH. Mass Transfer for an Impinging Jet Electrode. J Electrochem Soc. 1978;125:1461-70.

[130] Murube J. Tear Osmolarity. Ocul Surf. 2006;4:62-73.

[131] Korb DR, Blackie CA. Meibomian Gland Therapeutic Expression: Quantifying the Applied Pressure and the Limitation of Resulting Pain. Eye Contact Lens. 2011;37:298-301.

[132] Holly FJ. Personal profile. Ocul Surf 2008;6(3):147-9.

[133] Schlichting H, Gersten K. Boundary-layer theory. 8th ed. Berlin: Springer; 2000.

[134] Obot NT, Trabold TA. On the Rate Balance between Impingement Water Evaporation and Heat Transfer. Int Comm Heat Mass Transf. 1992;19:51-8.

Tables

Table 1: Oil spreading and dewetting on water.

Substance*	**Spreading behavior**** initial spread	duplex film	BUT
mineral oil (MO)	x	x	–
stearyl oleate (SO)	✓	x	–
oleic acid (OA)	✓	x	–
linseed oil (LS)	✓	✓	1 s
olive oil	✓	✓	< 1 s
MO + OA (0.5 wt%)	✓	✓	1 s
MO + DPPC (0.5 wt%)	✓	x	–
MO + $C_{12}E_4$ (0.5 wt%)	✓	x	–
MO, ChO, SO, Ch, DPPC (88, 5, 0.5, 6, 0.5 wt%)	✓	x	–
MO + ChO, Ch (0.4, 0.4 wt%)	✓	✓	5 s
Ch, ChO, SO (1:1:1)	✓	x	–
MO + stand oil (2 wt%)	✓	✓	5 s
oxidized MO (MOx)	✓	✓	5 s
MOx + 145K PIB (1 wt%)	✓	✓	10 s
MOx + BSM (10 wt%)	✓	✓	5 min
human meibum	✓	✓	> 30 min
bovine meibum	✓	✓	> 30 min

* DPPC = dipalmitoyl phosphatidyl choline, $C_{12}E_4$ = Brij 30, ChO = cholesteryl oleate, Ch = cholesterol, PIB = polyisobutylene.

**If 0.5 µL of oil spreads initially, the initial-spread entry is checked. If, in addition, it remains as a film long enough for a uniform duplex film to be visible, the duplex-film entry is checked. For oils that form duplex films, the barriers are blinked once and approximate breakup time is reported (BUT).

Table 2: Evaporation rate from a clean-water surface for both heated and unheated substrate.†

Duplex-oil system:	**MOx/BSM**	**MOx/BSM**	**BM, HM**
Substrate heating:	none	T_b = 45 °C	T_b = 45 °C
j_0* [10^{-5} g/cm^2/s]	1.01 ± 0.18	5.41 ± 0.16	5.93 ± 0.24
T_{S0} [°C]	17.6 ± 0.4	37.2 ± 0.2	36.2 ± 0.3
T_∞ [°C]	22.9 ± 0.2	23.3 ± 0.2	25.0 ± 0.6
R_H [%]	36.7 ± 2.1	42.8 ± 2.5	31.9 ± 5.0
k_m ‡ [cm/s]	1.34 ± 0.14	1.53 ± 0.11	1.71 ± 0.11
h [mW/cm^2/K]	1.44 ± 0.15	1.64 ± 0.12	1.83 ± 0.12
UA_W [mW/K]	63 ± 1	170 ± 10	140 ± 20

† Values are reported as average ± standard deviation over 40 measurements.

* Values for for j_0, T_{S0}, T_∞, and R_H are measured directly.

‡ k_m, h, and UA_W are calculated as described in §5.3.2.

Table 3: Measured water permeability of duplex-oil films.

Substance	**Avg. T_{SF} [°C]**	**Dk [10^{-4} cm^2/s]**
MOx/BSM	20	1.1
MOx/BSM	40	1.6
BM	40	2.6

Figure Captions

Fig. 1. Schematic of an oil lens spreading at the water/air interface. The directions of the oil (γ_o) and water (γ_w) surface tensions and the oil/water interfacial tension (γ_{ow}) are shown in (A). Between (A) and (B), the lens elongates during outward relaxation, as indicated by the horizontal arrows.

Fig. 2. Schematic of a duplex-oil film (gravity free) of initial thickness L_0 with $S < 0$ resting on a water substrate of depth d before and $d+l'$ after hole formation. Hole formation exposes water/air surface of area A_H at the expense of oil/air and oil/water surface areas, A_1 and A_2. Drawing is not to scale.

Fig. 3. Schematic water-concentration profile across a liquid/gas interface during evaporation. There is a discontinuity in concentration at $z = 0$ corresponding to the change in density from liquid to vapor. Within the interfacial region of thickness λ, molecules escape at the kinetic rate. However, to evaporate into the environment, they must convect and diffuse through the air subject to the airflow ($z > \lambda$).

Fig. 4. Schematic of the (A) concentration and (B) temperature profiles through the water, oil-film, and air phases during steady-state evaporation of water with depth H through a film of thickness L for the water substrate heated from the left at temperature T_b. There are discontinuities in concentration at $z = 0$ and $z = L$ corresponding to the solubility of water in oil.

Fig. 5. The evaporation-measurement apparatus. Process measurements and video-camera images are fed continuously to the PC. The entire apparatus is contained within an insulated box (not shown) to minimize temperature and humidity fluctuations, and drafts.

Fig. 6. Interference patterns observed in healthy human lipid layer. (A) Color interference fringes observed in the TFLL [118]. (B) Lipid layer between 60-80 nm thick [78]. (C) Lipid interference patterns for films greater than 75 nm and (D) less than 60 nm [117]. Images from [78, 113, 114] with permission.

Fig. 7. Repeated color interference patterns visualized in a human TFLL immediately after 6 successive blinks for the same human subject. The numbers under each panel indicate the blink number. From [18] with permission.

Fig. 8. Color interference patterns documenting spreading behavior of 0.5-µL oil droplets deposited on water in the miniature Langmuir trough. Each column of images corresponds to a column from Table 1. After initial droplet deposition, the oil may spread (A, MOx) or remain as a lens (D, MO). Upon spreading, the oil may briefly form a visible uniform duplex film (B, MOx) or dewet instantaneously while spreading (E, OA). When a duplex film is formed, the trough barriers were blinked once, and the approximate duplex-film breakup time (BUT) is recorded (C, MOx).

Fig. 9. Surface temperature versus time for an evaporating clean-water surface at a fan speed of 3800 rpm, T_∞ = 22 °C, and R_H = 30 %. The temperature of the water surface drops from ambient temperature to a steady wet-bulb temperature T_{S0} of ~17 °C.

Fig. 10. Mass of clean water in the unheated trough versus time for three different fan speeds: (□) 3800 rpm, (△) 5000 rpm, (○) 6300 rpm. Exact numerical values for each data set are shifted to give the same initial mass for all experiments.

Fig. 11. Surface temperature versus time before and after application of a 2.5-µm MOx/BSM duplex-oil film in an unheated trough. The temperature of the clean-water surface falls to a steady temperature T_{S0} of ~18 °C. After film deposition at t ~ 75 min, the temperature rises, eventually reaching a new steady-state temperature of T_{SF} = 20.7 °C.

Fig. 12. Relative mass of water in the trough versus time at a fan speed of 3800 rpm before and after application of MOx/BSM films of varying thickness in an unheated trough. The mass for each experiment is shown relative to the mass at which the film was applied. (■) clean water, (●) 100-nm film, (○) 500-nm film, (▲) 1-µm film, (△) 2.5-µm film, and (◆) 100-µm film.

Fig. 13. Film resistance, $R-R_m$, versus film thickness, L, for various oil films and temperatures. Squares represent MOx/BSM and circles correspond to bovine meibum (BM). The average surface temperature for the filled symbols is $T_{SF} = 20°C$ and for the open symbols is $T_{SF} = 40°C$. Best linear fits of the data up to 1 µm in thickness are shown.

Fig. 14. Color interference patterns observed in *in-vitro* duplex films of MOx/BSM in the miniature Langmuir trough immediately after 6 successive blinks. The deposited films are 100-nm thick. Each image is taken immediately after the blink number denoted below the frame. (Compare with Fig. 7.)

Fig. 15. Evaporation ratio J_F/J_0 versus oil-film thickness L for MOx/BSM in an unheated trough. Filled squares represent the average experimental values. Error bars denote the standard deviations. Solid line corresponds to theory (Eq. 18) with $k_m = 1.34$ cm/s and $Dk = 1.1 \times 10^{-4}$ cm^2/s, determined by the fit in Fig. 13. Corresponding surface temperatures are given in Fig. 16.

Fig. 16. Surface temperature T_{SF} versus oil-film thickness L for MOx/BSM films in an unheated trough. Filled squares represent the average measured values. Error bars denote the standard deviation. Solid line corresponds to theory (Eq. 24) with the same parameters as in Fig. 15.

Fig. 17. Evaporation ratio J_F/J_0 versus oil-film thickness L for MOx/BSM (■), bovine-meibum (○), and human-meibum (▽) films in a heated trough ($T_b = 45$ °C). Lines represent the theory in Eq. 18 plotted for $Dk = 1.6 \times 10^{-4}$ (solid line, MOx/BSM) and 2.6×10^{-4} cm^2/s (dotted line, BM). Corresponding surface temperatures are shown in Fig. 18.

Fig. 18. Surface temperature T_{SF} versus oil-film thickness L for MOx/BSM (■) and bovine-meibum (○) films in a heated trough ($T_b = 45$ °C). Lines correspond to theory (Eq. 24) with the same parameters as in Fig. 17 (solid line = MOx/BSM, dotted line = BM). T_{S0} is shown at $L = 1$ nm.

Fig. 19. Evaporation ratio J_F/J_0 versus film thickness L for literature data and from theory and data from this study in the heated trough. The solid line and filled squares correspond to theory

and data for heated MOx/BSM films. The dotted line and open circles correspond to theory and data for heated bovine-meibum films. Inverted open triangles are from human meibum experiments in this study. (●) and (▼) correspond to DPPC/Cholesterol and human-meibum films reported by [14]. (▲) are palmitoyl oleate/$C_{14}H_{30}$ films measured by Borchman *et al.* [13]. (◊) are films of MO:eucalyptus oil measured by [47]. (♦) are calculated values for evaporation reduction based on the *Dk* measured by Langmuir and Schaefer [8] for oxidized-turbine-oil duplex films assuming $\phi = 1$. A vertical arrow at 100 nm shows the approximate thickness of the human TFLL.

Fig. 20. Calculated evaporation rate, j_F, versus lipid-layer thickness, L, for various impinging-air speeds, u, for two lipid-layer permeabilities. Open squares and circles on the lines correspond to $Dk = 2.6\text{x}10^{-4}$ and $2.6\text{x}10^{-6}$ cm^2/s. Air speeds of 0.01, 0.1, and 1 m/s (corresponding to nearly stagnant air, ventilated-room air, and walking) are shown with solid, dotted, and dashed lines, respectively. For air speeds 0.01, 0.1, 1 m/s, the corresponding j_0 values are 2.1, 7.4, and $2.6\text{x}10^{-6}$ $g/cm^2/s$, respectively.

Fig. B1. Log-log plot of the measured mass-transfer coefficient [cm/s] versus fan speed [rpm]. Fan speeds used were 3800, 5000, and 6300 rpm. Error bars represent the standard deviation for each point, which was an average of 5-6 experiments. Filled and open squares correspond to data at T_{S0} of 17.2 and 34.7°C, respectively. The slope of both the solid and dotted best-fit lines is $m=0.58$. For the heated substrate, T_b = 43 °C.

Figures

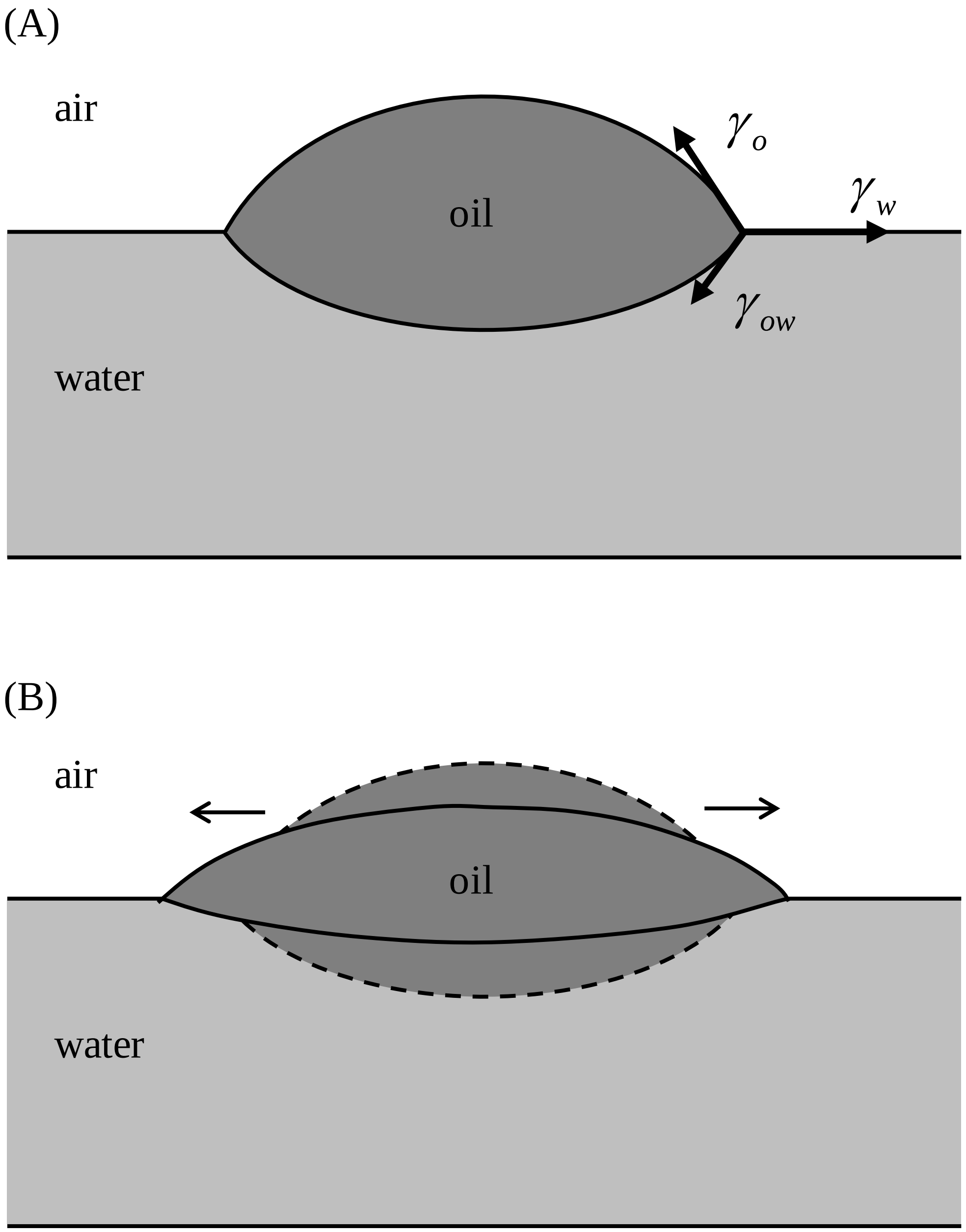

Fig. 1. Schematic of an oil lens spreading at the water/air interface. The directions of the oil (γ_o) and water (γ_w) surface tensions and the oil/water interfacial tension (γ_{ow}) are shown in (A). Between (A) and (B), the lens elongates during outward relaxation, as indicated by the horizontal arrows.

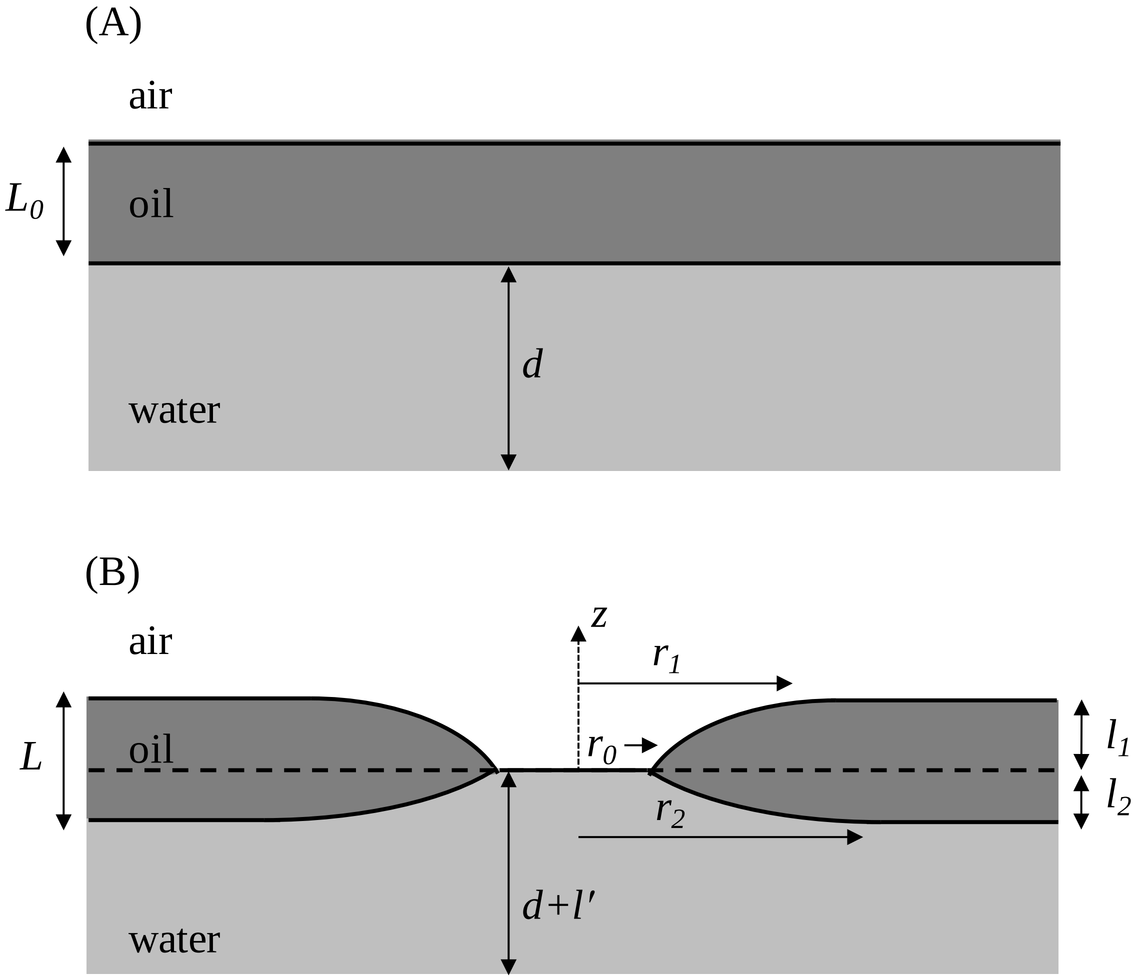

Fig. 2. Schematic of a duplex-oil film (gravity free) of initial thickness L_0 with $S < 0$ resting on a water substrate of depth d before and $d+l'$ after hole formation. Hole formation exposes water/air surface of area A_H at the expense of oil/air and oil/water surface areas, A_1 and A_2. Drawing is not to scale.

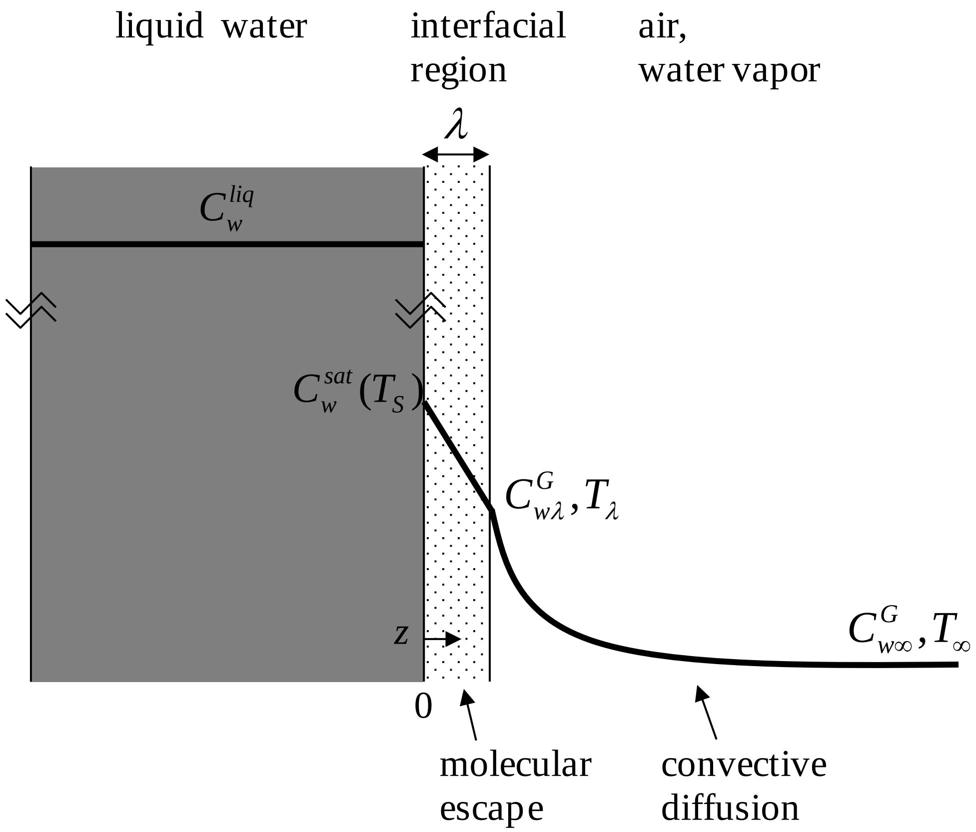

Fig. 3. Schematic water-concentration profile across a liquid/gas interface during evaporation. There is a discontinuity in concentration at $z = 0$ corresponding to the change in density from liquid to vapor. Within the interfacial region of thickness λ, molecules escape at the kinetic rate. However, to evaporate into the environment, they must convect and diffuse through the air subject to the airflow ($z > \lambda$).

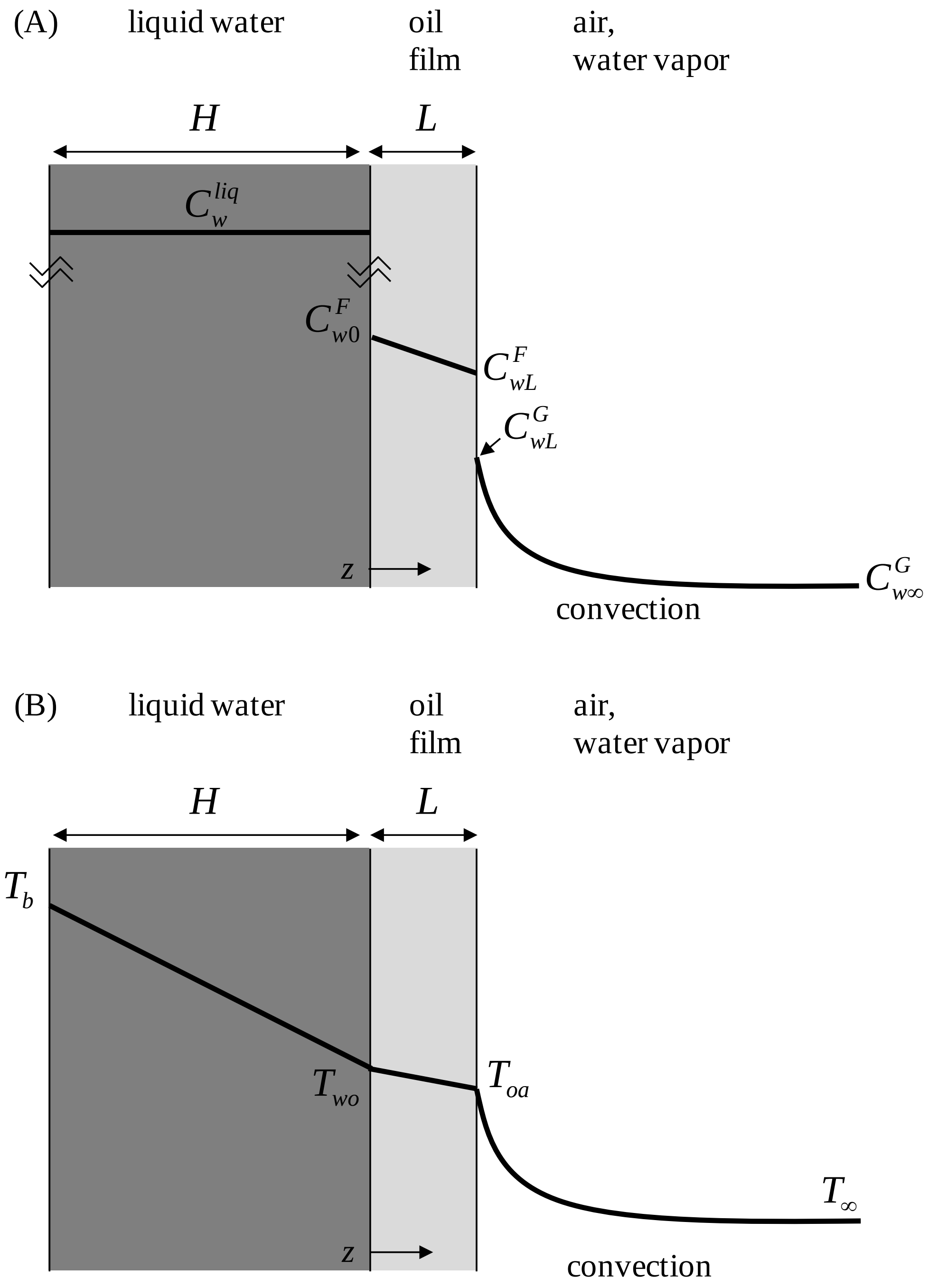

Fig. 4. Schematic of the (A) concentration and (B) temperature profiles through the water, oil-film, and air phases during steady-state evaporation of water with depth *H* through a film of thickness *L* for the water substrate heated from the left at temperature T_b. There are discontinuities in concentration at $z = 0$ and $z = L$ corresponding to the solubility of water in oil.

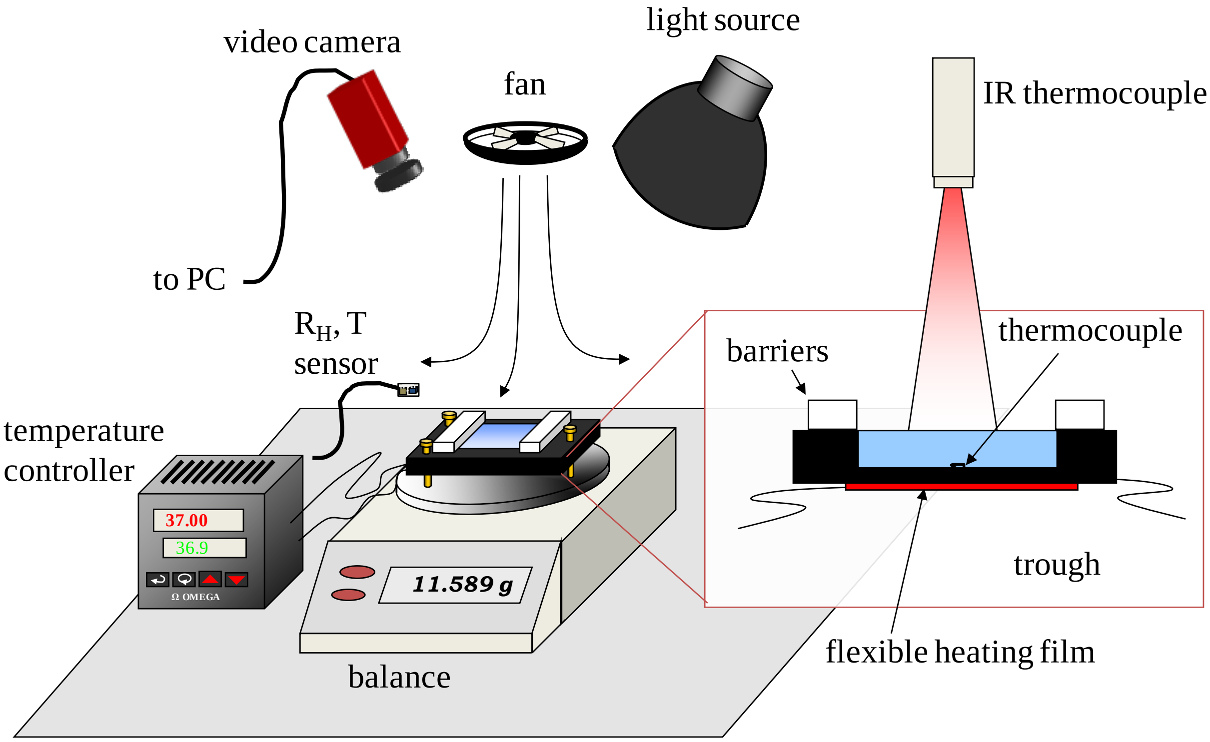

Fig. 5. The evaporation-measurement apparatus. Process measurements and video-camera images are fed continuously to the PC. The entire apparatus is contained within an insulated box (not shown) to minimize temperature and humidity fluctuations, and drafts.

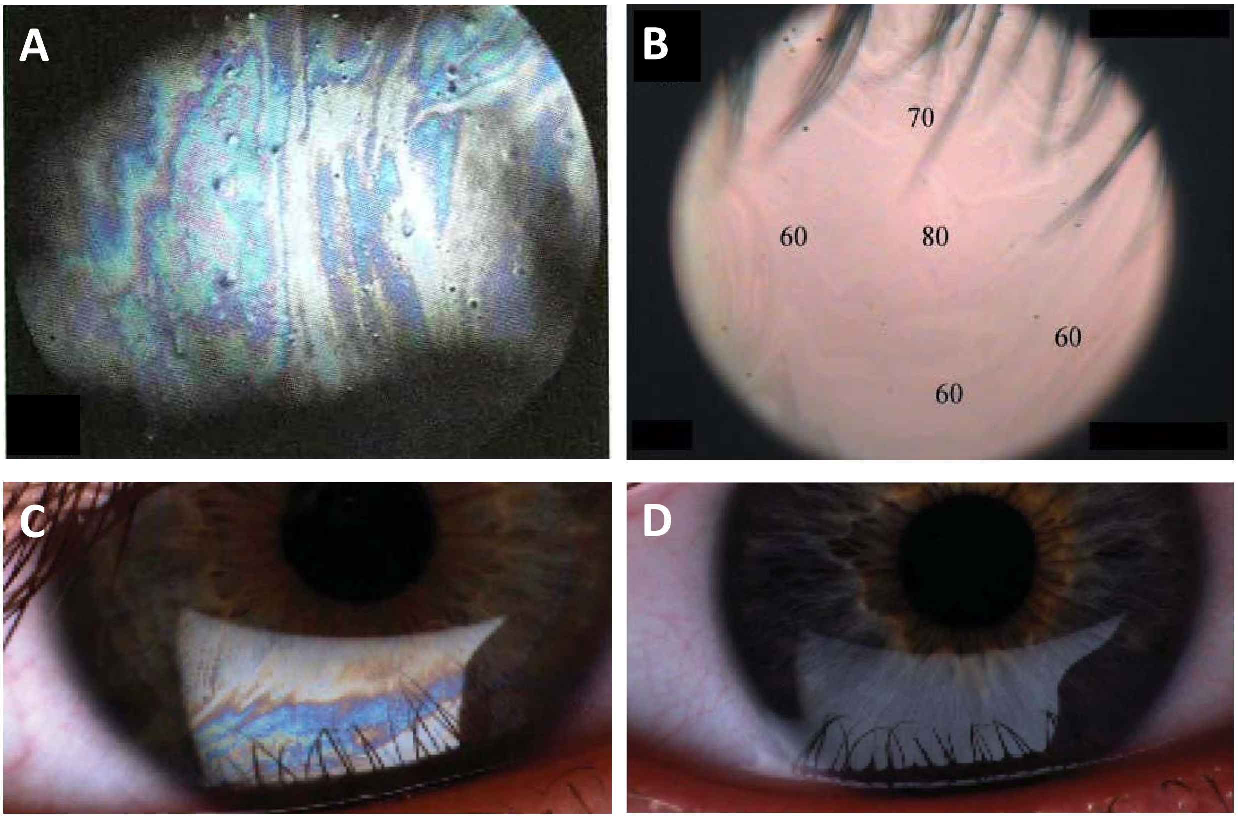

Fig. 6. Interference patterns observed in healthy human lipid layer. (A) Color interference fringes observed in the TFLL [118]. (B) Lipid layer between 60-80 nm thick [78]. (C) Lipid interference patterns for films greater than 75 nm and (D) less than 60 nm [117]. Images from [78, 113, 114] with permission.

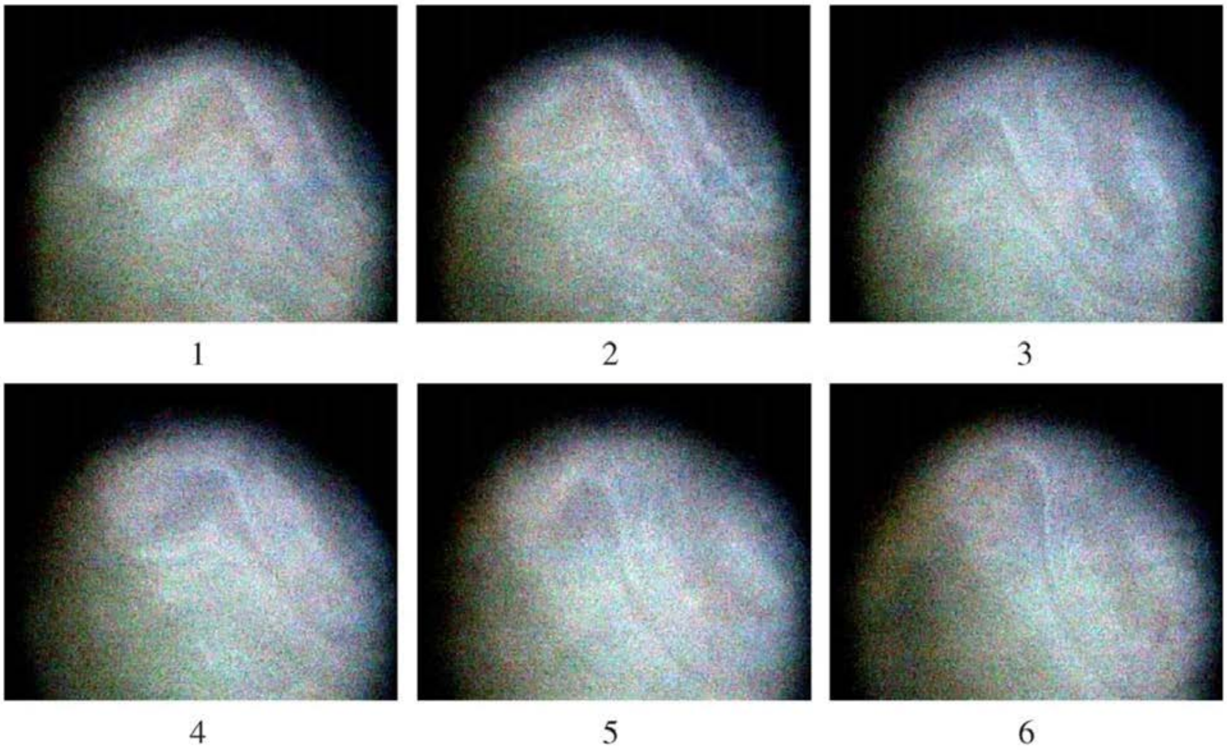

Fig. 7. Repeated color interference patterns visualized in a human TFLL immediately after 6 successive blinks for the same human subject. The numbers under each panel indicate the blink number. From [18] with permission.

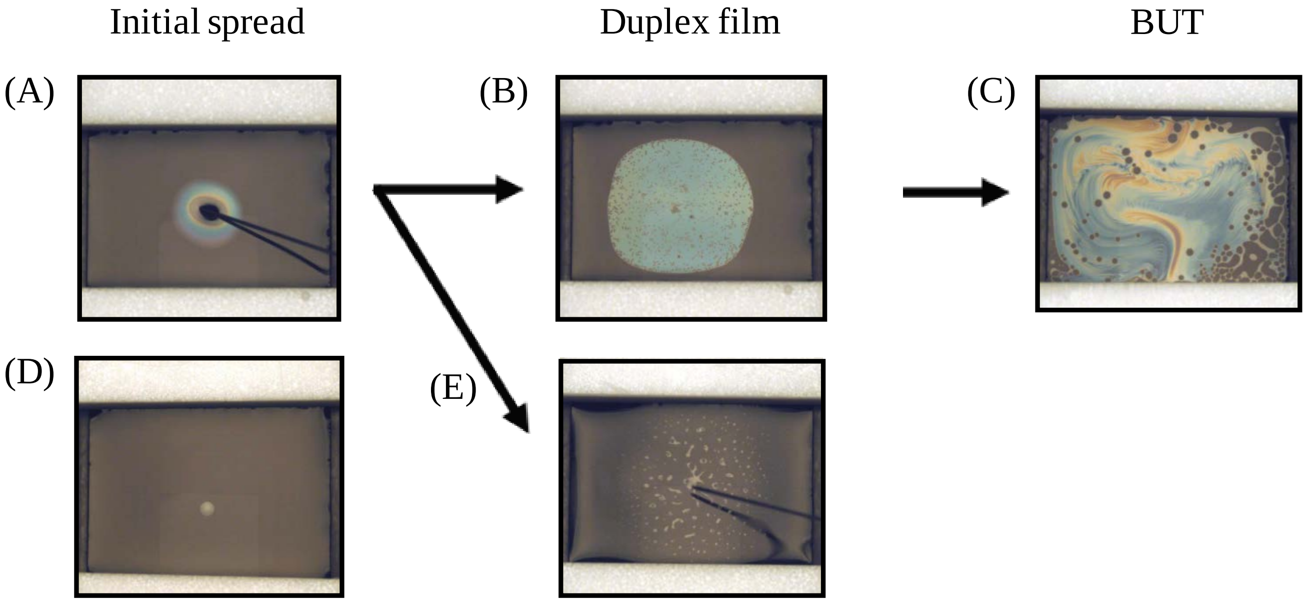

Fig. 8. Color interference patterns documenting spreading behavior of 0.5-µL oil droplets deposited on water in the miniature Langmuir trough. Each column of images corresponds to a column from Table 1. After initial droplet deposition, the oil may spread (A, MOx) or remain as a lens (D, MO). Upon spreading, the oil may briefly form a visible uniform duplex film (B, MOx) or dewet instantaneously while spreading (E, OA). When a duplex film is formed, the trough barriers were blinked once, and the approximate duplex-film breakup time (BUT) is recorded (C, MOx).

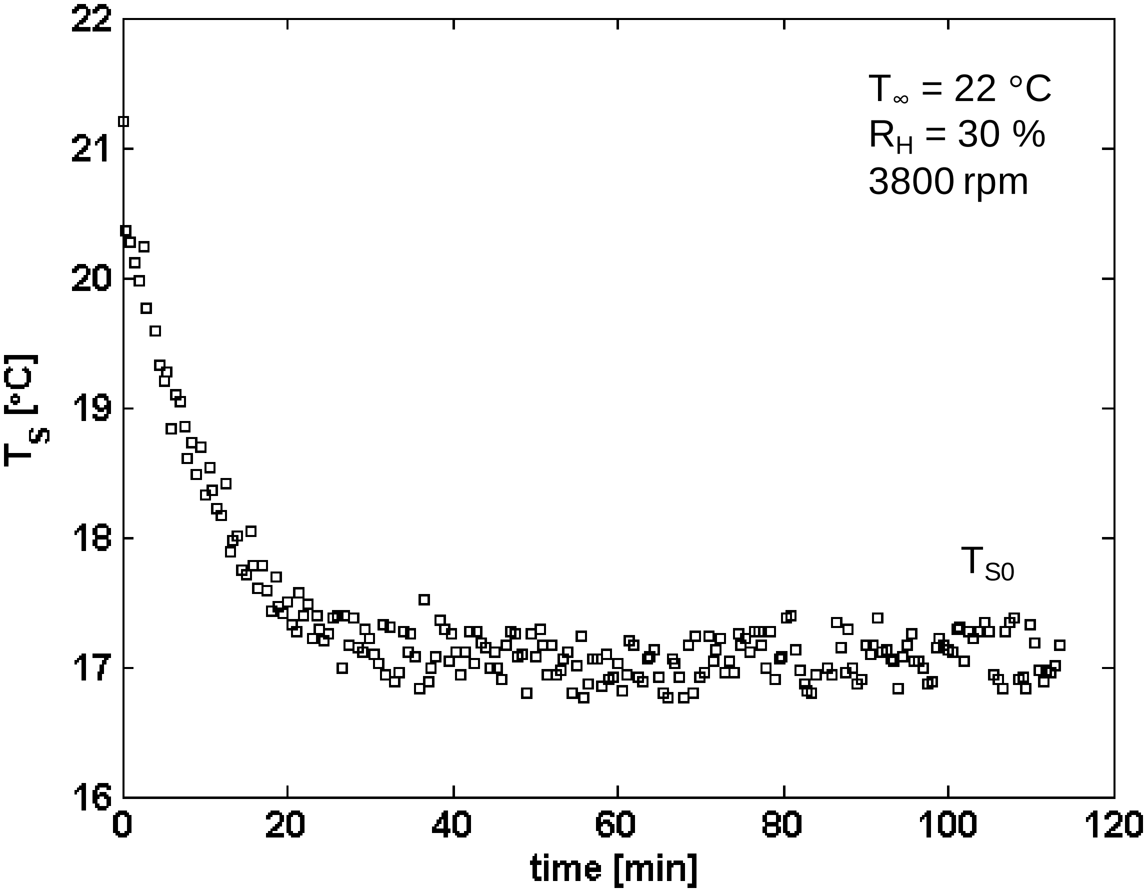

Fig. 9. Surface temperature versus time for an evaporating clean-water surface at a fan speed of 3800 rpm, T_∞ = 22 °C, and R_H = 30 %. The temperature of the water surface drops from ambient temperature to a steady wet-bulb temperature T_{S0} of ~17 °C.

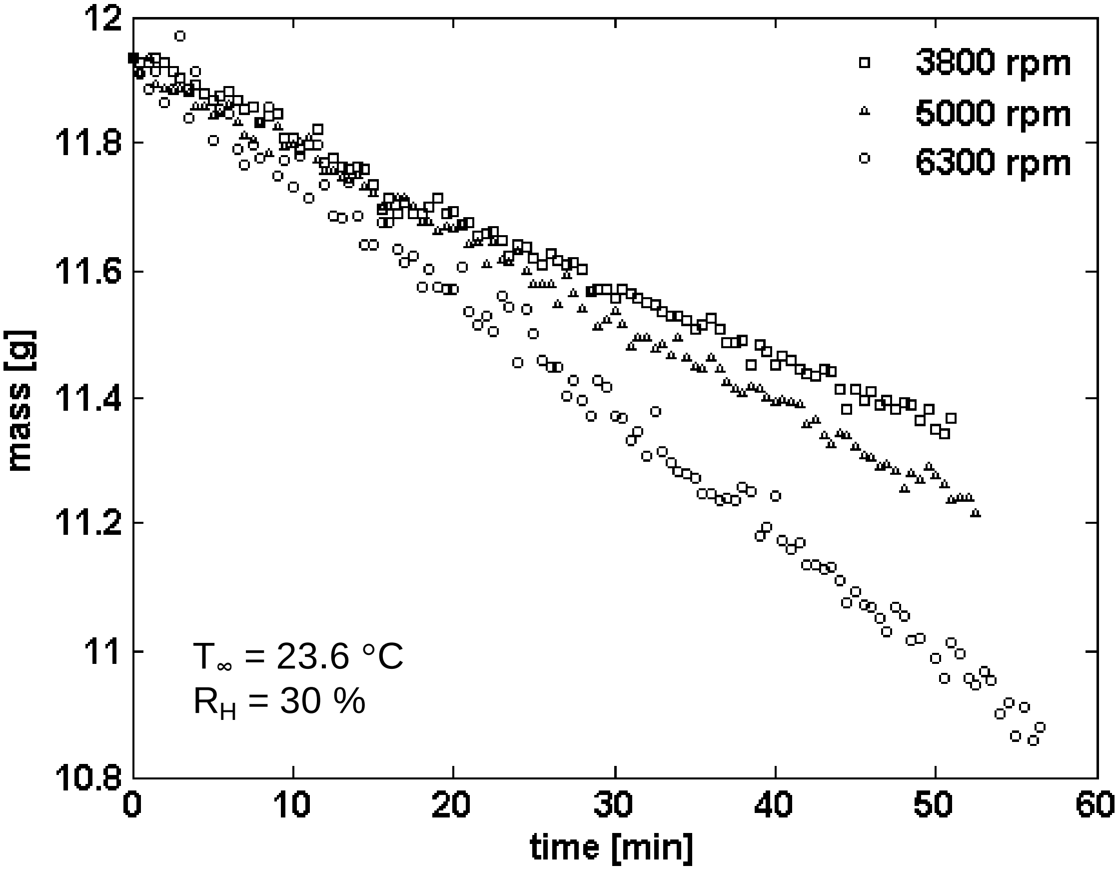

Fig. 10. Mass of clean water in the unheated trough versus time for three different fan speeds: (□) 3800 rpm, (△) 5000 rpm, (○) 6300 rpm. Exact numerical values for each data set are shifted to give the same initial mass for all experiments.

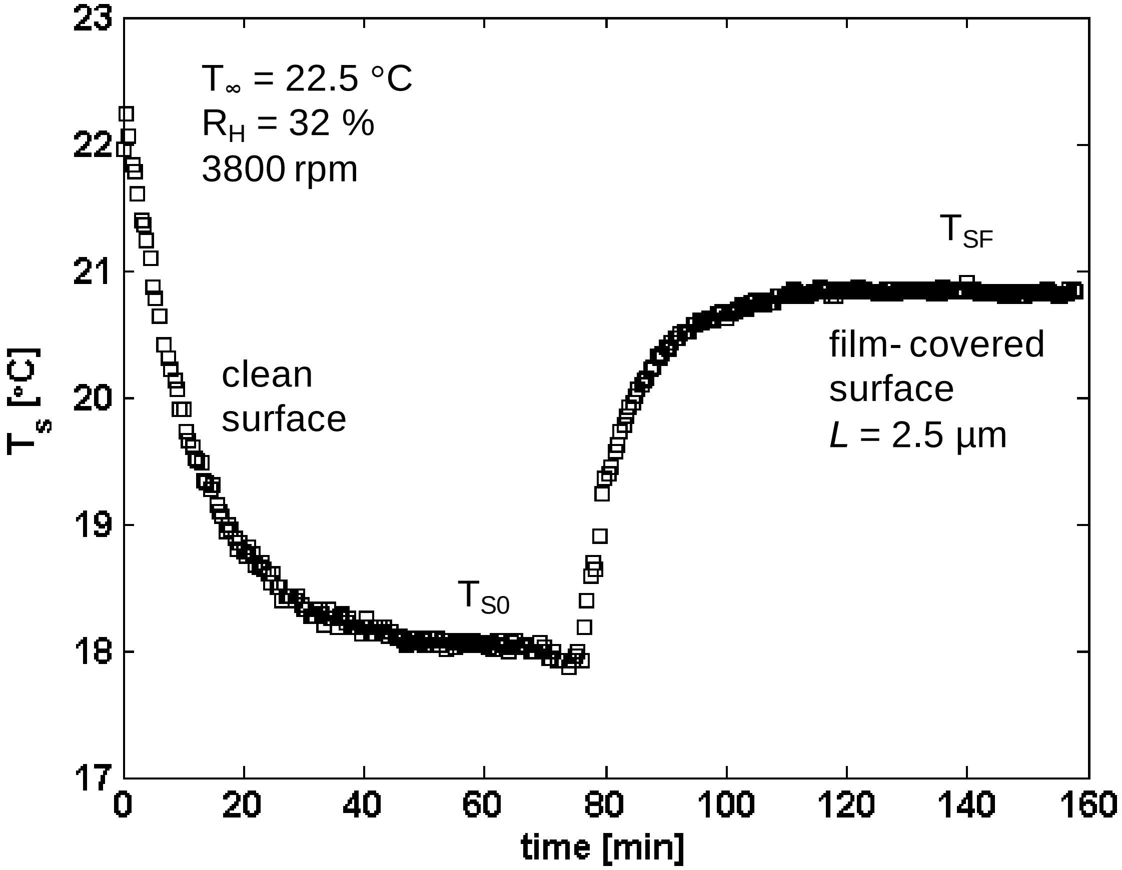

Fig. 11. Surface temperature versus time before and after application of a 2.5-µm MOx/BSM duplex-oil film in an unheated trough. The temperature of the clean-water surface falls to a steady temperature T_{S0} of ~18 °C. After film deposition at t ~ 75 min, the temperature rises, eventually reaching a new steady-state temperature of T_{SF} = 20.7 °C.

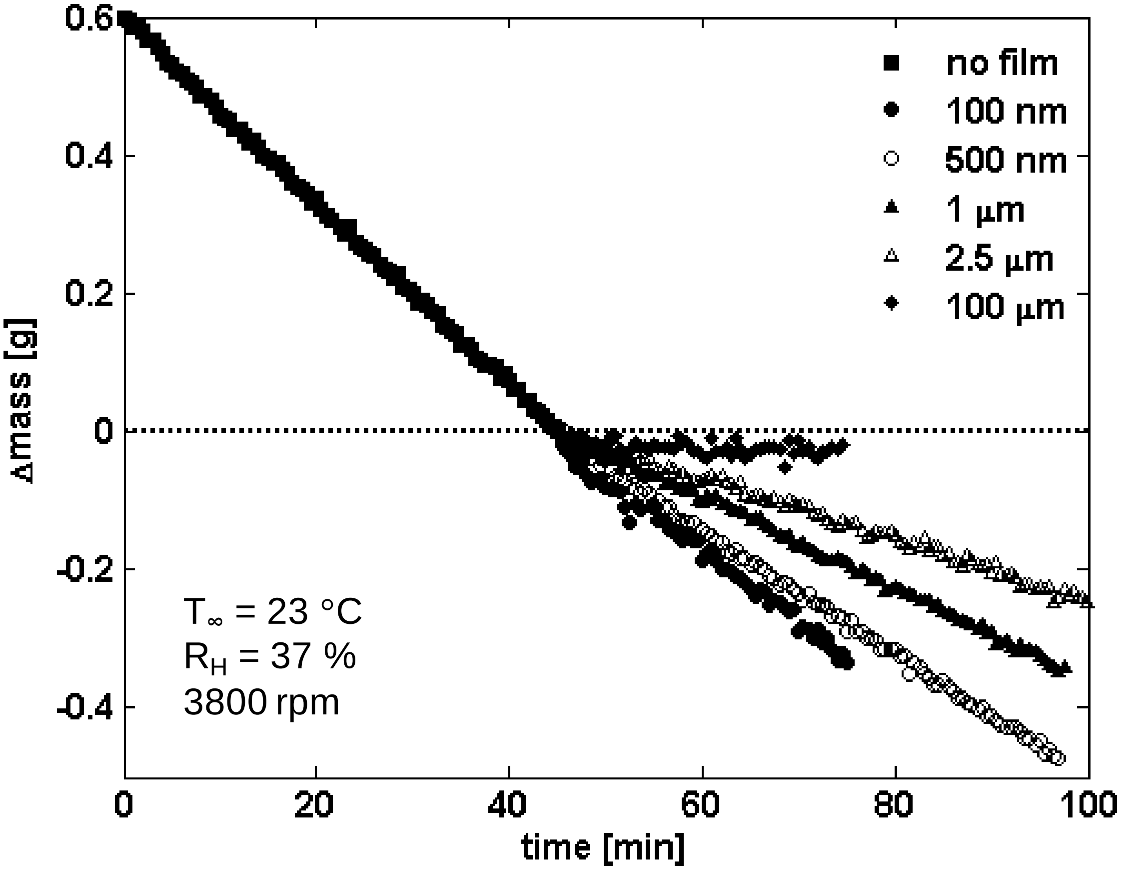

Fig. 12. Relative mass of water in the trough versus time at a fan speed of 3800 rpm before and after application of MOx/BSM films of varying thickness in an unheated trough. The mass for each experiment is shown relative to the mass at which the film was applied. (■) clean water, (●) 100-nm film, (○) 500-nm film, (▲) 1-μm film, (△) 2.5-μm film, and (◆) 100-μm film.

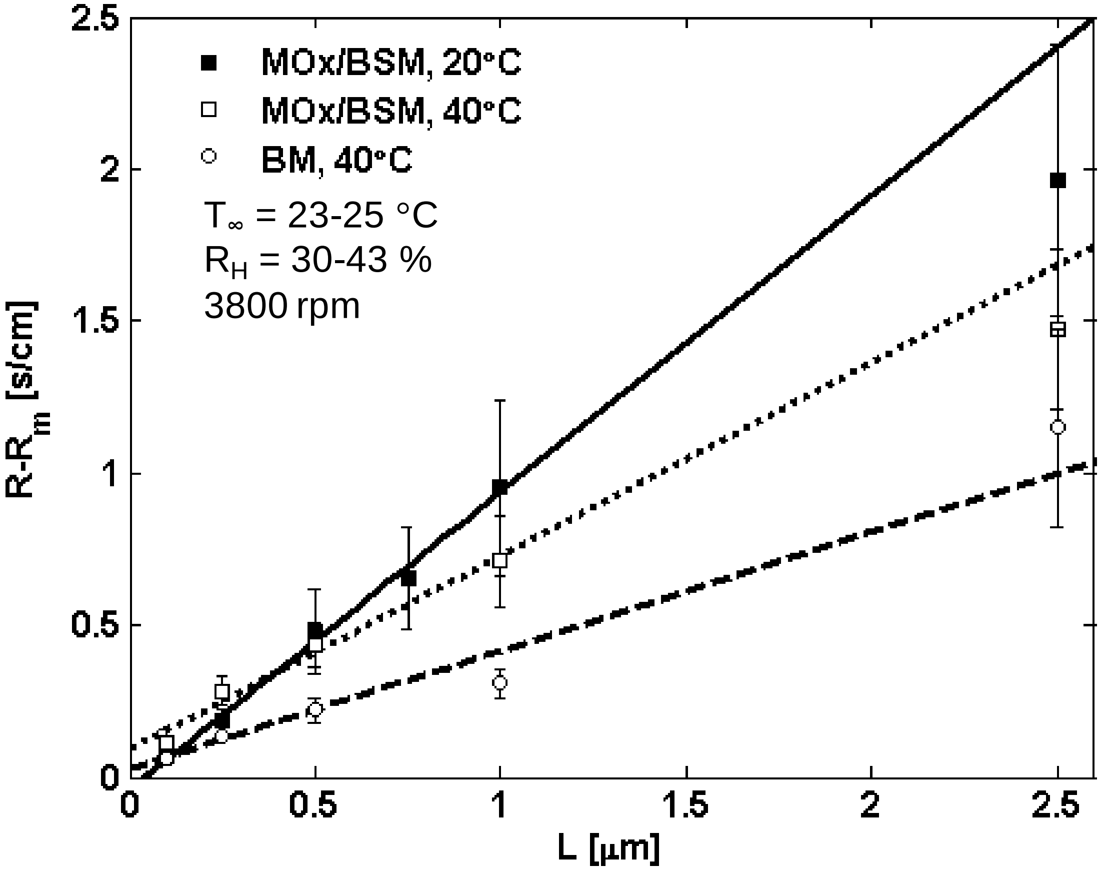

Fig. 13. Film resistance, *R-R*$_m$, versus film thickness, *L*, for various oil films and temperatures. Squares represent MOx/BSM and circles correspond to bovine meibum (BM). The average surface temperature for the filled symbols is T_{SF} = 20°C and for the open symbols is T_{SF} = 40°C. Best linear fits of the data up to 1 µm in thickness are shown.

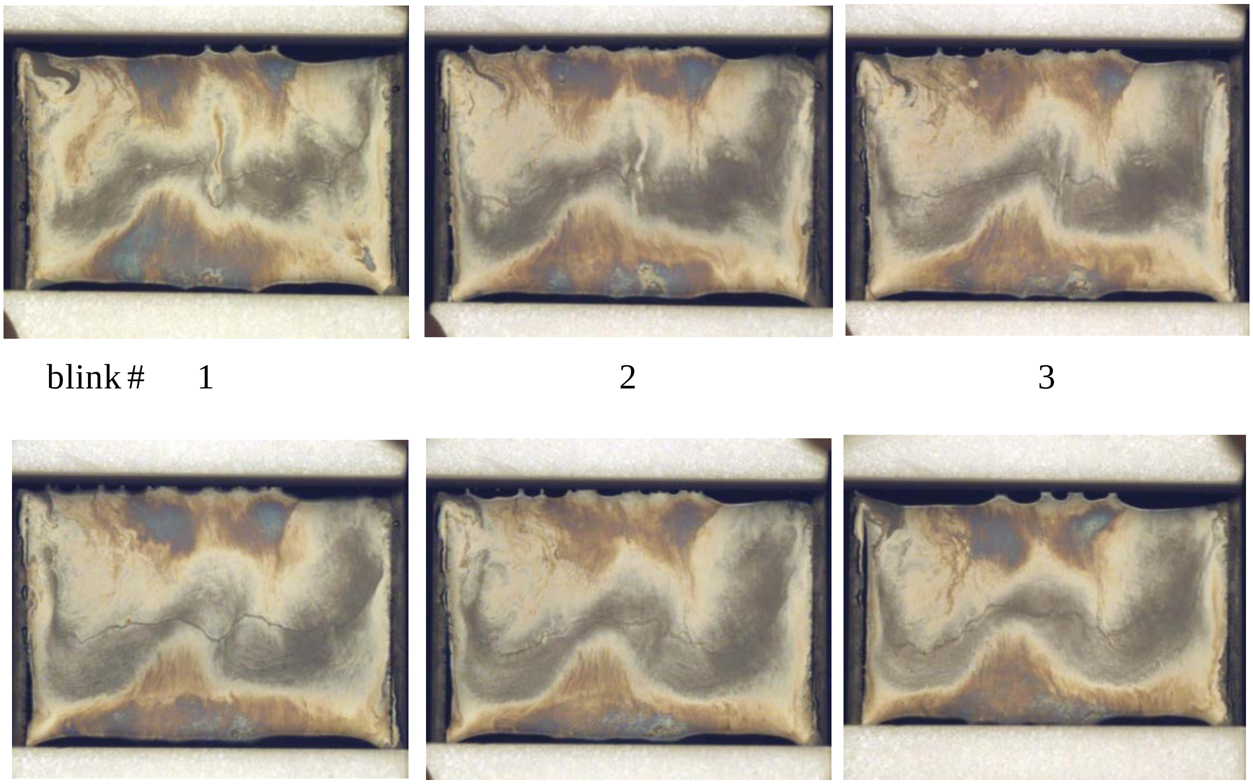

blink # 1 2 3

4 5 6

Fig. 14. Color interference patterns observed in *in-vitro* duplex films of MOx/BSM in the miniature Langmuir trough immediately after 6 successive blinks. The deposited films are 100-nm thick. Each image is taken immediately after the blink number denoted below the frame. (Compare with Fig. 7.)

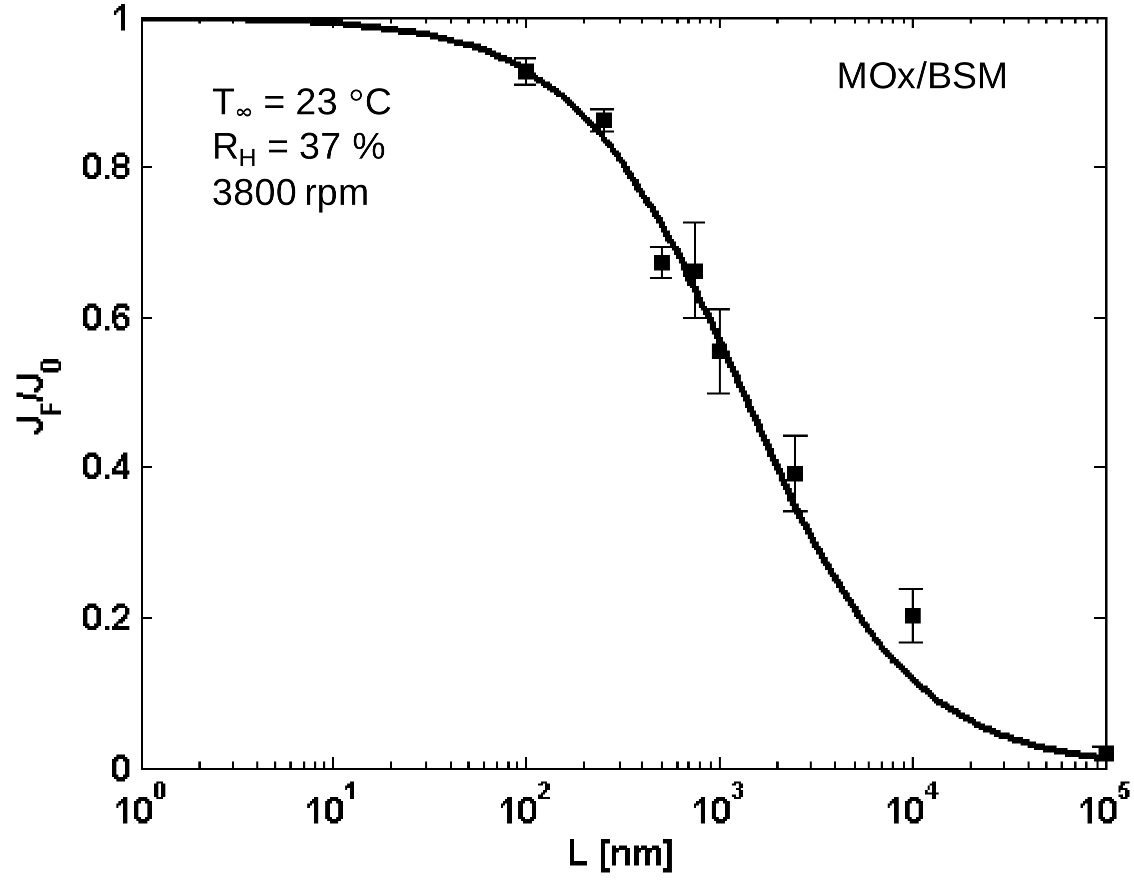

Fig. 15. Evaporation ratio J_F/J_0 versus oil-film thickness L for MOx/BSM in an unheated trough. Filled squares represent the average experimental values. Error bars denote the standard deviations. Solid line corresponds to theory (Eq. 18) with k_m = 1.34 cm/s and $Dk = 1.1\text{x}10^{-4}$ cm^2/s, determined by the fit in Fig. 13. Corresponding surface temperatures are given in Fig. 16.

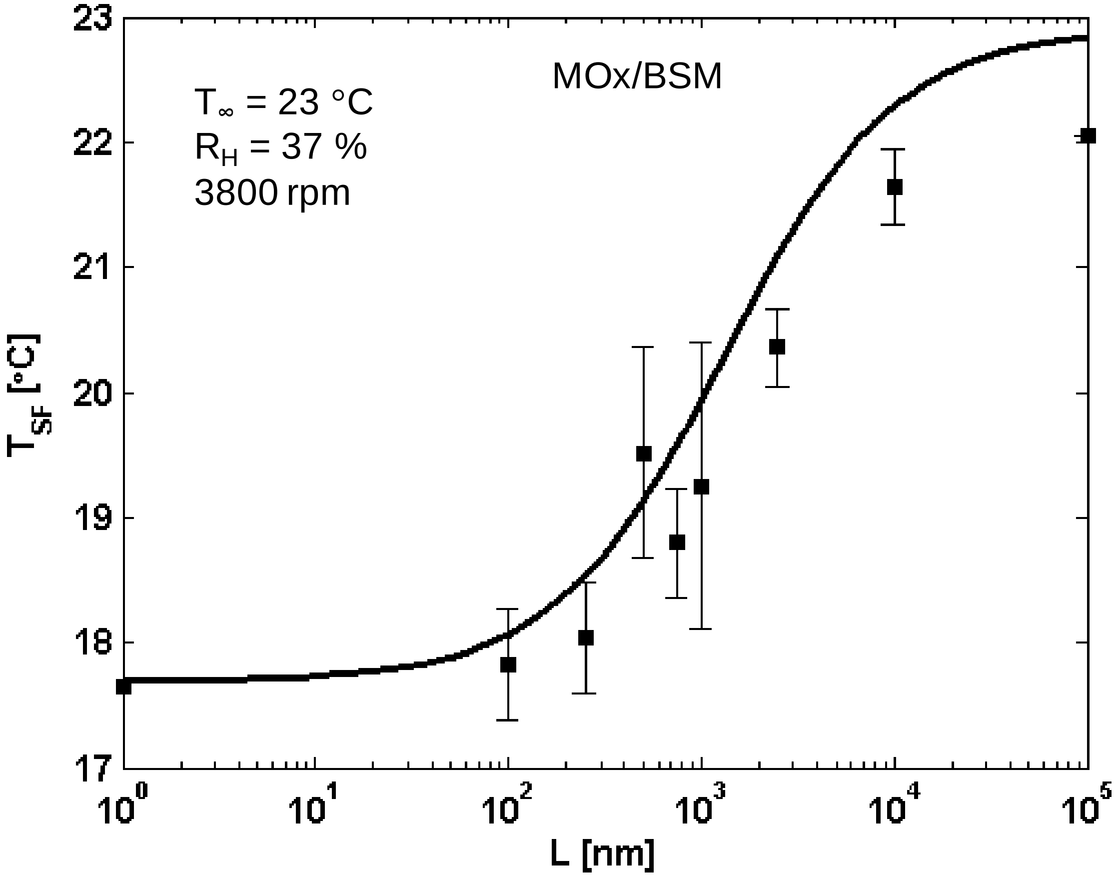

Fig. 16. Surface temperature T_{SF} versus oil-film thickness L for MOx/BSM films in an unheated trough. Filled squares represent the average measured values. Error bars denote the standard deviation. Solid line corresponds to theory (Eq. 24) with the same parameters as in Fig. 15.

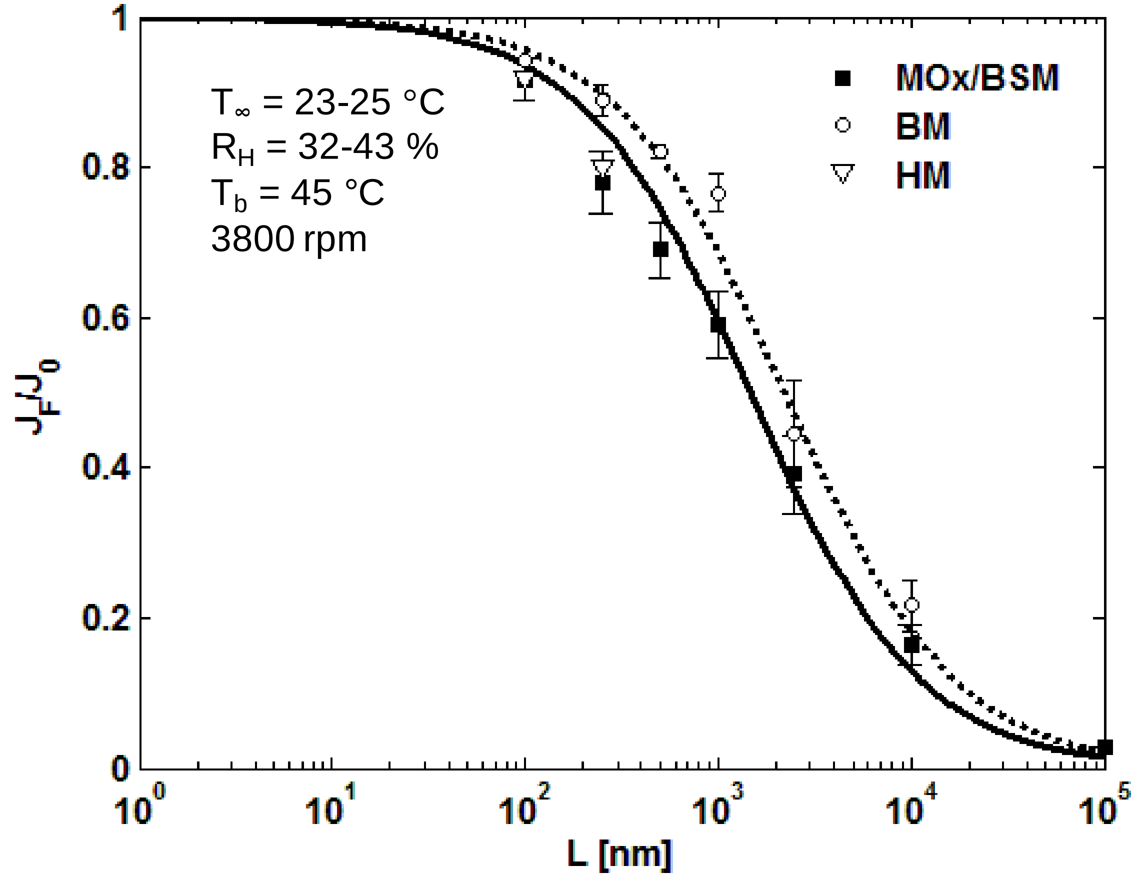

Fig. 17. Evaporation ratio J_F/J_0 versus oil-film thickness L for MOx/BSM (■), bovine-meibum (○), and human-meibum (▽) films in a heated trough (T_b = 45 °C). Lines represent the theory in Eq. 18 plotted for $Dk = 1.6\text{x}10^{-4}$ (solid line, MOx/BSM) and $2.6\text{x}10^{-4}$ cm^2/s (dotted line, BM). Corresponding surface temperatures are shown in Fig. 18.

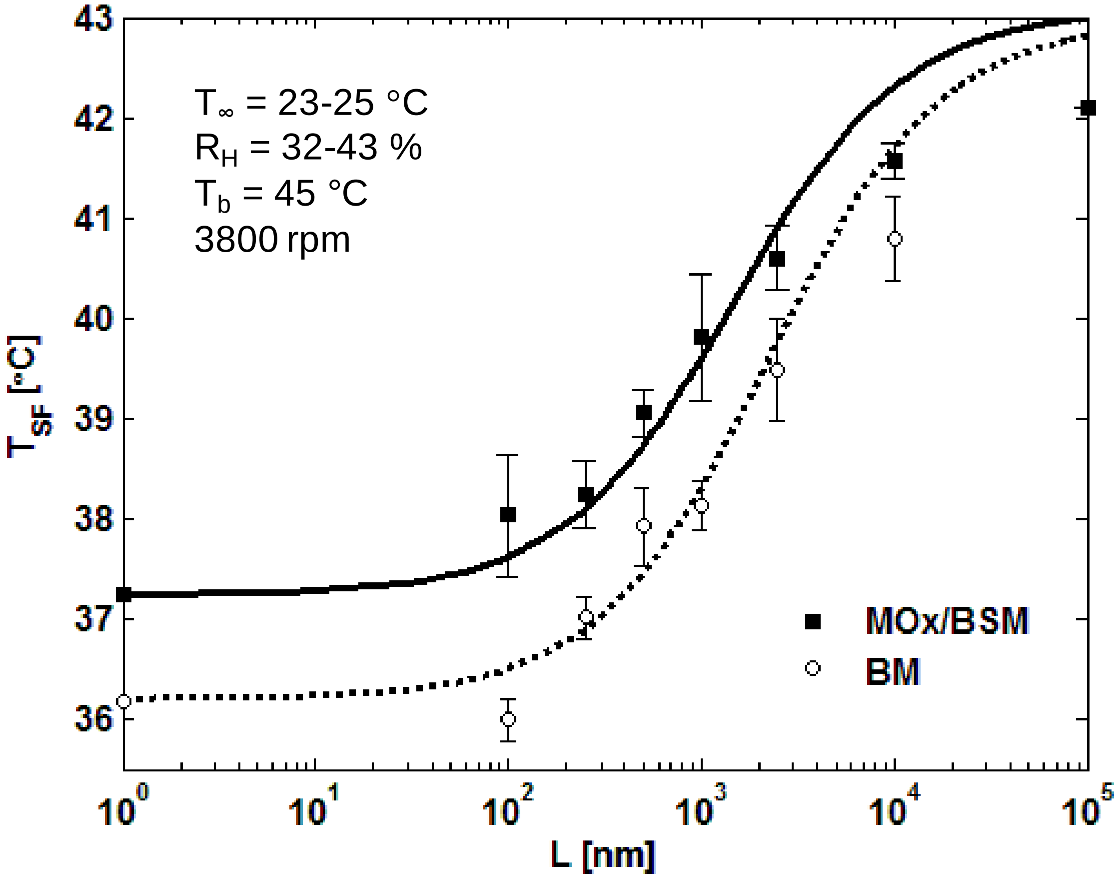

Fig. 18. Surface temperature T_{SF} versus oil-film thickness L for MOx/BSM (■) and bovine-meibum (○) films in a heated trough (T_b = 45 °C). Lines correspond to theory (Eq. 24) with the same parameters as in Fig. 17 (solid line = MOx/BSM, dotted line = BM). T_{S0} is shown at L = 1 nm.

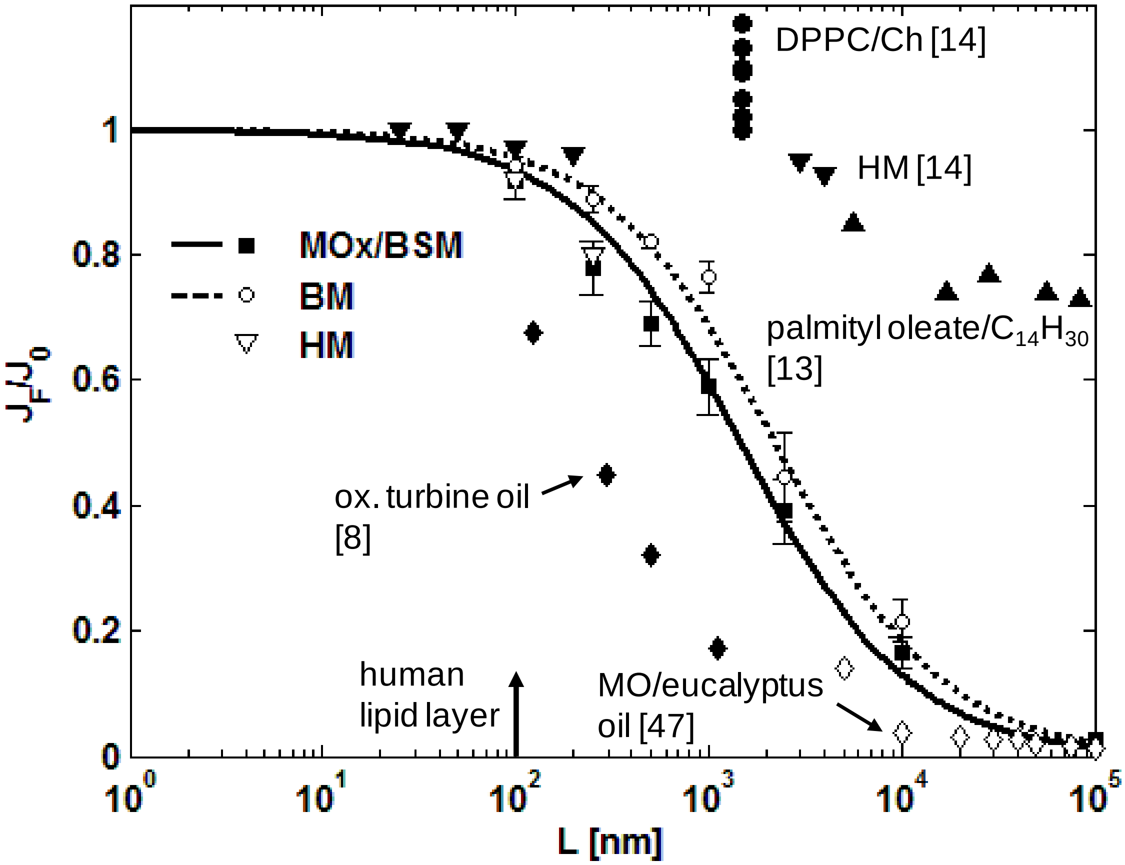

Fig. 19. Evaporation ratio J_F/J_0 versus film thickness L for literature data and from theory and data from this study in the heated trough. The solid line and filled squares correspond to theory and data for heated MOx/BSM films. The dotted line and open circles correspond to theory and data for heated bovine-meibum films. Inverted open triangles are from human meibum experiments in this study. (●) and (▼) correspond to DPPC/Cholesterol and human-meibum films reported by [14]. (▲) are palmitoyl oleate/$C_{14}H_{30}$ films measured by Borchman *et al.* [13]. (◊) are films of MO:eucalyptus oil measured by [47]. (♦) are calculated values for evaporation reduction based on the *Dk* measured by Langmuir and Schaefer [8] for oxidized-turbine-oil duplex films assuming $\phi = 1$. A vertical arrow at 100 nm shows the approximate thickness of the human TFLL.

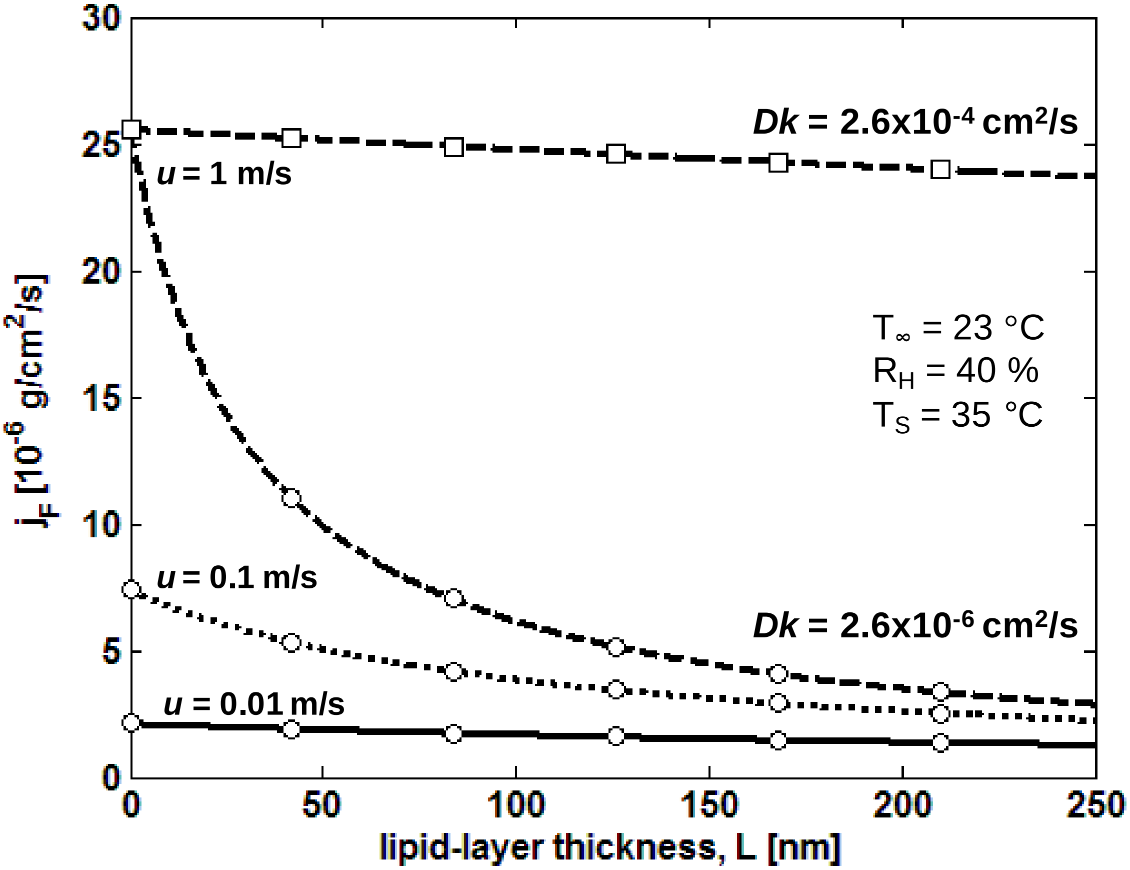

Fig. 20. Calculated evaporation rate, j_F, versus lipid-layer thickness, *L*, for various impinging-air speeds, *u*, for two lipid-layer permeabilities. Open squares and circles on the lines correspond to *Dk* = 2.6×10^{-4} and 2.6×10^{-6} cm^2/s. Air speeds of 0.01, 0.1, and 1 m/s (corresponding to nearly stagnant air, ventilated-room air, and walking) are shown with solid, dotted, and dashed lines, respectively. For air speeds 0.01, 0.1, 1 m/s, the corresponding j_0 values are 2.1, 7.4, and 2.6×10^{-6} $g/cm^2/s$, respectively.

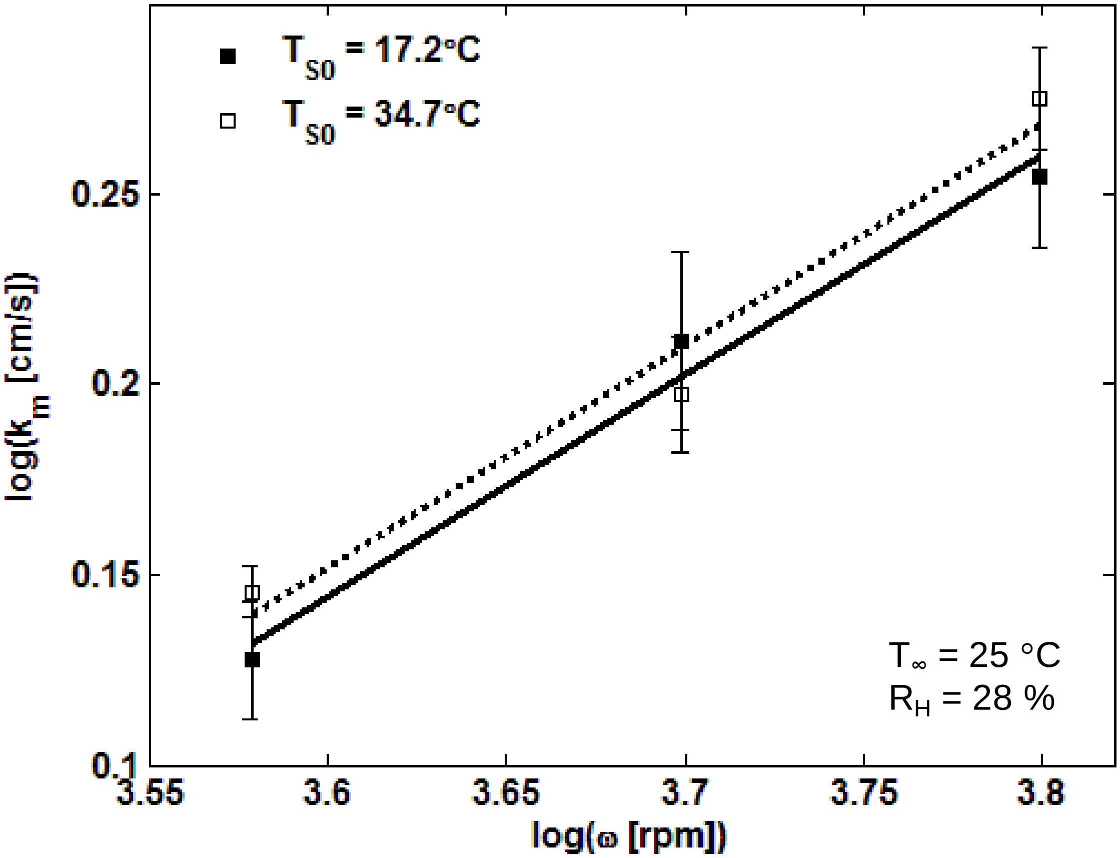

Fig. B1. Log-log plot of the measured mass-transfer coefficient [cm/s] versus fan speed [rpm]. Fan speeds used were 3800, 5000, and 6300 rpm. Error bars represent the standard deviation for each point, which was an average of 5-6 experiments. Filled and open squares correspond to data at T_{S0} of 17.2 and 34.7°C, respectively. The slope of both the solid and dotted best-fit lines is $m=0.58$. For the heated substrate, T_b = 43 °C.